Study of the Decay Matrix for $\eta' \rightarrow \eta\pi^+\pi^-$ using CLAS Detector at JLab

Ph.D. Thesis

By

SUDEEP GHOSH

DISCIPLINE OF PHYSICS

INDIAN INSTITUTE OF TECHNOLOGY INDORE

MAY 2018

Study of the Decay Matrix for $\eta' \rightarrow \eta\pi^+\pi^-$ using CLAS Detector at JLab

A THESIS

Submitted in partial fulfillment of the requirements for the award of the degree

of

DOCTOR OF PHILOSOPHY

by

SUDEEP GHOSH

DISCIPLINE OF PHYSICS

INDIAN INSTITUTE OF TECHNOLOGY INDORE

MAY 2018

INDIAN INSTITUTE OF TECHNOLOGY INDORE

CANDIDATE'S DECLARATION

I hereby certify that the work which is being presented in the thesis entitled **Study of the Decay Matrix for $\eta' \rightarrow \eta\pi^+\pi^-$ using CLAS Detector at JLab** in the partial fulfillment of the requirements for the award of the degree of **DOCTOR OF PHILOSOPHY** and submitted in the **DISCIPLINE OF PHYSICS, Indian Institute of Technology Indore**, is an authentic record of my own work carried out during the time period from July 2012 to May 2018 under the supervision of Dr. Ankhi Roy, Associate Professor, Discipline of Physics, IIT Indore and Dr. Moskov Amaryan, Professor, Department of Physics, Old Dominion University, Norfolk, VA 23529, USA.

The matter presented in this thesis has not been submitted by me for the award of any other degree of this or any other institute.

Signature of the student with date
(SUDEEP GHOSH)

This is to certify that the above statement made by the candidate is correct to the best of my/our knowledge.

Signature of Thesis Supervisor #1 with date | Signature of Thesis Supervisor #2 with date

(DR. ANKHI ROY) | **(DR. MOSKOV AMARYAN)**

MR. SUDEEP GHOSH has successfully given his/her Ph.D. Oral Examination held on ……………………………………….. .

Signature of Chairperson (OEB) | Signature of External Examiner | Signature(s) of Thesis Supervisor(s)

Date: | Date: | Date:

Signature of PSPC Member #1 | Signature of PSPC Member #2 | Signature of Convener, DPGC

Date: | Date: | Date:

Signature of Head of Discipline
Date:

ACKNOWLEDGEMENTS

I am thankful to nature for giving me all the perseverance, patience and hard work during this journey. I could not imagine a journey full of excitement and learning. It is a moment of pride to stand at this point, having solved couple of problems that looked difficult during the journey.

I owe a lot to some people, who kept their trust in me and supported me.

I want to begin thanking my supervisor Dr. Ankhi Roy, apart from the formal responsibilities, she has been instrumental in keeping me educated, focused and well prepared, sometimes going out of protocols to help me as a friend to make my path comfortable.

Heavily benefited by my co-supervisor Professor Moskov Amaryan, supported me with a lot of research related ideas and funding. A special mention to Dr. Susan Schadmand who helped me focus personally and administrative side of the course. I was constantly counseled by Dr. Biplab Ghosh, helping me take a variety of approaches to problems. Dr. Raghunath Sahoo and Dr. Swadesh Sahoo were the people responsible for evaluating my progress every year, they kept me on track with their valuable suggestions and constructive criticism. Lastly, I am highly indebted to all the faculties in the Discipline of Physics, Indian Institute of Technology Indore, never before could I experience such an environment, that fostered innovation, problem-solving and achievement.

I am highly indebted to the reviewers of the thesis for pointing out genuine flaws which helped me to improve the overall quality of the thesis.

The nature of the work I performed in my PhD gave me the opportunity to visit different countries, work at few of the finest research labs in the world. In this journey, I made many friends from various institutes and work culture. The exposure helped me to understand the science and world at large in a different perspective.

Indian Institute of Technology Indore is a great institution. I met a large pool of talents and made friends from different part of the country. Their contribution towards my development, both personally and academically played a vital role. Also thanks to the financial support provided by the institute and MHRD, Government of India.

To name a few Surjendu Bikash Dutta, Aditya Nath Mishra, Ankita Goswami, Aparna Rai, Camellia Sarkar Das, Nazimuddin Khan, Ajay Kumar, Ajay Pratap and Prakhar Garg. It is difficult to imagine a smooth sail without having such people in place.

I cannot possibly forget my time at Old Dominion University & Jefferson Lab, USA and Nuclear Physics Institute and Juelich Center for Hadron Physics, Forschungszentrum Juelich, Germany. I made friends with few of the smartest people in these places who help me with research input and ideas to complete the work. One such friend is Dr. Michael Kunkel who guided me throughout my PhD period earnestly, Georgie Mbianda is another such friend who worked with me and we both faced challenges and learned in the process.

At the end of the day, my achievements will be incomplete and efforts will not matter without my family making me successful as a human being, my father Sujit Kumar Ghosh and my mother Rina Ghosh always encouraged me to chase my dreams without the fear of failure. I also want to thank my elder brother Rajdeep Ghosh for generating curiosity towards science, logical reasoning and especially physics from early childhood. I also want to thank my superhero sister-in-law Nayana Hazarika Ghosh and my nephew Ethan for filling my life with various moments of joy and fun in this important journey. I am really lucky to have some amazing friends who make my life complete and make me question my boundaries, to name a few, Abhishek Banerjee, Sujoy Shil, Srimit Sarkar, Sandip Tirkey, Debarati Roy, Sarmistha Saha and Amrita Saha.

DEDICATION

Dedicated to people fighting around the world against superstitious beliefs, uneducation, unjust customs, social and financial discrimination.

LIST OF PUBLICATIONS

Publications from Thesis work:

1. M.C. Kunkel, M. J. Amaryan, S.Ghosh, A.Roy (2018), et al., Exclusive photoproduction of π^0 up to large values of Mandelstam variables s, t, and u with CLAS, PHYSICAL REVIEW C 98, 015207
   Available online. DOI: https://journals.aps.org/prc/pdf/10.1103/PhysRevC.98.015207

2. Sudeep Ghosh and Ankhi Roy (2017), An improvement to the measurement of Dalitz plot parameters, Papers in Physics 9, 090009
   Available online. DOI: http://dx.doi.org/10.4279/PIP.090009

3. S. Ghosh, A. Roy for the CLAS collaboration (2016), *Dalitz plot of* $\eta' \to \eta\ \pi^+\ \pi^-$, EPJ Web Conf., **130**, 03002
   Available online. DOI: https://doi.org/10.1051/epjconf/201613003002

4. S. Ghosh for the CLAS collaboration (2016), *Dalitz plot analysis of* $\eta' \to \eta\ \pi^+\ \pi^-$, AIP Conference Proceedings, **1735**, 030018
   Available online. DOI: http://dx.doi.org/10.1063/1.4949401

5. S. Ghosh, A. Roy for the CLAS collaboration (2014), *Calculation of the matrix element for the hadronic decay* $\omega \to \pi^0\ \pi^+\ \pi^-$, Proceedings of the DAE Symp. On Nucl. Phys, **59**, 648

6. S. Ghosh, A. Roy for the CLAS collaboration (2013), *Dalitz plot of the hadronic decay* $\eta' \to \eta\ \pi^+\ \pi^-$, Proceedings of the DAE International Symp. On Nucl. Phys, **58**, 242

Publications from other work:

1. Hans-Peter Morsch and **Sudeep Ghosh** (2017), Chiral Structure of Particles Bound by Magnetic Forces, Journal of Advances in Mathematics and Computer Science, ISSN: 2231-0851, 24(4): 1-11
   Available online. DOI : 10.9734/JAMCS/2017/35743

Analysis Note:

1. "Dalitz Plot Analysis of eta' to eta pi+ pi- from CLAS g12 Data Set", under review in 2nd round, Available online: https://www.jlab.org/Hall-B/shifts/index.php? display=admintask =paperreview

ABSTRACT

KEYWORDS:

Dalitz plot, Decay Matrix, Matrix element of decay

In the present thesis work, we report the results of Dalitz plot analysis of the hadronic decay $\eta' \to \eta\ \pi^+\ \pi^-$ using CLAS detector through the photoproduction reaction γ p $\to \eta'$ p. The dynamical information about the three-body decay of any meson can be obtained by studying the decay matrix and Dalitz plot is a tool to perform the study. The Dalitz plot is a scatter plot to study decay dynamics of a meson decaying into three bodies. As the three-body decay has two degrees of freedom, one can define two linearly independent variables X and Y to represent the decay in the phase space as:

$$X = \frac{\sqrt{3}(T_{\pi^+} - T_{\pi^-})}{Q} \tag{1}$$

$$Y = \frac{(m_\eta + 2m_\pi)}{m_\pi} \cdot \frac{T_\eta}{Q} - 1. \tag{2}$$

Where T_η, T_{π^+} and T_{π^-} are the kinetic energies of the particles η, π^+ and π^- respectively in the rest frame of the η' meson and Q = T_{π^+}+T_{π^-}+T_η. The m_η and m_π are the masses of η and π mesons respectively.

The obtained Dalitz plot phase-space is parameterized with a general parametrization function given in equation (3), which gives the amplitude of the $\eta' \to \eta\ \pi^+\ \pi^-$ decay. The square of decay amplitude is given by,

$$f(X, Y) = M^2 = A(1 + aY + bY^2 + cX + dX^2). \tag{3}$$

Where a, b, c and d are the Dalitz plot parameters of the decay and A is the normalization constant. The parameters give information of the resonances, intermediating particles and interactions among the decay of final state particles.

Physical observables e.g. decay width, phase shifts, quark mass ratio and parameters quantifying interactions can also be calculated from the Dalitz plot parameters. Also, a precise measurement of these parameters is needed for the correct input to the theoretical distribution of the effective chiral Lagrangian.

Current status of experimental data on $\eta' \rightarrow \eta\ \pi^+\ \pi^-$ decay is based on the following: the VES Collaboration, which has reported the Dalitz plot parameters of $\eta' \rightarrow \eta\ \pi^+\ \pi^-$ with 14.6 x 10^3 events in charge exchange (π^- p $\rightarrow \eta'$ p) and 7 x 10^3 events in diffraction like production (π^- N $\rightarrow \eta'\ \pi^-$ N), the BESIII Collaboration has also reported $\eta' \rightarrow \eta\ \pi^+\ \pi^-$ decay parameters ($e^+\ e^- \rightarrow \pi^+\ \pi^-$ J/$\psi \rightarrow \eta'$ γ) with 43826 $\pm$ 211 events with better precision compared to VES. The two measurements disagree with each other and with the theoretical calculation of the parameters. Our Dalitz plot analysis of $\eta' \rightarrow \eta\ \pi^+\ \pi^-$ decay from the CLAS *g12* dataset is based on 160090 events and subsequent decay of $\eta' \rightarrow \eta\ \pi^+\ \pi^-$, which has the competitive statistics to study the parameters with low statistical errors. An important component of the Dalitz distribution in the decay $\eta' \rightarrow \eta$ $\pi^+\ \pi^-$ is the invariant mass of the π^+ and π^- mesons (M(π+ π−)) which is also presented and compared to various theoretical models. This component is sensitive to intermediating particles and interactions among the final state mesons.

The Continuous Electron Beam Accelerator Facility (CEBAF) at Jefferson Lab (JLab), Newport News, Virginia, USA has performed the "*g12*" experiment and collected the data during March - June 2008. The data is recorded using the CEBAF Large Acceptance Spectrometer(CLAS) detector and further used to perform the analysis.

The complete reaction under study is " γ p $\rightarrow \eta'(\rightarrow \eta\ \pi^+\ \pi^-)$ p" and events with one proton, one π^+, one π^- and any number of neutral particles are selected as skim condition out of all events available in "*g12*" dataset. In this analysis η and η' mesons are reconstructed as a missing particle. The η' meson is reconstructed with the information of incident photon, target proton and final state proton and it is represented as M_x(p). Similarly, η reconstruction uses incident photon, target proton and final state particles such as the proton, π^+ and π^- and it is denoted as M_x(pπ+π-). The threshold energy for the production of η' meson is 1.45 GeV and the production cross-section of the η' meson drops significantly after 3.6 GeV. Hence the analysis is performed with all events with an incoming photon energy from the threshold of 1.45 up to 3.6 GeV.

The Pluto [v5.42] event generator developed by the HADES collaboration is used in this analysis for the simulation. The 5 x 10^8 γ p $\to$ η' p $\to$ η π^+ π^- p events are generated using Pluto along with a model which is close to the real scenario. The incident photon beam is given a bremsstrahlung nature to reproduce the bremsstrahlung photon beam distribution of the incident photons. To make the simulation more realistic the measured differential cross-section of the η' meson is used as input during event generation. The output of the Pluto with the above-mentioned model is first extracted in the standard CLAS "gamp" files and then processed with CLAS simulation suit in the following order:

- The gamp files are first converted into the format of the PART bank containing the event.

- GSIM (Geant3-based simulation): GSIM in CLAS simulates the decay tracks of particles and finally the digitized information is sorted in other "raw" banks from the PART bank.

- GPP (GSIM post-processor): The events are passed through GPP, which smears detector signal more accurately to reflect the actual resolution of *g12* data and simulate the experimental conditions.

- a1c: Finally the events are passed through a1c, which is a reconstruction program for the simulated data. The same program is used during data reconstruction.

The next step is to improve the identification of the particles and signal to background ratio using conditions and corrections. All these conditions and corrections which are implemented in this analysis for data and simulation are listed in Table 1.

This work used a Dalitz plot which has 30 bins in X and 30 bins of Y, which gives a total of 900 bins in Dalitz plot. Out of these 900 bins, those bins which fall

Table 1: The list of conditions and corrections implemented to the *g12* data and simulation.

"*g12*" Experiment data	Simulation
Photon Multiplicity	NA
Beam Energy Correction	NA
Momentum Correction	NA
Removal of bad TOF paddle	Applicable
Geometric Fiducial Cut	Applicable
Kinematic Fit (1% probability cut)	Applicable
Vertex Length Cut (-70 $\leq v_z \leq$ -110 cm)	Applicable
Vertex cross-sectional radius ($\sqrt{v_x^2 + v_y^2}$ $\leq$ 2 cm)	Applicable
Timing Cuts on proton, π^+ and π^- ($t_{vert}(TOF)$ and $t_{vert}(Tagger)$ $\pm$ 1.0 ns)	Applicable
$\mid \cos\theta_{center-of-mass}$ of $\eta' \mid \leq 0.85$	Applicable
$\mid M_x$(p $\pi+$ $\pi-$) - 0.547 $\mid \leq$ 0.015 GeV	Applicable

Table 2: Dalitz plot parameters from both the fit methods.

	Acceptance correction method	Smearing matrix method
a	-0.1511 ± 0.0068	-0.1508 ± 0.0069
b	-0.1583 ± 0.0115	-0.1514 ± 0.0120
c	0.0138 ± 0.0092	0.0128 ± 0.0094
d	-0.0780 ± 0.0121	-0.0813 ± 0.0127
χ^2/ndf	1.18	1.16

outside the phase space of decay or bins with very low acceptance ($< 0.5\%$) are rejected. Finally, out of 337 bins are subtracted for background and a background subtracted Dalitz plot is obtained for further analysis and calculation of Dalitz plot parameters.

Once all the conditions and corrections are implemented, a background subtraction is performed to extract the $\eta' \to \eta\ \pi^+\ \pi^-$ events and eliminate all other channels which lead to the same final state of one proton, one π^+ and one π^-.

To cross-check the analysis and increase the confidence of the results, the Dalitz plot parameters are calculated with the following two different methods:

- Acceptance correction method: The $\eta' \to \eta\ \pi^+\ \pi^-$ decay contribution for each Dalitz plot bin is corrected for acceptance, without considering the migration of events from one bin to other.

- Smearing matrix method: In this method, the fits are performed directly to the Dalitz plot from data along with a function. This function takes care of the acceptance in the same bin and also acceptance due to the migration from neighboring bins using a smearing matrix.

The number of bins selected along the Dalitz variables X and Y are higher than the resolution of these variables, so these two independent methods yield similar Dalitz plot parameters within the statistical errors, which also serves as a cross-check to the analysis. The calculated Dalitz plot parameters a, b, c and d from both the methods are given in Table 2.

In this thesis, the dominant decay mode of η' which is $\eta' \to \eta\ \pi^+\ \pi^-$ is studied. The decay also produces $\eta' \to 3\pi$ decay which is an isospin violating mode and it is through a mixing of η^0 - π^0 meson. This effect arises from the light quark mass differences. Hence this study is an indirect probe to understand the decay dynamics of mesons. This decay information is studied with the help of a Dalitz plot distribution. The results from this Dalitz plot distribution is then compared to reported experiments.

To gain more confidence over extraction of events from the experiment, a measurement of the cross-section of η' is also done and compared to the previous *g11* measurement. The generated events used in the analysis were also modeled very carefully to appear as close to nature. A very sensitive background subtraction is performed to both the smooth and in-peak backgrounds. The goodness of fit is reflected in the χ^2/ndf of each bins which is above 0.5 and below 2 even for the bins with low statistics. Also, the fit to the whole Dalitz plot yields a reasonable χ^2/ndf of 1.16, which shows the quality of the fit. The Dalitz plot parameters are calculated with two independent methods and matches within the statistical errors from both the methods because of the choice of wide binning, which is 3 times more than the resolution of Dalitz variables X and Y. The choice of the binning is a result of the optimization of the total number of events and the resolution of the Dalitz variables. The "Smearing matrix method" being a more realistic approach has been used to present the final Dalitz plot parameters and to perform systematic studies in the analysis.

A comparison of the *g12* Dalitz plot parameters with the other experimental results is shown in the Table 3. The parameters a and b from the CLAS *g12* measurement are consistent within 1 σ to the results reported by the VES and shows disagreements with the BESIII parameters. The parameter c which indicates C-parity violation in the strong interaction when it deviates from zero. In the present analysis, the c parameter is consistent to zero within 1.5 σ. The parameters c and d from *g12* measurement is consistent with both the experiments. The Dalitz plot parameters are also compared to neutral decay mode of the η' meson, the $\eta' \to \eta$ $\pi^0\ \pi^0$ decay for the measurements from the GAMS, A2 Collaboration at MAMI and the BESIII Collaboration. Our parameters for $\eta' \to \eta\ \pi^+\ \pi^-$ decay show deviation by 4 standard deviations from all the measurement of neutral decay mode of η' meson for the Dalitz parameters a and b. Our measurement seems to agree within statistical limits for the parameter d to both the recent measurements from A2 Collaboration at MAMI and the BESIII Collaboration.

A comparison of the *g12* Dalitz plot parameters with the U(3) Chiral effective theory is shown in the Table 4. The value of b and d from *g12* measurement as well as from the previous measurements largely deviate from zero. However, the framework U(3) chiral unitary approach and U(3) chiral effective field theory in combination with a relativistic coupled-channels approach predict b and d to be zero which recommends the theory to include the final state interaction corrections in the chiral model for pseudoscalar mesons. The theory* in the Table 4 is resulting from theoretical fits which include the VES data.

The $\eta' \to \eta\, \pi^+\, \pi^-$ decay is also used to study a scalar intermediate particle. The η' and η meson are pseudoscalars and both has an isospin (I) of 0. The isospin I, for both the π^+ and π^- is 1. Due to the conservation of 3^{rd} component of the isospin (I_3), the η' meson can decay into π^+ and π^- through an intermediate scalar meson. Hence, we looked at the invariant mass of $\pi^+\, \pi^-$ distribution and compared it to the theoretical distribution which considers intermediate states of decays. A good sensitivity to the parameters of the σ meson decay to the π^+ π^- in the $\eta' \to \eta\, \pi^+\, \pi^-$ decay is found and compared to the Nonlinear Sigma Model Lagrangian (NLSM) and Generalized Linear Sigma Model (GLSM). The right-centered distribution of the acceptance corrected invariant mass of $\pi^+\, \pi^-$ mesons, M(π+ π−) distribution from CLAS *g12* data is due to the σ contribution. However, in the absence of σ meson from the NLSM, the centeredness of M(π+ π−) shifts from right towards the left.

The organization of the thesis is as follows:

Chapter 1 provides the introduction to fundamental particles and basic forces within the Standard Model, thereon the formation of hadrons and the properties of the pseudoscalar meson η' and its decay to $\eta\, \pi^+\, \pi^-$ are discussed. Later on, the Chiral Perturbation Theory is explained for pseudoscalar mesons and the $\eta' \to \eta\, \pi^+\, \pi^-$ decay along with its applicability and reason behind the acceptabil-

Table 3: Comparison of *g12* Dalitz plot parameters of the $\eta' \to \eta\ \pi^+\ \pi^-$ decay with various experimental results.

Parameter	VES	BESIII (Old)	BESIII (New)	CLAS $g12$
a	-0.127 ± 0.016 ± 0.008	-0.047 ± 0.011 ± 0.003	-0.056 ± 0.004 ± 0.002	-0.151 ± 0.007 $^{+0.008}_{-0.012}$
b	-0.106 ± 0.028 ± 0.014	-0.069 ± 0.019 ± 0.009	-0.049 ± 0.006 ± 0.006	-0.151 ± 0.012 $^{+0.006}_{-0.006}$
c	0.015 ± 0.011 ± 0.014	0.019 ± 0.011 ± 0.003	0.0027 ± 0.0024 ± 0.0018	0.013 ± 0.009 $^{+0.017}_{-0.020}$
d	-0.082 ± 0.017 ± 0.008	-0.073 ± 0.012 ± 0.003	-0.063 ± 0.004 ± 0.003	-0.081 ± 0.013 $^{+0.017}_{-0.023}$
χ^2**/ndf**	1.13	1.05	...	1.16

Table 4: Comparison of *g12* Dalitz plot parameters to the theoretical predictions.

	Theory*	Theory	Theory	**CLAS** *g12*
a	-0.093	-0.116 ± 0.024	-0.116 ± 0.011	-0.151 ± 0.007
b	-0.059	0.000 ± 0.019	-0.042 ± 0.034	-0.151 ± 0.012
c	...	...	...	0.013 ± 0.009
d	-0.003	0.016 ± 0.035	0.010 ± 0.019	-0.081 ± 0.013
χ^2**/ndf**				1.16

ity of the theory. At this point the theoretical foundation of the problem is set, so we moved on to explain a Dalitz plot and how it is used to extract the decay parameters. Finally, the current status of the study and importance of the results are discussed.

Chapter 2 covers the details of the experimental facility directly related to the analysis. It includes the CEBAF accelerator, hall B photon tagger, the CLAS detector and subdetectors, triggers and data acquisition. Additionally, it will also explain how the raw data from various subdetectors are interpreted and prepared for performing data analysis.

Chapter 3: The recorded, pre-sorted and calibrated data available on the JLab data farms and the required corrections and selections with the help of analysis programmes to reconstruct γ p $\rightarrow \eta'(\rightarrow \eta\, \pi^+\, \pi^-)$ p decay events are explained here. The chapter also gives a brief summary of the *g12* run, the simulation framework and series of events selection criteria along with the corrections required for the reconstruction of these events.

Chapter 4: This chapter explains detailed steps involved in obtaining the Dalitz plot and the Dalitz plot parameters for the $\eta' \rightarrow \eta\, \pi^+\, \pi^-$ decay. We performed the background subtraction in two steps, first the non-resonant background subtraction and second, the in-peak background reduction using the realistic Monte-Carlo simulations. Then we moved on to explaining how the background subtracted Dalitz plot is fitted to a general parameterization using two different and independent methods along with acceptance correction to obtain the final Dalitz plot parameters.

Chapter 5: This chapter shows in details the calculation of the systematic errors from all the different sources and our criterion on deciding which among those sources should be considered to be the part of final result. The error which cannot be explained by the statistical fluctuations of the measurement were finally added to the results after adding all the systematic errors from the sources in quadrature.

Chapter 6: This chapter concludes the final Dalitz plot parameters along with all the experimental errors and the invariant mass distribution of pions using

CLAS *g12* experiment. The significance of the results, conclusion and outlook of the analysis and its comparisons to other theories and experiments are also covered in this chapter.

Contents

Figures

Tables

Chapter 1

Introduction

This chapter gives an introduction to the fundamental particles and basic forces within the Standard Model. The thesis is based on the study of the Dalitz plot for etaprime (η') decay ($\rightarrow \eta\ \pi^+\ \pi^-$), so the formation of hadrons and the properties of the pseudoscalar meson η' and its decay to $\eta\ \pi^+\ \pi^-$ are discussed. Later, the Chiral Perturbation Theory is explained for pseudoscalar mesons and its applicability to $\eta' \rightarrow \eta\ \pi^+\ \pi^-$ decay is discussed. At this point, the theoretical foundation of the problem is well defined. So, we explain a Dalitz plot and how it is used to extract the decay parameters. Finally, the current status of the study and the importance of the results are discussed.

1.1 Motivation

Quantum Chromodynamics (QCD) is the theory of strong interaction. There has been a lot of work and progress in the field of perturbative QCD which is a part of high energy physics. However, the scientific community has less understanding of particle behavior in the low energy regime or the non-perturbative QCD regime. We do not have a complete explanation for phenomena like quark confinement and asymptotic freedom [1]. Strong interaction is also responsible for the production of pseudoscalar mesons. However, the theory does not give a suitable explanation for the higher mass of the η' meson compared to other pseudoscalar mesons. Due to the axial U(1) anomaly and heavier mass of the meson, the η' is not a Goldstone boson in the chiral limit [2].

The Jefferson Lab (JLab) at Newport News, USA has an accelerator facility, which provides a very suitable range of energies for production and detection of light pseudoscalar mesons. We, as a part of the "Light Meson Decay CLAS, Approved Analysis (LMD-CAA)" group, study the low energy QCD regime using the data from the facility, and share the following common objectives:

- Transition form factor of different light mesons
- Dalitz plot analysis of different hadronic decay channels of light meson
- Branching ratio calculation of different rare decay channels
- Different symmetry violating decay channel
- Mixing angle between different mesons

The present thesis work is focused on understanding the decay of the pseudoscalar meson η' into $\eta\ \pi^+\ \pi^-$. A Dalitz plot is used here to study the decay, which contains kinematical information of the decay. A better understanding of these plots will help physicists to avoid tedious calculations and reject the incorrect interpretation of the experimental effects. The results will be particularly useful to give inputs to hadronic spectroscopy problems and develop the theoretical distributions of effective or the non-perturbative QCD [3].

1.2 The Standard Model (SM)

The whole visible universe is made up of subatomic particles which are bound together with four unique kinds of interactions among them. The SM of particle physics describes the electromagnetic, weak and strong interaction excluding gravity among all these interactions. The SM of particle physics is one of the most accepted theories that describes all known fundamental particles and the interactions between them except gravity. The Fig. 1.1 shows all the fundamental quarks, leptons and the gauge bosons along with their respective mass, charge and spin.

The majority of particles in the visible universe are composed of six quark flavours in three different colors (Red, Blue and Green), six leptons and antiparticles of both quarks and leptons, which are the building blocks of all matter

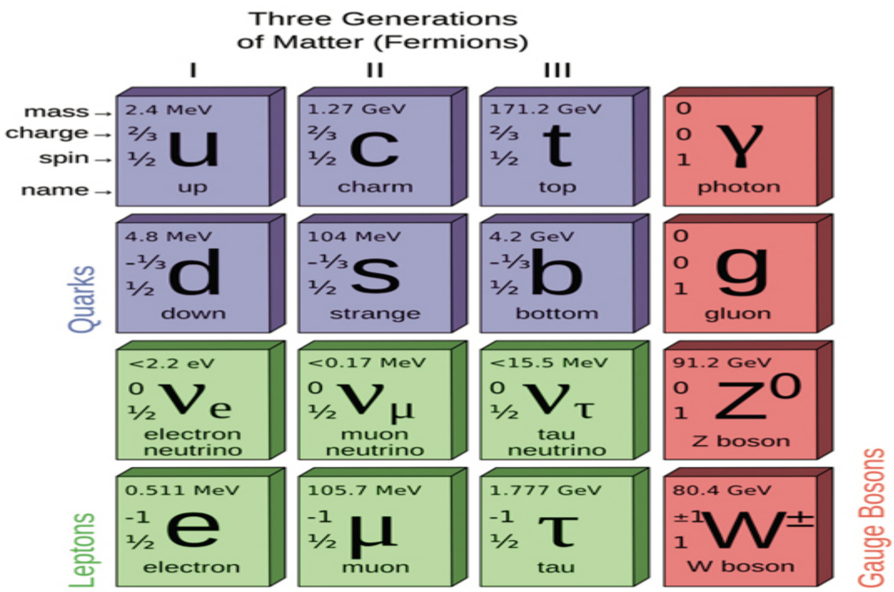

Figure 1.1: Six quarks include up, down, strange, charm, top and bottom. Six leptons are the electron, electron neutrino, muon, muon neutrino, tau and tau neutrino. The gauge bosons are photon, gluon, z boson and w boson. Image Source: [4]

except the dark matter. The dynamics of these particles are governed by interactions, mediated by another class of particles, known as gauge bosons [5].

The weak interactions are short ranged and with low interaction strength. The mediators of these forces are heavy and short-lived $W^{\pm}$ and Z vector bosons. The quantum electrodynamics (QED) governs the electromagnetic interaction, which is a long (infinite) range force because of the massless charge carrier particle, known as “photon”.

The quantum chromodynamics (QCD) which shares a common analogy to the QED in terms of particle's charge and mediator boson is the theory of strong interaction which is responsible for the existence of nuclei and composite particles. The six flavours of quark are categorized in three generations: the “up quark” (u) and the “down quark” (d) form the first generation, the “charm quark” (c) and “strange quark” (s) form the second generation and the “top quark” (t) and “bottom (or beauty (b)) quark” form the third generation [6]. Out of these, only the light “up” and “down” quarks form the key constituents of stable visible matter. Quarks come with three different “color” charges analogous to “electric” charge in QED and the quark composition in a composite system (exception is quark-gluon plasma (QGP)) or particle is always colorless (quark confinement). The strong force is very short ranged with high interaction strength which is mediated by gluons carrying the "color" charges. These gluons are available in 8 physical gluonic states which forms a color-SU(3) octet [1]. The interaction strength of strong force between quarks ($\alpha_s = g^2/4\pi$, where g is effective coupling constant) is very different from other interactions, a colorless particle becomes asymptotically weaker when energy increases or distance decreases, this gives rise to a unique feature of QCD called the asymptotic freedom. It was discovered and described in 1973 by Frank Wilczek and David Gross and separately by David Politzer in the same year. The discovery of asymptotic freedom in the theory of the strong interaction facilitate them the shared Nobel Prize of physics in 2004 [7]. The Fig. 1.2 shows the QCD coupling constant given below as a function of momentum transfer along with experimental data versus theoretical prediction.

$$\alpha_s(Q) = \frac{1}{(33 - 2N_f)\ln(Q^2/\Lambda^2_{QCD})} \tag{1.1}$$

where Q is the energy exchange and N_f is the number of quarks and flavours. The Λ_{QCD} is a scale factor. Thus, quarks interact strongly at low energy (high momentum transfer) and consequently, perturbative calculations are not allowed due to large coupling constant which introduces divergence in the perturbative expansions. The Λ_{QCD} simply defines the scale for strong interaction physics dividing it into two regimes; one, with low energy non-perturbative QCD (Effective Theory) and other with high energy QCD where perturbative calculations are still valid.

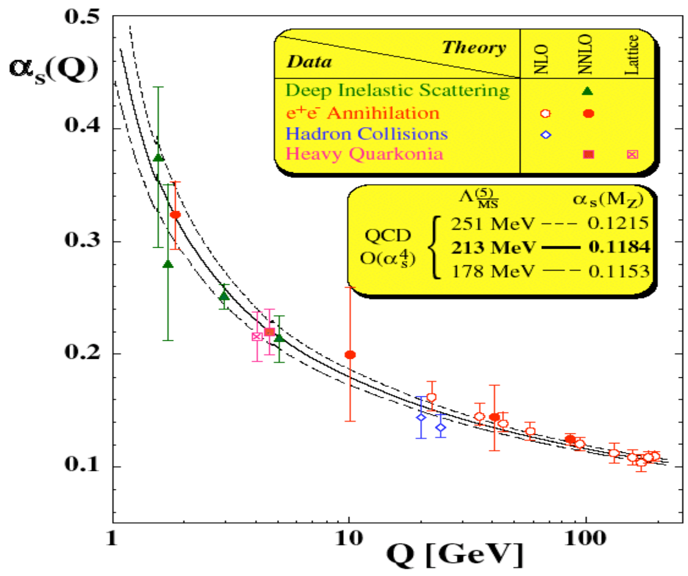

Figure 1.2: The QCD coupling constant vs the energy exchange for various experimental data and theoretical predictions. Image Source: [9]

1.3 Hadrons

The hadrons are colorless particles that are made of two or three quarks. The hadrons with three quarks result into a colorless state called baryons, whereas, a hadron formed by a quark and anti-quark pair is called a meson. These quark contents of a particle allow SM to assign quantum numbers to the hadrons and often denoted as J^{PC}. Here J = L+S is the total angular momentum containing orbital angular momentum L and spin S, while the parity is denoted by P = $(-1)^{L+1}$ and charge conjugation by C = $(-1)^{L+S}$ [10]. The SM model explains all hadrons observed in nature as a combination of different quarks and the interactions holding them together.

The mesons can be further classified depending on the J and P shown in Table 1.1. The present work, however, is focused on understanding pseudoscalar meson. The pseudoscalar mesons form an SU(3) group representation, through a combination of light quarks (u,d,s) and thus, producing nine different states which are further grouped in an octet and a singlet state. The nonet of the pseudoscalar mesons are shown in Fig. 1.3, where the charge (Q) increases towards the right and the strangeness (S) increases towards the upward direction.

Table 1.1: The table shows different types of mesons depending on their quantum numbers.

Type	S	L	P	J	J^P
Scalar Meson	1	1	+	0	0^+
Pseudoscalar Meson	0	0	-	0	0^-
Axial Vector Meson	0	1	+	1	1^+
Vector Meson	1	0	-	1	1^-
Tensor Meson	1	1	+	2	2^+

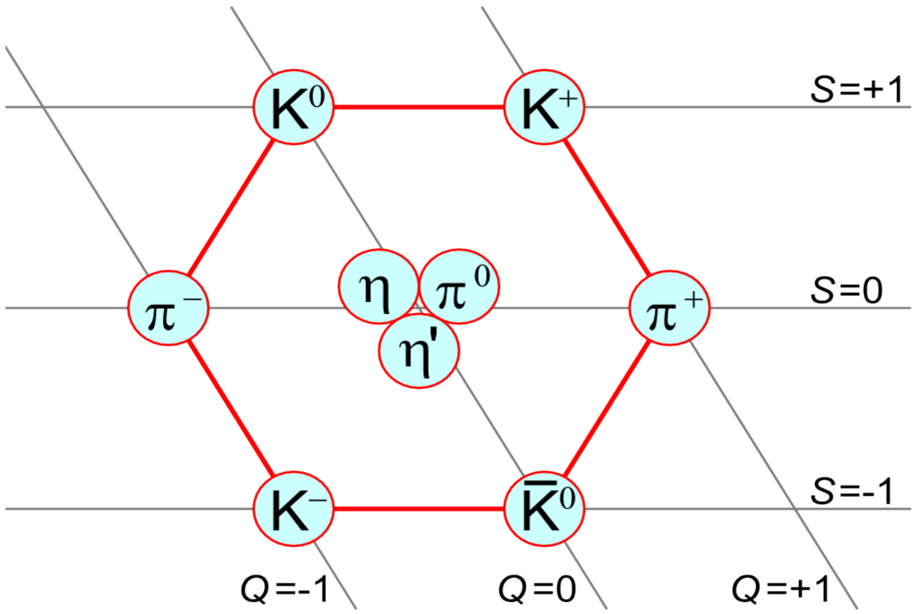

Figure 1.3: The nonet of pseudoscalar mesons.: [11]

1.3.1 η' pseudoscalar meson

The η' meson is the heaviest pseudoscalar meson with a mass of 957.78 $\pm$ 0.06 MeV/c^2, decay width (τ) of 0.196 $\pm$ 0.0009 MeV and configuration $J^{PC} = 0^{-+}$. The η' meson is not a pure singlet or an octet, rather it is a linear combination of the singlet (η_1) and octet (η_8) state and the θ is the mixing angle.

$$\eta_1 = \frac{\mathrm{u\bar{u}} + \mathrm{d\bar{d}} + \mathrm{s\bar{s}}}{\sqrt{3}} \tag{1.2}$$

$$\eta_8 = \frac{\mathrm{u\bar{u}} + \mathrm{d\bar{d}} - 2\mathrm{s\bar{s}}}{\sqrt{6}} \tag{1.3}$$

$$\eta' = \cos(\theta).\eta_1 + \sin(\theta).\eta_8 \tag{1.4}$$

Table 1.2: Major decay modes of η' meson.

Decay modes of η'	Branching Ratio (%)
$\pi^+ \pi^- \eta$	42.6 ± 0.7
$\rho \gamma$ (including non-resonant $\pi^+ \pi^- \gamma$)	28.9 ± 0.5
$\pi^0 \pi^0 \eta$	22.8 ± 0.8
$\omega \gamma$	2.62 ± 0.13

1.3.2 η' decay modes

The $\eta' \rightarrow \eta \pi^+ \pi^-$ decay is the dominant decay mode of the heaviest pseudoscalar meson η'. The major decay modes of η' meson are shown in Table 1.2 [12]. The study of the prominent decay mode can help to understand the quark contents, general behaviour pseudoscalar meson, quark mass ratios and thereby allowing one to develop a theory which works at low energy non-perturbative QCD regime. The decay width for $\eta' \rightarrow \eta \pi^+ \pi^-$ modes can be written as:

$$\tau(\eta' \rightarrow \eta\pi^+\pi^-) = \frac{1}{2.m_{\eta'}} \int \mid M \mid^2 d\phi \tag{1.5}$$

where phase space volume element is dϕ and M is the matrix containing interactions. The masses of the intermediate σ (550 MeV), f_0 (980 MeV) and a_0 (983.5 MeV) resonances are either less than or comparable to η' meson mass [13]. The contributions of these resonances in the decay can be represented by Feynman diagrams shown in Fig. 1.4.

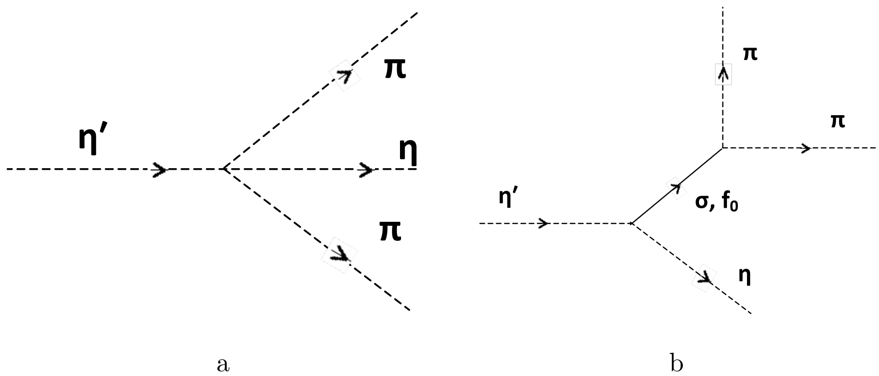

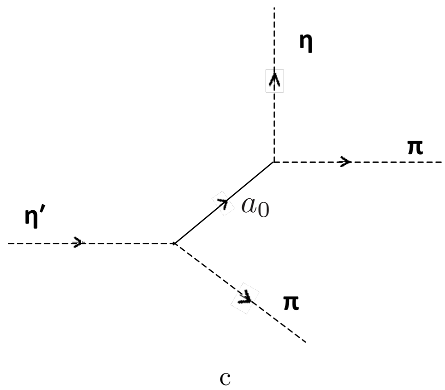

Figure 1.4: The Feynman diagram showing different ways in which the decay of $\eta' \rightarrow \eta\ \pi^+\ \pi^-$ can occur (a) the non-resonant decay, (b) decay with scalar σ and f_0 meson resonances and (c) with scalar a_0 meson resonance [13].

1.4 Chiral Perturbation Theory (ChPT) for Pseudoscalar Meson

The chirality is a symmetry where the left-handed and right-handed operations are observed independently. The ChPT is an elegant theory which provides a framework to study the mesons at very low energies, and the chiral symmetry acts as an exact symmetry and valid for non-perturbative QCD. The chiral symmetry is a very useful concept and applicable to quarks u, d and s as they have small masses and takes part in low-energy hadronic interactions. In this effective theory, the Lagrangian has a $SU(3)_L \times SU(3)_R$ chiral symmetry. This symmetry, when broken in the ground state, gives the eight massless Goldstone bosons: ($\pi^{\pm,0}$, $K^{\pm}$, K^0, $\bar{K^0}$, η) [14], as expressed in equation 1.6. These eight massless bosons serve as the effective degrees of freedom for the theory instead of the most fundamental particles, the quarks and the gluons. Within the theory, the pseudoscalar mesons gain their masses from the spontaneous breakdown of the chiral symmetry. The Lagrangian ($\mathcal{L}$) during the spontaneous breakdown of the chiral symmetry changes its symmetry from $SU(3)_L \times SU(3)_R$ to $SU(3)_V$.

$$\mathcal{L}_{QCD}(q, \bar{q}, g) \rightarrow \; Effective \; theory \; \rightarrow \mathcal{L}_{ChPT}(\pi, K, \eta) \tag{1.6}$$

These processes can be defined with the Feynman tree-level diagrams and the expansion of the Lagrangian is in order of momenta which saves the theory from being divergent. The expansion of the Lagrangian where subscripts refer to the order of momentum is given below:

$$\mathcal{L}_{ChPT} = \mathcal{L}_2 + \mathcal{L}_4 + \mathcal{L}_6 + ... \tag{1.7}$$

The lowest order of the Lagrangian ($\mathcal{L}_{ChPT,LO}$ or $\mathcal{L}_2$) in ChPT is given by

$$\mathcal{L}_{ChPT,LO} = \frac{F_\pi^2}{4}(\partial_\mu U^\dagger \partial^\mu U) + \frac{F_\pi^2 B_0}{2} tr(M(U^\dagger + U)) \tag{1.8}$$

where F_π is pion decay constant, has a value of 92.2 MeV in the chiral limit, B_0 is a constant appearing in the mass term of the pseudoscalar mesons, U is the unitary matrix given below:

$$U(\Phi) = \exp(i\Phi/F_\pi)\phi = \begin{bmatrix} \pi^0 + \frac{1}{\sqrt{3}}\eta & \sqrt{2}\pi^+ & \sqrt{2}K^+ \\ \sqrt{2}\pi^- & -\pi^0 + \frac{1}{\sqrt{3}}\eta & \sqrt{2}K^0 \\ \sqrt{2}K^- & \sqrt{2}\bar{K}^0 & \frac{2}{\sqrt{3}}\eta \end{bmatrix} \tag{1.9}$$

and M is the quark matrix, M $= \begin{bmatrix} m_u & 0 & 0 \\ 0 & m_d & 0 \\ 0 & 0 & m_s \end{bmatrix}$

Some of the applications of lowest order Lagrangian $\mathcal{L}_2$, which considers the simplest tree-level diagrams, are $\pi^+ \rightarrow \mu^+ \ \nu_\mu$ decay and $\pi - \pi$ scattering. Similar applications of $\mathcal{L}_4$ and $\mathcal{L}_6$ can also be found in the references [15, 16].

The observed mass of the η' meson in nature is much higher than the other pseudoscalar mesons, which is due to axial U(1) anomaly [17, 18]. The axial U(1) anomaly of the QCD Lagrangian prevents the corresponding pseudoscalar singlet from being a Goldstone boson and in fact, the anomaly suggests that lightest pseudoscalar candidate should be the η' meson, which is not the case. So, a conventional ChPT does not include the η' meson. One of the way to include η' meson is extending the chiral $SU(3)_L \times SU(3)_R$ symmetry to $U(3)_L \times U(3)_R$ as shown in Fig. 1.5. The ChPT calculations using a tree level diagram do not seem to explain the experimental observables from the Lagrangian $\mathcal{L}_2$ only. So, one has to look for the higher order of the Lagrangian, and hence the tree level diagrams from the Lagrangian $\mathcal{L}_4$ and loops with vertices from $\mathcal{L}_2$ along with a framework of large N_c ChPT [19] are discussed. The fourth order Lagrangian $\mathcal{L}_4$ is given by,

$$\mathcal{L}_4 = \frac{N_c}{192\pi^2} Tr\{\frac{1}{2}[U^\dagger \partial_\mu U, U^\dagger \partial_\nu U]^2 + (\partial_\mu (U^\dagger \partial_\mu U)^2 - 2(\partial_\mu (U^\dagger \partial_\mu U)))^2\} \tag{1.10}$$

So far the η' meson description is exclusively taken care within the effective theory. The Lagrangian can then be modified to take care of hadronic decay mode $\eta' \rightarrow \eta \ \pi^+ \ \pi^-$. Where, the $\mathcal{L}_4$ gives the major contribution which is given below:

$$\begin{aligned} \mathcal{L}_{int} =& \frac{N_c}{192\pi^2} \frac{2}{F_\pi} \frac{(\cos(\theta) - \sqrt{2}\sin(\theta))(\cos(\theta) + \sqrt{2}\sin(\theta))}{6} \times \\ & \{\partial_\mu \eta' \partial_\mu \eta \partial_\nu \pi . \partial_\nu \pi + 2 . \partial_\mu \eta' \partial_\nu \eta \partial_\mu \pi . \partial_\nu \pi\} \end{aligned} \tag{1.11}$$

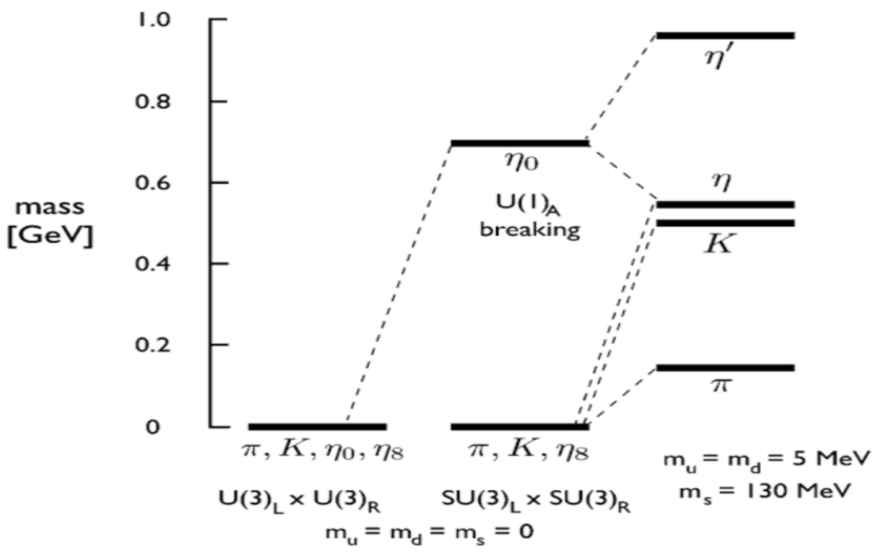

Figure 1.5: Pictorial presentation of symmetry breaking in the pseudoscalar meson nonet. Image Source: [20]

The decay rates of $\eta' \to \eta\ \pi^+\ \pi^-$ and $\eta' \to \eta\ \pi^0\ \pi^0$ can be measured using equation 1.11. The decay rates are $\tau(\eta' \to \eta\ \pi^+\ \pi^-) = 195$ keV and $\tau(\eta' \to \eta\ \pi^0\ \pi^0) = 105$ keV [21]. The investigation of these decays with the U(3) ChPT up to fourth chiral order including one-loop corrections produces $\tau(\eta' \to \eta\ \pi^+\ \pi^-) =$ 84.4 keV and $\tau(\eta' \to \eta\ \pi^0\ \pi^0) = 42.2$ keV [2], which are close to the experimental measurements of $\tau(\eta' \to \eta\ \pi^+\ \pi^-)$=90 $\pm$ 8 keV and $\tau(\eta' \to \eta\ \pi^0\ \pi^0) = 42 \pm 4$ keV [22]. These comparisons show the genuineness and are the reason behind the acceptability of ChPT.

The ChPT Lagrangian straight away produces the $\eta' \to \eta\ \pi^+\ \pi^-$ decay amplitude. In this thesis, the experimental measurement of $\eta' \to \eta\ \pi^+\ \pi^-$ decay amplitude is studied, which is accessible by studying the decay amplitude of Dalitz plot phase-space and parameterized to quantify and compare with the theoretical calculations.

1.5 Dalitz Plot for a Three Body Decay

A three body decay of the $\eta' \to \eta\ \pi^+\ \pi^-$ can be specified with three final state four-vectors P^μ_η, $P^\mu_{\pi^+}$ and $P^\mu_{\pi^-}$ for each final state scalar particle. The three four-

Table 1.3: The number of degrees of freedom for a meson undergoing three body decay to scalar particles.

Constraints	Degrees of freedom
3 four-vectors	12
4-momentum conservation	-4
3 masses	-3
3 Euler angles	-3
Total	2

vectors produce 12 parameters, however, the three body decay also has constrains shown in Table 1.3. Therefore, we see that the three body decay of the meson leaves two degrees of freedom to explain the phase-space of the decay.

A Dalitz plot is a scatter plot introduced by Richard Dalitz. One of the important achievement of the earlier time was that the Dalitz plot could solve the "τ-θ puzzle" of particle physics. The two particles with the same masses and lifetimes with a violation of the parity conservation (P) in the decay mode, were long thought to be two different particles. Finally, a Dalitz plot resolved it. Today we identify both states with K^+ where the parity symmetry is broken. A Dalitz plot where the variables are the function of the decaying particle masses with very less number of events is called an "Old Dalitz plot" [23]. The primitive application of these plots was to know the spin and the parity of the decaying particle, which resulted in information like intermediate resonances and identification of particles. With the advancement of experimental capabilities, Dalitz plots are now produced with a large number of events and low statistical fluctuations, referred as "new Dalitz plot", which are capable of enhancing even the slightest variations in the event distribution. These modern Dalitz plots are quantified with different parameterizations and evaluated for precise determination of the parameters. This information serves as inputs to problems in hadronic spectroscopy. The parameters allow one to study and understand resonances, predict effective potentials, intermediating particles and interactions in the decay. Physical observables like decay width, phase shifts, quark mass ratio and parameters quantifying interactions can also be calculated from the Dalitz plot parameters [24–27].

In the current measurement of the Dalitz plot containing purely kinematic informations of the phase-space is described using two variables X and Y given by,

$$X = \frac{\sqrt{3}(T_{\pi^+} - T_{\pi^-})}{Q} \tag{1.12}$$

$$Y = \frac{(m_\eta + 2m_\pi)}{m_\pi} \cdot \frac{T_\eta}{Q} - 1. \tag{1.13}$$

Where, T_η, T_{π^+}, and T_{π^-} are the kinetic energies of the particles η, π^+ and π^-, respectively, in the rest frame of the η' meson and Q = T_{π^+}+T_{π^-}+T_η, m_η and m_π are the mass of η and π mesons, respectively. The Dalitz plot of $\eta' \to \eta$ π^+ π^- decay is shown in Fig. 1.6. The information of any decay is accessible by studying the amplitude of the phase-space. So, the decay amplitude of Dalitz plot phase-space is parameterized with the general parameterization function given in equation 1.14.

$$f(X, Y) = M^2 = A(1 + aY + bY^2 + cX + dX^2). \tag{1.14}$$

Where, a, b, c, and d are the Dalitz plot parameters of the decay and A is the normalization constant.

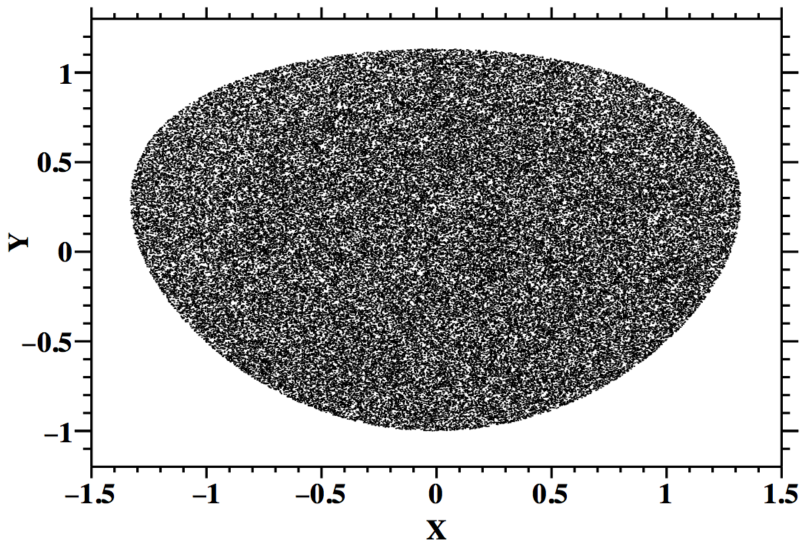

Figure 1.6: Dalitz plot distribution for the decay of $\eta' \to \eta$ π^+ π^-.

1.6 Present Status

Current status of experimental data on $\eta' \to \eta\ \pi^+\ \pi^-$ decay is based on the following: the VES Collaboration, which has reported the Dalitz plot parameters of $\eta' \to \eta\ \pi^+\ \pi^-$ with 14.6×10^3 events in charge exchange (π^- p $\to \eta'$ p) and 7×10^3 events in diffraction like production (π^- N $\to \eta'\ \pi^-$ N) [28], the BESIII Collaboration has also reported $\eta' \to \eta\ \pi^+\ \pi^-$ decay parameters in $e^+\ e^- \to \pi^+\ \pi^-$ J/$\psi \to \eta'\ \gamma$ with 43826 $\pm$ 211 events [29] with better precision compared to VES. There are also calculations from theory using U(3) chiral unitary approach [24] and U(3) chiral effective field theory in combination with a relativistic coupled-channels approach [30]. The two measurements disagree with each other and with the theoretical calculation of the parameters [30]. The previous experimental measurements and theoretical calculations are shown in Fig. 1.7.

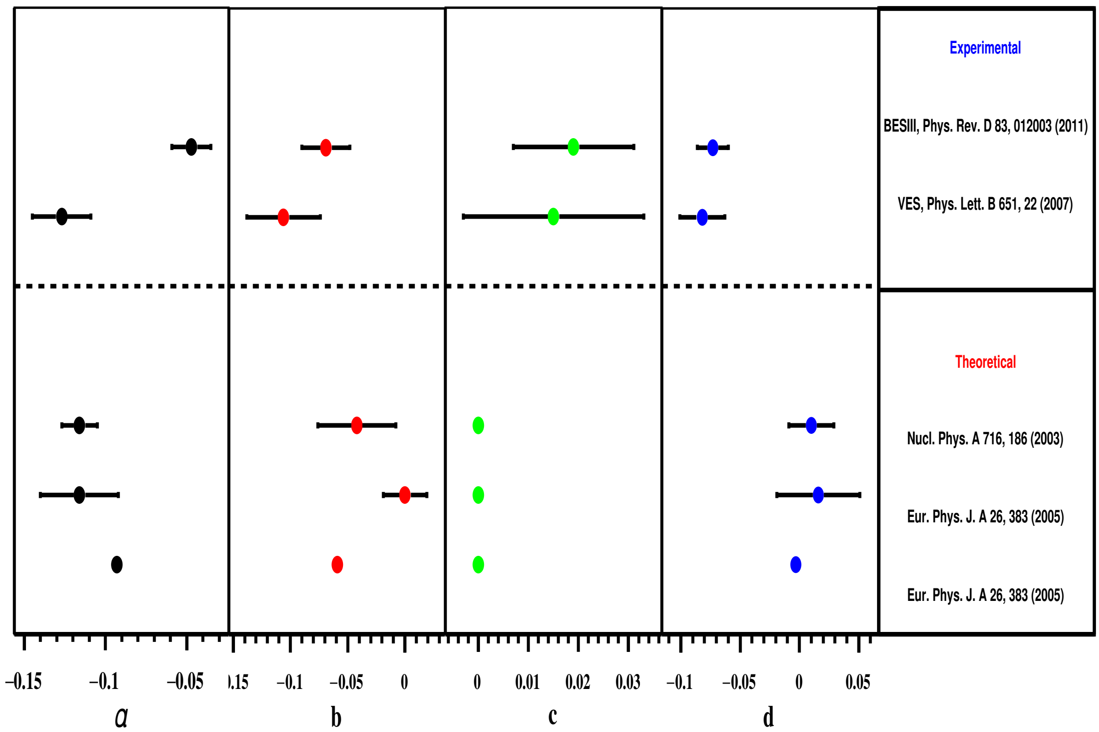

Figure 1.7: Comparison of different experimental and theoretical calculations for Dalitz plot parameters of $\eta' \to \eta\ \pi^+\ \pi^-$ decay.

In this thesis, we present results of Dalitz plot analysis of the decay $\eta' \to \eta\ \pi^+\ \pi^-$ from the CLAS *g12* dataset. The analysis is based on more than 1.5K events of photoproduction and subsequent decay of $\eta' \to \eta\ \pi^+\ \pi^-$, which has the competitive statistics to study the parameters with reduced statistical errors. It is a complementary independent measurement to cross-check the parameters with almost an order of magnitude higher statistics.

Chapter 2

Experimental Setup

The Dalitz plot analysis of $\eta' \to \eta\ \pi^+\ \pi^-$ decay is done with events collected by the *g12* run data recorded at Thomas Jefferson National Accelerator Facility or Jefferson Lab (JLab) located in Newport News, Virgina, USA. This high statistical data provided the reaction γ p $\to$ (η') p $\to$ (η) $\pi^+\ \pi^-$ p for the Dalitz plot analysis, where the particles in parenthesis are not directly detected.

JLab is a national laboratory of United States, funded by the U.S. Department of Energy (DOE) and it has a motto of “Exploring the nature of matter”. JLab has Continuous Electron Beam Acceleration Facility (CEBAF) accelerator with three experimental halls (A, B, and C) in the facility. The Ariel view of the JLab is shown in Fig. 2.1 and very recently, the accelerator beam energy has been upgraded to 12 GeV and a new experimental hall (D) has been developed. The production of the high-quality photon beam for the experiment is achieved using CEBAF accelerator and finally obtained in the hall-B.

This chapter will cover the details of the experimental facility directly related to the analysis. It includes the CEBAF accelerator, hall B photon tagger, the CLAS detector and subdetectors, Triggers and data acquisition. Additionally, it will also explain how the raw data from various subdetectors are interpreted and prepared for performing data analysis.

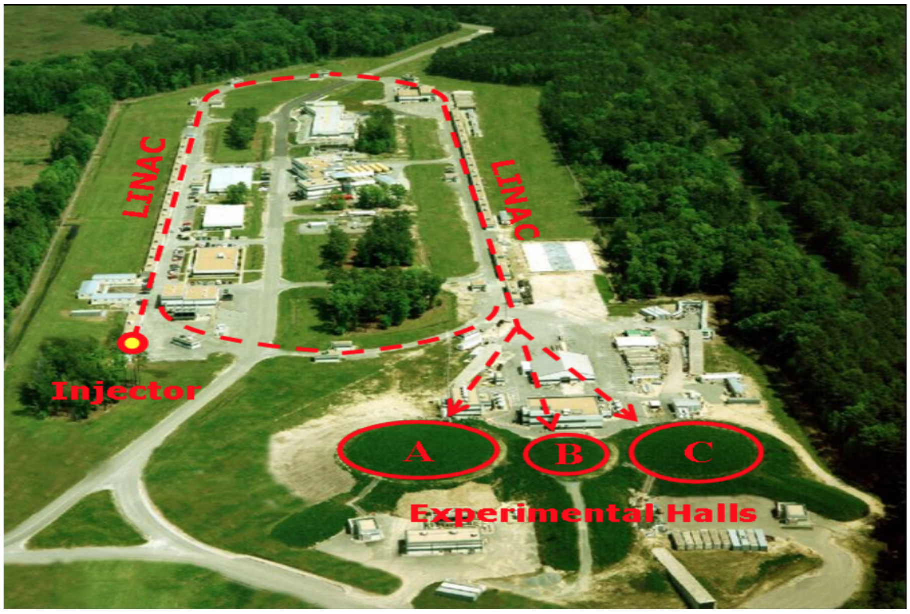

Figure 2.1: Bird's-eye view of the JLab accelerator site. Image Source: [31]

2.1 CEBAF Accelerator

The CEBAF at JLab provides polarized electron beam of up to 6 GeV with an average current of up to 200 A to all the experimental halls. The polarized electron source from the injector is circulated in the racetrack shaped accelerator of 1.4 km in length with a pair of superconducting linear accelerators (LINAC) connected to each other by two arc sections that also contain steering magnets.

The injected electrons come from electron gun with a laser which radiates the GaAs photocathode system and produces the bunches of electrons. The electron gun has three lasers, one for every experimental hall thus giving the freedom to choose polarizations and control current for the experiments at different hall. The incident laser is pulsed at every 2 ns and then passed through an optical chopper to improve the separation of the bunches by 667 ps in time and 90 m in length. Both the LINAC's have 168 Superconducting Radio Frequency (SRF) Niobium (Nb) cavities as shown in Fig. 2.2. The superconductivity is achieved by liquid helium refrigeration of Nb cavity to a temperature of approximately 2.1 K, at this temperature the Nb looses electrical resistance and behaves as a superconductor. Klystrons are used to make radio frequency (RF) standing waves inside these cavities thus creating the accelerating potential for the electrons. The whole subsystem is synchronised in a way to give an overall frequency of 1497

MHz to the RF waves inside the cavity.

The two arc sections have in total 9 recirculating arcs, the electron bunch once inside the LINAC can be passed up to five times completing passages through all the 9 recirculating arcs to achieve maximum energy of 6 GeV. The beam energy in each hall can be controlled by choosing the number of laps of electron bunches. The electrons from the accelerator are then passed to all the three halls simultaneously and the RF-timing of the electron beam bunch is also recorded [33] before sending it to the halls. The schematics of the CEBAF accelerator with different components are shown in Fig. 2.3.

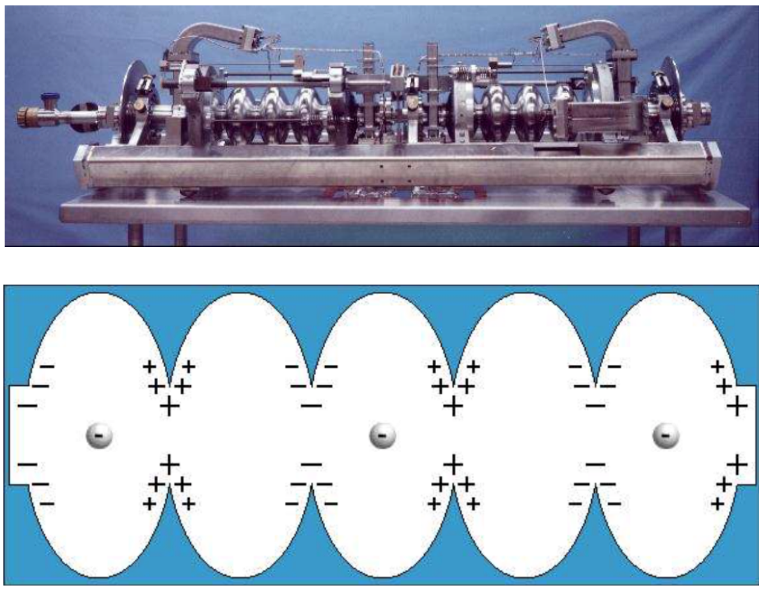

Figure 2.2: A pair of typical CEBAF superconducting cavity (top), and the accelerator has 338 such cavities. A pictorial representation of the standing wave inside the cavity (bottom) through which the electron bunch propagates. Image Source: [32]

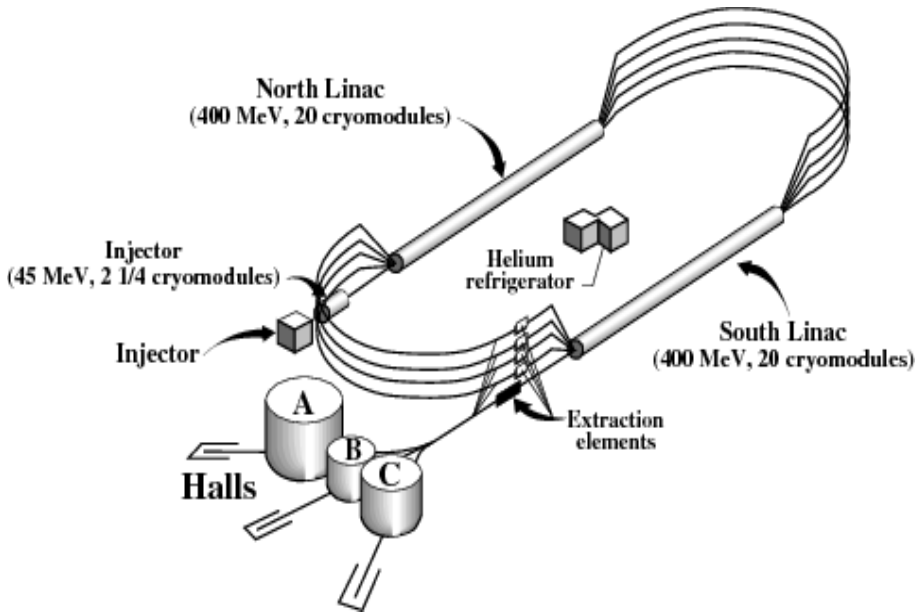

Figure 2.3: The CEBAF along with the position of installed components in the facility. Image Source: [31]

2.2 Hall B Photon Tagger

The experimental hall B is the house to the CLAS experiment where the *g12* run data is taken. The hall B serves to convert the electrons into photons through the bremsstrahlung process and it also tags those photons which are used later in the experiment. The complete diagram of Photon Tagger system with the sub-parts is shown in Fig. 2.4. The electron beam from the CEBAF facility passes through a gold (Au) foil radiator of 10^{-4} radiation length. The prime reason behind choosing Au is that it has a heavy nucleus which produces sufficient Coulomb field for the incoming electrons. The interaction of an electron with the nucleus results in the production of photons thus decelerating electrons and transfer of some negligible energy to the gold atom.

A dipole magnet of 1.75 T separates the deviated electrons while the photons remain undeflected. The dipole magnet with its field strength is constructed in a way that it throws electrons which do not radiate to follow a circular arc directed into a shielded beam dump below the floor of hall B. However, the interacted electrons curl depending on momentum and magnetic field, and finally moves toward the scintillator hodoscope along the flat focal plane downstream. The curling of electrons gives it a characteristic angle depending on the energy of an electron.

A scintillator hodoscope along the flat focal plane downstream detects the scattered electrons, and it consists of two separate planes of scintillator detectors. The first detector plane is called the E-plane, where E denotes the energy. This plane contains 384 narrow scintillator paddles of 20 cm in length, 4 mm thick and range from 6 to 18 mm in width. These paddles are arranged in an overlapping fashion and give the energy resolution of the E-plane which is 0.1% of the incident electron beam energy. Consequentially, the electron energy can be measured by knowing the paddle position through which an electron passed, and thereby allows the determination of the radiated Bremsstrahlung photon E_γ energy via. simple energy conservation as:

$$E_\gamma = E_{CEBAF} + E_{Scattered}$$

where E_{CEBAF} is the electron energy from the CEBAF and $E_{Scattered}$ is the measured electron energy from the E-planes. About 20 cm beneath the E-plane there is also another set of planes called the T-plane to measure the timing information. This scintillator plane has 61 paddles, and each paddle is 2 cm thick and provides a time resolution of 110 ps. The paddles are organized into two groups, the first has 19 narrower counters spanning the photon energy range from 75% to 95% of the incident electron energy, and the second group has 42 counters spanning the range from 20% to 75%. The paddle widths along the plane are varied to compensate for the $1/E_\gamma$ behavior of the bremsstrahlung process so that the counting rate remains constant. The timing resolution obtained from these counters is of the order of 110 ps, and within this resolution it is possible to identify and tag the photons using the T-plane information along with RF-timing information from the electron beam bunch. The T-plane information is also crucial to calculate the event vertex or the interaction time, and the instant of time when all the particles produced after interaction left the target. Photons in the energy range from 20% to 95% of the electron beam energy can be tagged by this photon tagging system and is shown in Fig. 2.5 along with the position of the counters. Finally, a collimation system with interspaced sweep magnets clean up any charged particle background generated in the collimator walls, before the photon beam proceeds toward the target cell. A detailed information of the hall B photon tagging system is explained in the paper [33].

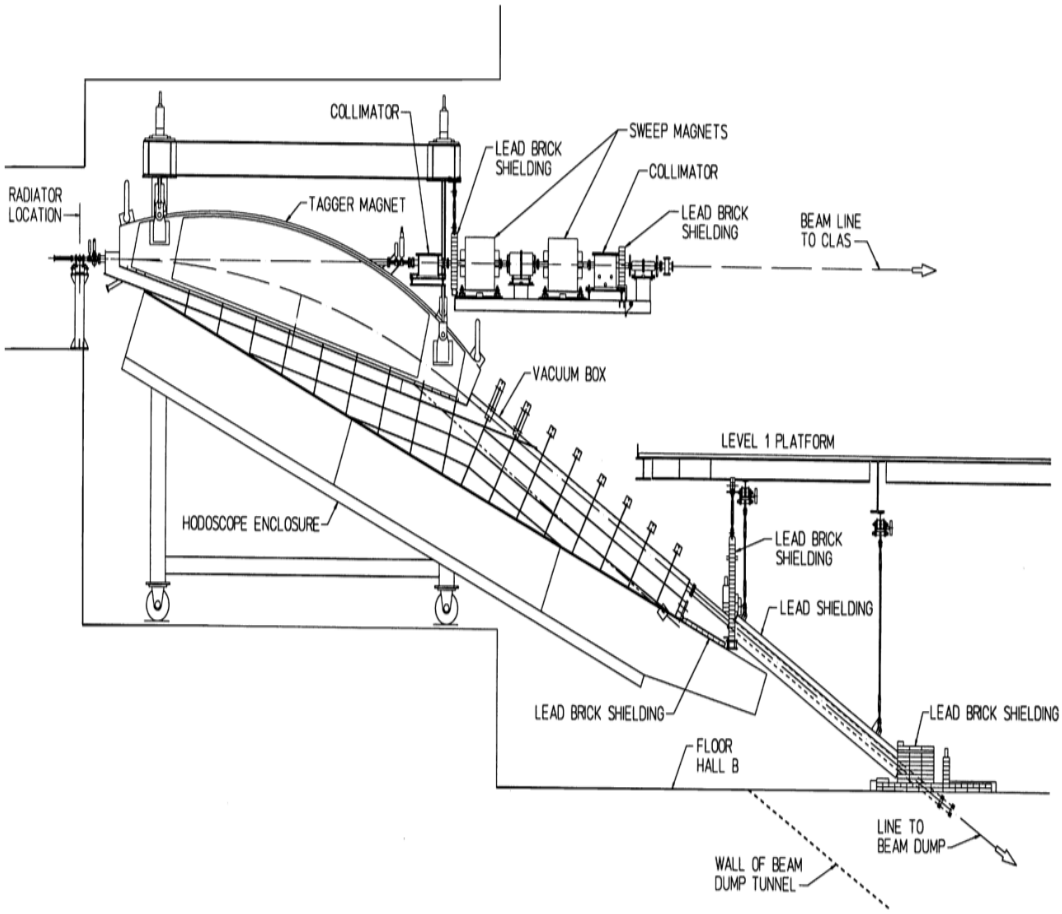

Figure 2.4: A complete assembly of the hall B Tagger system with the location of the radiator, hodoscope enclosure, collimators, shielding, and beam dump entrance. Image Source: [33]

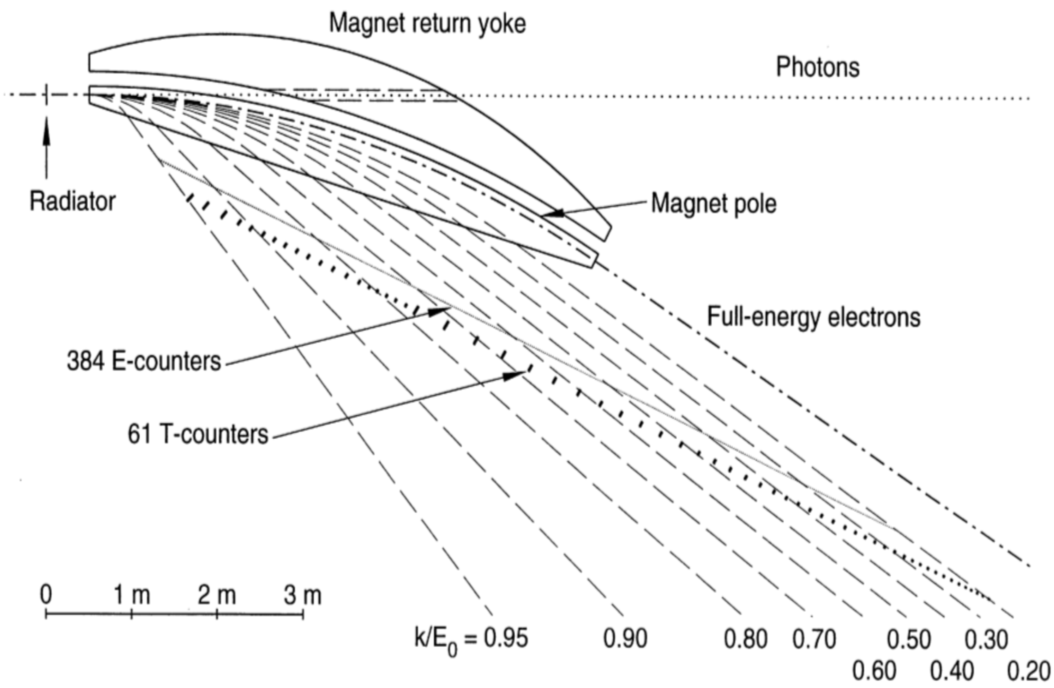

Figure 2.5: The photon tagging system with the position of E and T counters, along with the measured electron energy range. Image Source: [33]

2.3 CLAS Detector

The CLAS detector [34] is placed inside the Experimental hall B. It is an onion-shaped detector with different layers of subdetector. Considering the CLAS detector geometry in spherical coordinate where beam direction being the z-axis, the azimuthal angle divides the detector as six different identical and independent sectors. The CLAS detector along with the subdetectors are shown in Fig. 2.6. The CLAS detector is specially optimized for detection of charged particles with $\approx 3\pi$ coverage with a radius of 4 m. The different subdetectors along with the experimental target are described in this section and are also listed below:

1. *g12* Target Cell

2. Start Counter

3. Superconducting Toroidal Magnet

4. Drift Chambers

5. Time of Flight

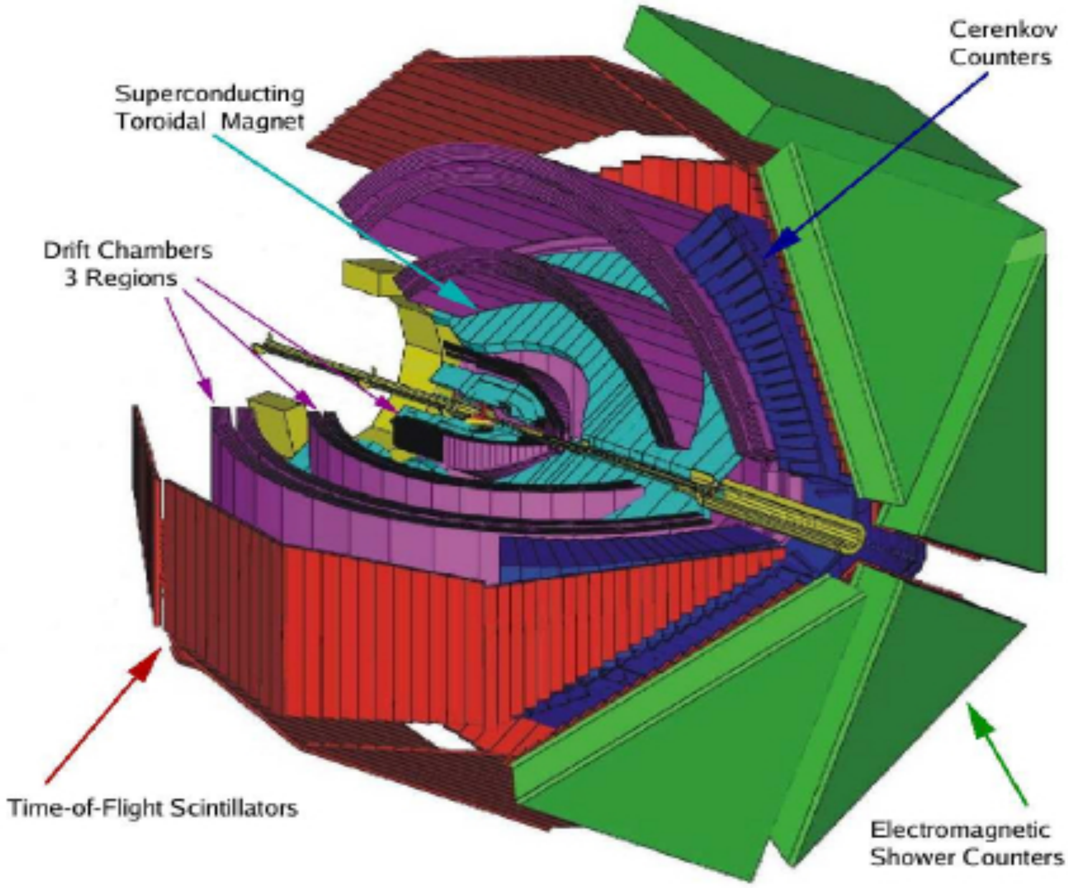

Figure 2.6: The CLAS detector along with the position of various subdetectors. Image Source: [35]

2.3.1 *g12* Target Cell

A cylindrical cell of 40 cm in length and 4 cm in diameter filled with unpolarized liquid hydrogen (lH_2) is used as a fixed target, which served atomic protons as the target to the experiment. The geometry of target cell is shown in Fig. 2.7. The cell body is made of Kapton which is 5 μm thick and the two ends are made of Aluminium. In the *g12* experiment, the Target Cell was placed 90 cm away from the CLAS center.

2.3.2 Start Counter

Start Counter measuring the start time (ST) entirely surrounds the target region and it is the first detector encountered by the particles after the interaction. It

Figure 2.7: The target cell used for the *g12* run. Image Source: [36]

has a length which is equal to the target length of 40 cm, and there is a total of 24 scintillator paddles divided into the six sectors of CLAS. Each independent CLAS sector has four such independent scintillator paddles, and all the scintillator paddles are bent inward around the downstream end of the target to provide total coverage. The signal from the scintillator paddles is collected by the phototubes attached to the upstream ends as shown in Fig. 2.8. The acrylic light guides taper is connected to a photomultiplier tube (PMT). The PMT signals from the 24 start counter are sent to ADC's and CAMAC discriminator and the discriminated output finally reaches to the trigger logic in order to get recorded. The hexagonal support shell holds the six sectors mounted on them independently, while the other accessories like base with the flange, the light guides, PMT's and housings were placed in a way that it does not block the good and useful acceptance region of CLAS detector. The time resolution calculated for the subdetector comes out to be < 380 ps.

The timing information from the Stant Counter is very important to this analysis as it allows to calculate the velocity of the produced particle by knowing timing difference and distance between the TOF and ST. The timing information from Stant Counter, timing counters of the tagger and RF also helps to calculate more important information like the events and particles production vertex, correct beam photon associated with an event etc. The logic of the timing counters of the tagger with the ST allows users of the facility to record only events within a certain photon energy range.

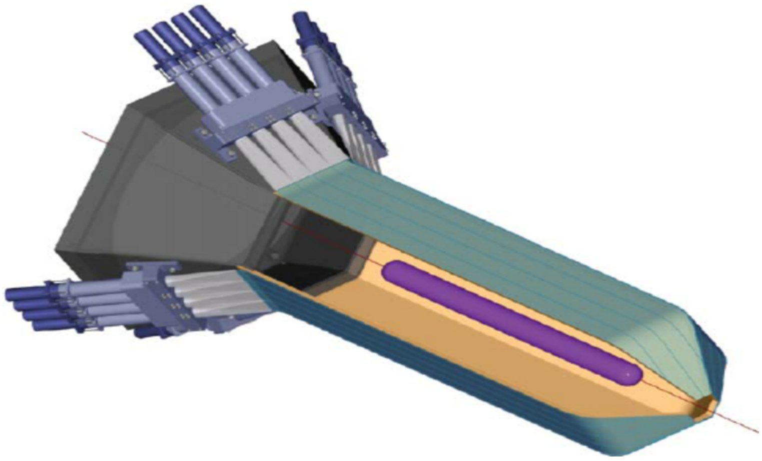

Figure 2.8: Start counter surrounding the target cell and connections of the photomultiplier tube. Image Source: [37]

2.3.3 Superconducting Toroidal Magnet

One of the most crucial parts of the detector is the superconducting toroidal magnet which produces the magnetic field inside the detector. The charged particles produced after the interaction experiences the magnetic field. The field deviates the particles from its linear trajectory depending on the strength and direction of field. From the deviated trajectory along with the help of the tracking detectors, the momentum of the particle is computed. Charged particle when suffer magnetic field, it bend outwards laterally, and so the possibility of a crossover from one sector to the other is minimal. In the default or normal field mode, the positively charged particles bend backward and negatively charged particles bend forward. The strength varies downstream as well as radially. The highest magnetic field strength is in the forward direction behind the target and near the beamline and it is lower in the downstream region and further away from the detector in the radial direction as shown in the map given in Fig. 2.9. The magnet subsystem has six kidney-shaped superconducting torous coils arranged around the beamline and are separated by each other azimuthally by 60°. The magnet on a whole is approximately 5 m in diameter. Each of the six coils has four layers of 54 windings of aluminum and is kept at a superconducting temperature of ≈ 4 K using CEBAF helium refrigerator.

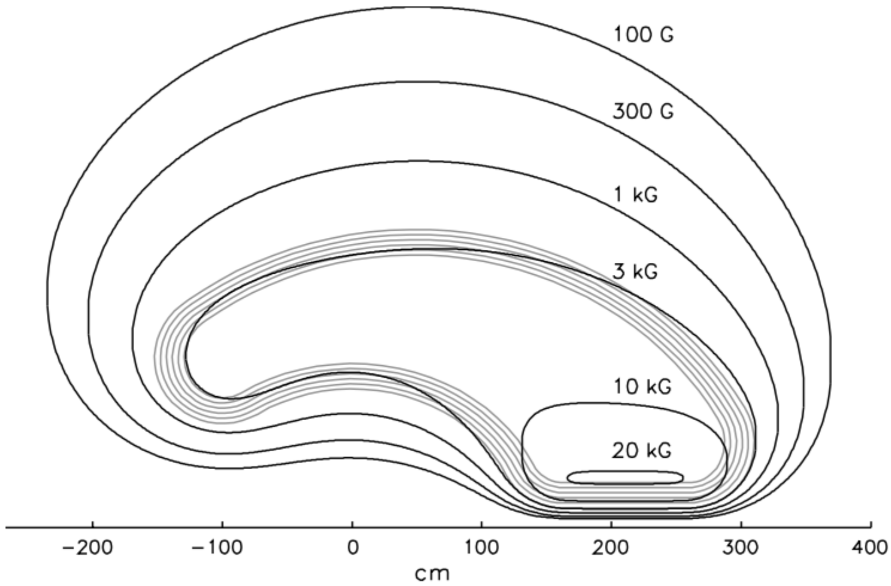

Figure 2.9: Contours of a constant absolute magnetic field for the CLAS toroid in the midplane between two coils. The strength of the CLAS magnetic field (kG), at the azimuthal center of a sector versus radial distance from the beamline z coordinate (in cm). Image Source: [34]

2.3.4 Drift Chambers

The Drift Chambers tracks the charged particle produced after the interaction and deviation by the magnetic field. The Drift Chambers has three regions. Region one, is the nearest to the interaction region and the inner-most chamber, it is at a position radially below the torus coils where magnetic field is the weakest. Region two, is mounted with the magnets cryostats where the magnetic field is the highest and the maximum deviation of the particle is measured at this point. The Region three, is positioned outside of the torus coils, and at the farthest distance from the target, and the magnetic field is again weak here. The regions in an x-z plane of the CLAS detector are shown in Fig. 2.10. These three regions give the tracking information of the particle from a point with almost no magnetic field, to a point of highest magnetic field (highest deflection) and again at a point after suffering the highest deflection. All these points help to give the complete trajectory of the particle inside the known magnetic field.

Each Drift Chamber has two superlayers, one with axially oriented wires (relative to the magnetic field direction) and another with wires oriented at a 6° stereo angle (for azimuthal information). Each superlayer has six layers of wire and every layer has 192 wires arranged as hexagonal drift cells. Each such cell has 20 m gold-plated tungsten sense wires in the middle acting as the positive terminal and is surrounded with 140 m gold-plated aluminum alloy field wires acting as the negative terminal. The gas inside the Drift Chamber is a mixture of 90% Argon and 10% CO_2, the mixture of gas has ionization property, high drift velocity and is non-flammable in nature. The single wire's position resolution is 330 μm and the momentum resolution is δp/p $\leq$ 0.5% for 1 GeV/c and the resolution decreases with increasing polar angle, because of the magnetic field strength.

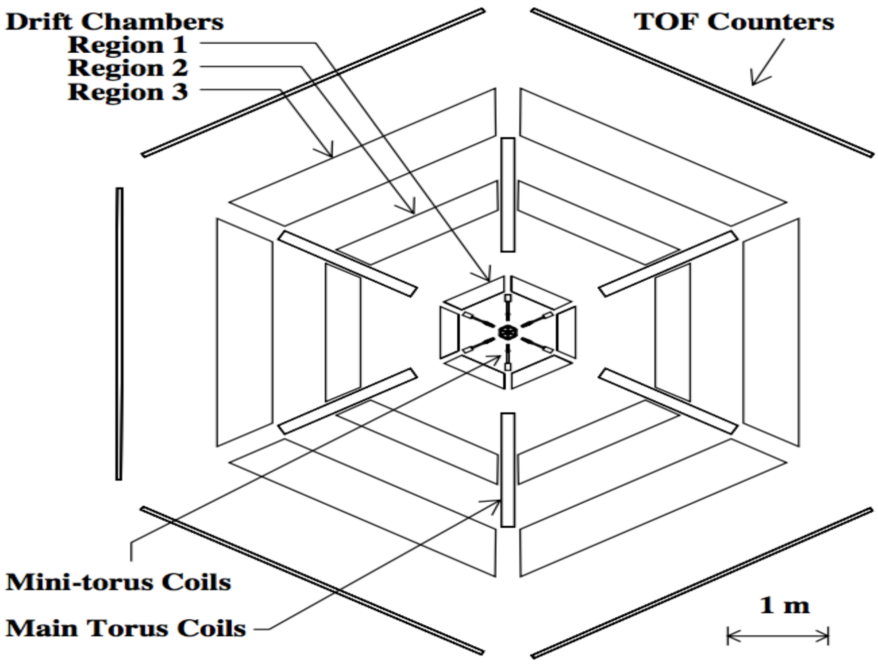

Figure 2.10: The x-z-plane of CLAS showing the relative positions of the three sets of drift chambers can be seen, the first one near the target (Region 1), the second one between the magnet coils (Region 2), and the third one outside the magnets (Region 3). Image Source: [34]

2.3.5 Time of Flight

The Time of Flight (TOF) is the outermost detector of CLAS with six segments, one for each sector. It measures the time instant of the outgoing charged particle from the detector and it is located approximately four meters away from the CLAS center. The TOF acts as a scintillator wall in each sector. It has four panels and a total of 57 bars of TOF-counters which are varying lengths and widths. These counters are arranged in a fashion such that their lengths project perpendicularly onto the beamline. The counters in the most forward region have a scattering angle of less than 45° and the counters vary in length from 32-276 cm and the width is 15 cm. The counters in the region of scattering angle more than 45° vary from 271-445 cm in length and are 22 cm in width. The TOF paddles orientation in a single sector with respect to the beam direction is shown in Fig. 2.11. The signals from the scintillators are collected via photo-multiplier tubes (PMTs) mounted at each end of the bars. The timing resolution is 80-160 ps, depending on the length of the bar where the longer bars has the worse resolution. Using the time information from TOF and ST, and the knowledge of path length allows one to calculate the velocity of a particle. In addition, the momentum of the particle is also known from the Drift Chambers. With this information in hand, one can calculate the mass of the particle, which helps in performing the particle identification. The TOF-system has a very crucial role in this analysis, and it is also a part of the Level 1 trigger [34].

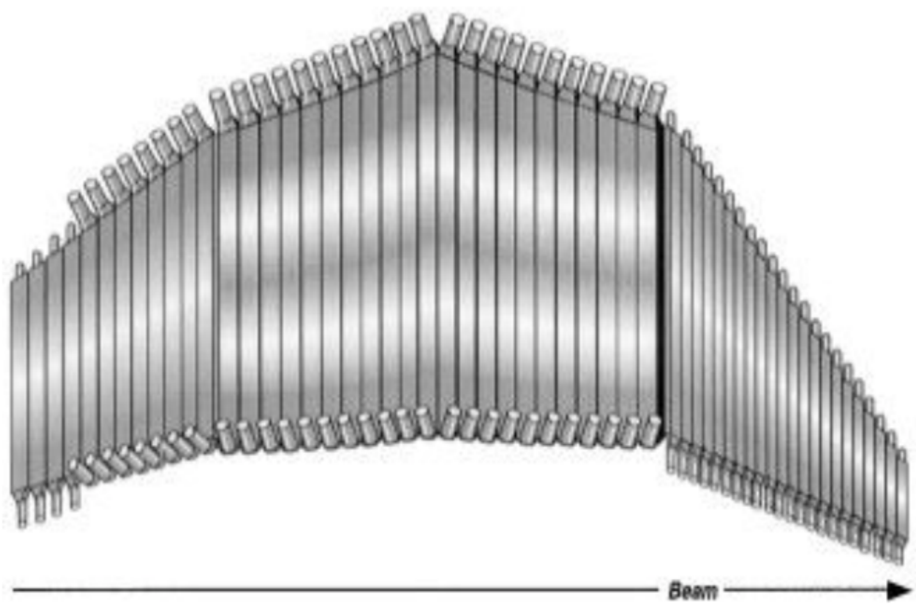

Figure 2.11: A single sector of the CLAS TOF. Image Source: [34]

2.4 Triggers in *g12* and the Data Acquisition in CLAS

During the operation of experiments, a lot of background noise arises from unknown sources like cosmic radiation passing through subdetectors and noise due to electronics. A trigger system sets a criterion to decide on which events should be recorded. The triggering is not only done to remove the background noise described above, but it is also used in a way to optimize and synchronise the real-world limitations in computing power and data storage capacity rates. One of the important components of the *g12* experimental trigger is the Field Programmable Gate Array (FPGA), which allows the use of the trigger with multiple conditions. FPGA allows a total of twelve different trigger conditions together, and also allows modification of the trigger condition during the running of the experiment. The trigger conditions are signals from various subdetectors which have to be present for a certain event to be recorded. The signals from the subdetectors in CLAS sum up to $\approx$ 40,000 readout channels for each trigger. A discriminator monitor attached to each channel defines a threshold, and any signal needs to exceed this defined threshold in order to be recorded. The signal allowed by the discriminator is regarded as events from the physics interaction which are digitized by two types of hardware. The time to digital converter (TDC) records the time at which a signal arrives and the analog to digital converter (ADC) digitizes an analog signal by counting the number corresponding signals. The TDC and ADC can handle multiple signals parallely and write their output to a single data stream. Software processes running on server clusters communicate with each TDC and ADC and assemble their data stream into an event-based data format which is then stored in a disk array. So, the trigger decides the events to be saved, and these signals with information from all the subdetectors are collected and written to the tapes by the Data Acquisition System (DAQ) in CLAS. The DAQ in CLAS during the *g12* run recorded events at a speed of 8 kHz. The raw digitized data from the different electronics are processed by series of CLAS offline reconstruction programs and modules. The processing finally converts the raw digitized data into event based separated in time information, along with the information of individual particles with PID and signals from all different subdetectors produced in the reaction. After this offline reconstruction of events, the data is used for analysis to achieve the physics goals.

2.5 Data Reconstruction and Particle Identification

The process of reconstruction of the raw data and converting it to a format where it is suitable to perform physics analysis is called cooking. The raw data from subdetectors are first calibrated and then processed through program "a1c" program for reconstruction in *g12*. The signal from a subdetector in each sector is analysed separately. The hits in the DC regions form clusters and a hit-based-tracking is performed on the DC to find a trajectory based on the information of all three regions. The hit-based tracking is only a preliminary process and a lot of tracks are not identifiable to physical events, as many hits comes from unknown sources referred as noise. So, a time-based tracking is applied to the hits based information to match the corresponding TOF paddles. TOF which gives timing information are read out by TDC is used to set an upper limit to the time of the drift-chamber hits. The DC hits are checked individually with the upper limit, and each hit is verified in increasing time order as the track moves away from the target. This time-based tracking results in elimination of noise hits, clusters and tracks not associated to a physical event. After these eliminations, the remaining clusters of tracks are refitted number of times for precise momentum measurement and event vertex measurement, which is determined by the distance of closest approach of the track to the beamline. The time-based tracking algorithm has sets of tracking parameters obtained from best fits, correlating hits from same events and coincidence from the ST are then extrapolated to other subdetectors. The final stage of reconstruction is the identification of these hits as particles after knowing their mass and charge. The mass can be calculated using the timing and momentum information given below:

$$m = cp^2/\beta^2 \ and \ \beta = \frac{t_{TOF} - t_{vertex}}{cl} \tag{2.1}$$

where c is the speed of light, p is the momentum, l is the length traversed by the particle, t_{TOF} and t_{vertex} are TOF and propagated ST time respectively. The calculated mass and charge gives the particles identification (PID) to the tracks. The classification is given below:

$$PID = \begin{cases} \pi^{\pm}, \ if \ m < 0.3 \ GeV/c^2 \ and \ charge = \pm \\ K^{\pm}, \ if \ 0.35 < m < 0.65 \ GeV/c^2 \ and \ charge = \pm \\ p^{\pm}, \ if \ 0.8 < m < 1.2 \ GeV/c^2 \ and \ charge = \pm \\ d, \ if \ 1.75 < m < 2.2 \ GeV/c^2. \end{cases} \tag{2.2}$$

In cases of mismatch or unavailability of complete information, the reconstructed masses lie between these cuts and, therefore, classified as unknown.

Chapter 3

Event Selection & Simulation

The event selection begins with recorded, presorted and calibrated *g12* data available on the JLab data farms. Events are selected further in a way that there are one or more beam photons ($x_n \gamma_{beam}$), target proton (p_{target}), a single π^+, π^- and recoiled proton (p). These events are then processed using series of modules developed by CLAS collaboration along with various conditions and selections which taps the γ p $\rightarrow \eta'(\rightarrow \eta\ \pi^+\ \pi^-)$ p decay events. Similar final state backgrounds originating in the η' meson region are also referred here as reconstructed events.

The Monte-Carlo event generation and the recipe involved using the specific CLAS modules, conditions and selections to obtain the accepted Monte-Carlo events are also explained. By and large, the chapter will cover the event reconstruction process of the *g12* data and simulation. A flow diagram showing the steps involved is also shown below in Fig. 3.1.

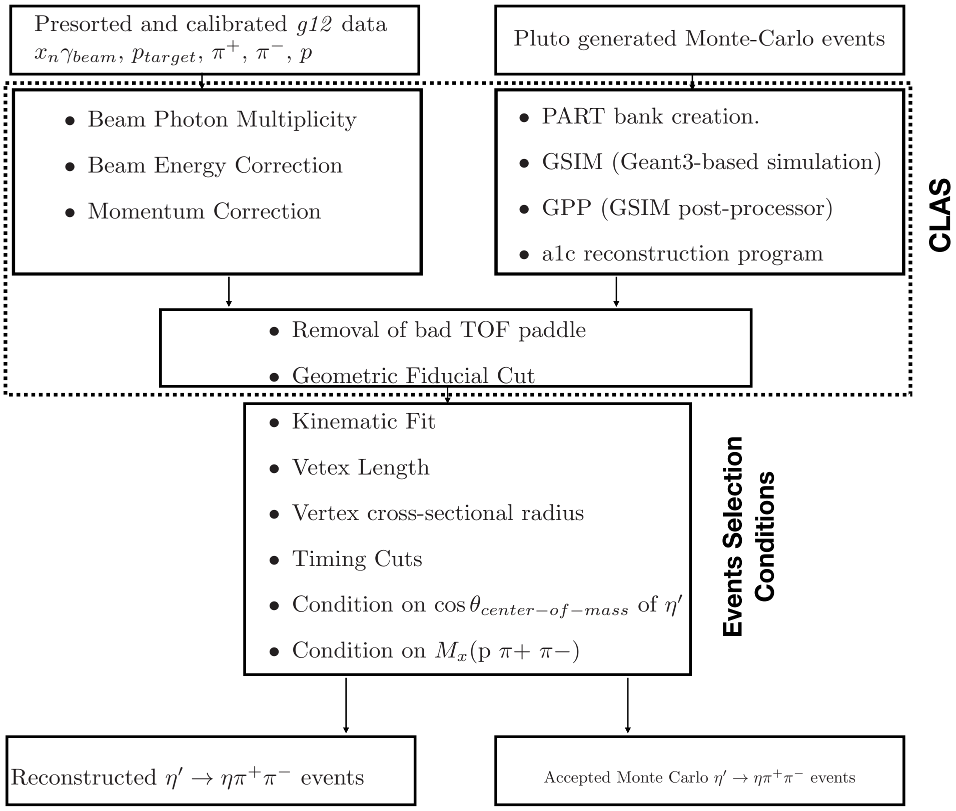

Figure 3.1: Pictorial diagram of the procedure involved to select $\eta' \to \eta\ \pi^+\ \pi^-$ events in data and simulation.

3.1 *g12* Run

The *g12* experiment collected the data during March - June 2008 and recorded 26 x 10^9 events with the production trigger. It recorded 626 production runs, 37 single-prong runs, and 3 special calibration runs. The table of all runs are available in "G12_procedures_working_version.pdf" [38, 39] along with the detailed trigger information. Finally, a total of 660 runs are used in the analysis and the particular run numbers used are provided in Appendix A. Runs which are taken for special calibrations such as normalized, zero-field, empty-target and for different subsystems are not used in this analysis. The fixed target *g12* experiment has an energy of the photon beam ranging from 1.142 GeV to 5.425 GeV. This analysis is performed using all the events from 1.455 up to 3.6 GeV because the beam threshold energy for the production of η' meson is 1.455 GeV and the production cross-section of the η' meson drops significantly after 3.6 GeV. Calibrated data in ".root" [40] format with all events arranged as per the run number, event number, and PID along with all other information recorded by the experiment are used for the analysis. The complete reaction under study is " γ p $\rightarrow \eta'(\rightarrow \eta\ \pi^+\ \pi^-)$ p", and events with one proton, one π^+, one π^- and any number of neutral particles are selected as skim condition out of all events available in *g12* dataset. In this analysis η and η' mesons, are reconstructed as a missing particle. The η' meson is reconstructed with the information of incident photon, target proton, and final state proton and it is represented as M_x(p). Similarly, η reconstruction uses incident photon, target proton, and final state particles proton, π^+, and π^- which is denoted as M_x(pπ+π-).

3.2 Simulation

The Pluto simulation framework [v5.42] developed by the HADES collaboration [41] was used to generate hadronic physics reaction for this analysis [42]. Pluto is a very suitable Monte-Carlo event generator for the low energy regime to study the hadronic decays. The 5 x 10^8 γ p $\rightarrow \eta'$ p $\rightarrow \eta\ \pi^+\ \pi^-$ p events are generated using Pluto along with a model which is close to the real scenario. The incident photon beam distribution is given a bremsstrahlung nature and to make the simulation even more realistic, the measured differential cross-section of the η' meson [43] is fed as input during event generation [44]. The initial events generated by the process is called the generated Monte Carlo events. These events are then processed by the CLAS algorithms, which produces the same effect as the actual detector environment. The processed events by the algorithm are called the accepted Monte-Carlo events. The generated Monte-Carlo events with the above mentioned model are first extracted in the standard CLAS format called the "gamp" files and are then processed with CLAS simulation suit in the following order:

- The gamp files are first converted into the special CLAS format called the PART bank containing the event. The sole reason behind storing the events in a PART bank is that the CLAS programs require it.

- GSIM (Geant3-based simulation): GSIM in CLAS simulates the decay tracks of particles and finally the digitized information is sorted in other "raw" banks from the PART bank.

- GPP (GSIM post-processor): The events are passed through GPP, which smears detector signal more accurately to reflect the actual resolution and to simulate the experimental conditions.

- a1c program: Finally the events passed through a1c, which is a reconstruction program for the simulated data. The same program is used during data reconstruction.

A complete description of these reconstruction steps can be found in the reference [38].

3.3 *g12* Corrections

In order to perform precise measurement of variables which will be later used in the analysis, one has to remove any inefficiency involved in the experiment to a maximum possible extent. In the *g12* experiment these inefficiencies were thoroughly studied and taken care by the set of *g12* corrections. The *g12* corrections were derived from the exclusive π^+, π^- and proton reaction (γ p $\rightarrow \pi^+ \pi^-$ p). A description of corrections to the analysis is given below, however, for a detailed description follow the reference cited in [38].

- Beam Photon Multiplicity: The CEBAF at Jefferson lab accelerates electrons in bunches which are separated by a time interval of 2.004 ns. When an electron bunch reaches hall B, the RF timing is recorded. The electrons then interact with the radiator material gold (Au) and are deviated towards the tagger counters [33] due to the magnetic field strength, where the time instant of the electron hitting the counter is recorded. The interactions between electron and radiator produce bremsstrahlung photons which travel towards the target and hit the start counter, which records the start time. A matching of the start time, RF time and tagger time instant enable to tag in-time photons. Due to multiple electrons producing many photons, the matching is satisfied more than one time in an event, giving more than one in-time photon. Finally, all the photons which fall within a timing window are recorded. The timing window corresponds to a difference between the time instant recorded by the tagger and start counter. This timing window difference is 1.002 ns. The relative numbers of the event with different beam photon multiplicities within the timing window are shown in Fig. 3.2. There are approximately 12 % events in the dataset which has more than one in-time photons after the skim selection. These multiple photons in a single event are considered to be individual events with different combinations of the same final state particles in the analysis.

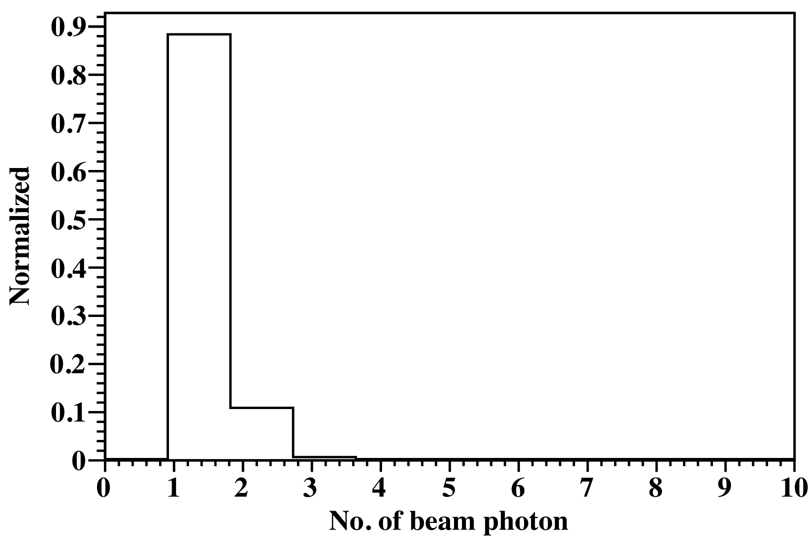

Figure 3.2: Normalized plot showing relative number of event versus number of beam photons within the 2.004 ns timing window.

- Energy Loss Correction: A charged particle produced inside a target material suffers from energy loss due to ionization in the medium, while passing through the matter on its way. The energy loss is proportional to the distance traversed by the particle and the density of the medium, and can be explained by the Bethe-Bloch equation [45]. These corrections were included in the "eloss" package written by Eugene Pasyuk, Research Professor at Arizona State University, and included in the "CLAS software package". These corrections take care of materials like liquid hydrogen, Kapton walls of the target, beam pipe, Start Counter, the air between Start Counter and first set of drift chambers in the path of the particle. This loss is very small for light particles like electrons or positrons which travel with a velocity close to "c" compared to heavy particles like protons. So these corrections were not applied to light particles [46].

- Beam Energy Correction: There are two corrections to the incident beam photon energy, one is due to the mechanical sagging of the tagger planes, which gives miscalculated energy information of the electron's energy. In addition to that, the other is the beam photon energy which is miscalculated due to tagger magnet shut-off during the *g12* run period. It was identified when the missing masses computed for *g12* were systematically low depending on the run number and varied by as much as 10 MeV. The reason behind this problem was the tagger magnet shut-off around the run 56920 on May 12, 2008. The restarting of the tagger magnet changed the field strength of the magnetic field due to the residual magnetic field (hysteresis), although the tagger current was the same. This magnetic field resulted in *g12* missing mass fluctuations, as the scattered electrons were directly affected by the field and consequently gave wrong tagged photon energy. So, there is a correction to the incident beam photon energy of the affected runs. This correction is only applicable to the data and not applicable to the simulated events.

- Momentum Correction: This correction arises due to the difference in the magnetic field of the magnetic field map in the reconstruction software and the actual magnetic field of the CLAS torus. The correction depends on the particle type and it varies for different CLAS sectors. It is finally a correction to the momentum of the charged particles and can be calculated from the azimuthal angle ϕ of the particle. This correction is only applicable to the data.

- Removal of bad TOF Paddle: The routine removes those paddles which show a significant drift on the position resolution of any particle using the θ versus the ϕ map of the detector. This correction takes the sector number and paddle number as input and is applicable to both, data and simulation.

- Geometric Fiducial Cut: The Geometric Fiducial Cut reject events lying in regions outside the well behaved acceptance and where simulations cannot be reproduced reliably. These regions are defined by an upper and lower limit to the azimuthal angle ϕ between the center of a sector and a particle track. This cut removes the dead part of the detector from the $\theta - \phi$ map as shown in Fig. 3.3. It is applied with the "nominal" option out of the three options - "tight, loose and nominal" present in the routine. This correction is applied to both data and simulation [47].

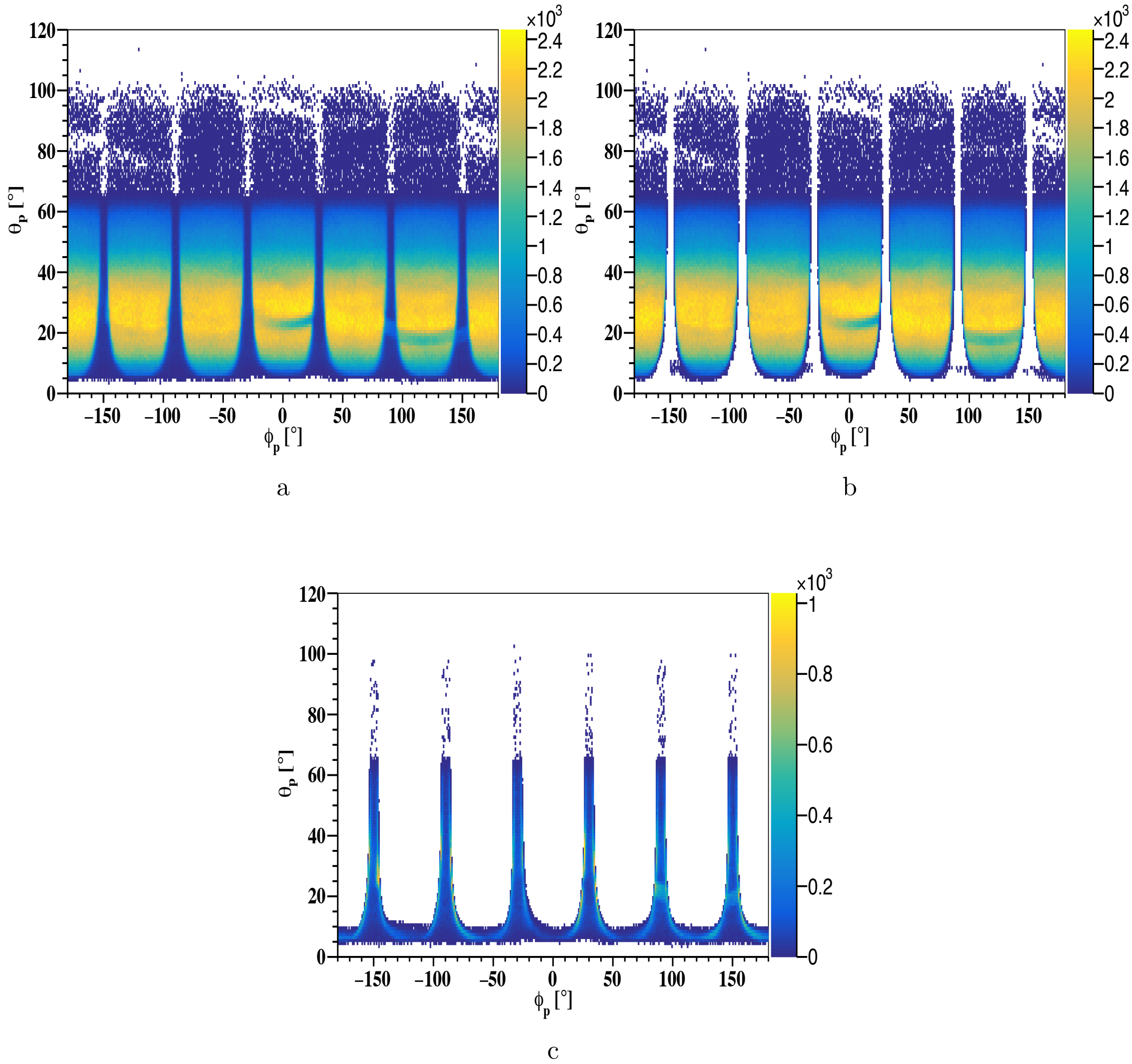

Figure 3.3: (a) The polar angle of proton (θ_p) versus azimuthal angle of proton (ϕ_p) before the fiducial volume cut applied, (b) after the fiducial volume cut and (c) the events which got eliminated by the cut.

3.4 Event Selection

This upcoming part of the chapter contains the analysis conditions and corrections, based on the experiment geometry and decay reaction specifics to improve the identification of the particles, thereby, enhancing the signal to background ratio. These corrections are applicable sometimes only to *g12* data and often to both the data and simulation. The applicability of these corrections to *g12* data and simulations are listed in Table 3.2 appearing at the end of the chapter for a quick summary.

3.4.1 Kinematic Fitting

Kinematic Fitter [48] is a tool used to get rid of unwanted background in the signal channel and helps to improve the signal to background ratio. Any measurement with a tool comes with an error, and it can be represented as a vector $\vec{\eta}$. We can also define the measurement as,

$$\vec{\eta} = \vec{y} + \vec{\epsilon}. \tag{3.1}$$

where $\vec{y}$ denotes the actual value of the measurement without error and $\vec{\epsilon}$ is the error associated with the measurement. These measured variables for an event have correlations among them and it can be expressed with constraining equations. These constraints can also be shown as a function of some unmeasured variables. The fitter uses the magnitude and error of the measured variables along with the correlations among variable to obtain the precise χ^2 minimization and the probability of each event. The constraints are calculated using the method of Lagrange multipliers through a least-square fit. In a reaction with "k" constraints and "n" unmeasured variable, the effective number of constraints are (k - n). Such a χ^2 minimization with (k - n) effective constraints are called a (k - n)-C fit.

The CLAS *g12* Kinematic Fitter is tuned for the reaction γ p $\rightarrow$ π^+ π^- p, which has four constraints from energy-momentum conservation, three from momentum and one from energy make it a 4-C fit. In a 4-C fit, all the final state particles are detected and these fit filters unwanted background which is used to adjust the measured tracks to coincide with the constraint. The Kinematic Fitter takes the "TBER (Track Based Error)" matrix, vertex information and four-momentum of all particles as input. The vertex information is obtained from the transformation of measured tracking parameters which are momentum (p), the dipolar angle (λ) and azimuthal angle (ϕ) of the particle relative to the sectors plane, and these make the TBER matrix [49]. The Kinematic Fitter with these inputs return probabilities and χ^2 along with the pull-distribution value of momentum p, λ and ϕ for each particle of every event and the incident photon energy (E_γ) of every event. The pull-distributions are the difference between the measured and the final parameters obtained from the kinematic fit and it is nor-

Pull (Data)	μ	σ	Pull (Simulation)	μ	σ
Proton p	0.106	1.162	Proton p	0.091	1.105
Proton λ	0.012	0.947	Proton λ	0.012	1.125
Proton ϕ	-0.031	0.999	Proton ϕ	-0.027	1.031
π^+ p	0.074	1.102	π^+ p	0.059	1.061
π^+ λ	0.039	0.974	π^+ λ	0.027	1.104
π^- ϕ	-0.059	1.029	π^+ ϕ	-0.058	1.030
π^- p	0.168	1.111	π^- p	0.157	1.076
π^- λ	0.031	0.993	π^- λ	0.025	1.125
π^- ϕ	-0.033	1.030	π^- ϕ	-0.022	1.028
γ E	-0.164	1.117	γ E	-0.157	1.053

Table 3.1: The table shows the Gaussian mean (μ) and width (σ) for the pull-distributions from a 4-C kinematic fit of γ p $\rightarrow$ π^+ π^- p to events from data and simulation after a 1% probability cut.

malized by the quadratic error difference. The pull-distribution of a particle's momentum p, λ, and ϕ and E_γ from all the events are fitted with Gaussian, and the fit parameters (mean and sigma (σ)) decide the quality of the covariance matrix. In an ideal case, the Gaussian fitted to the pull-distribution is expected to return zero mean and σ of one, which ensures that the fitter correctly calculates covariance error matrix. The probability and fitted value of the pulls from data and simulation for the reaction in equation 3.2 are shown in Fig. 3.4 & 3.5. The mean and σ from the Gaussian fit to the data and simulation after a 1% probability cut is given in Table 3.1.

$$\gamma p \rightarrow \pi^+\pi^- p. \tag{3.2}$$

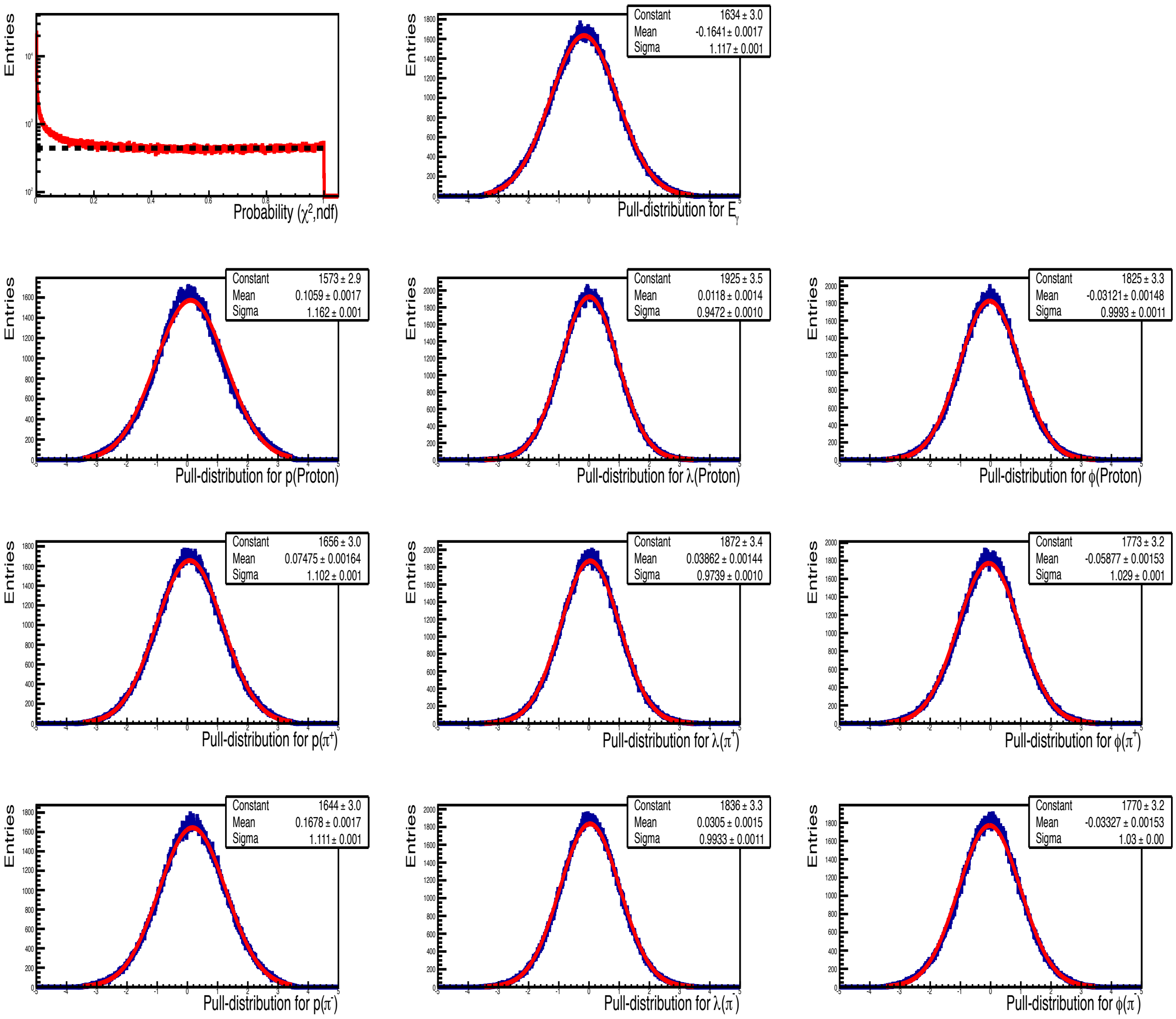

Figure 3.4: The probability and pull-distributions for all the variables (momentum (p), dipolar angle (λ) and azimuthal angle (ϕ)) of all the particles for a 4-C kinematic fit to γ p $\rightarrow \pi^+ \pi^-$ p from *g12* data after a 1% probability cut.

Kinematic Fit to the Analysis

Kinematic fitting is implemented to the analysis channel in equation 3.3, where the missing particle is constrained to be an η meson. The only constraint here is η mass and hence it requires a 1-C fit which is particularly useful when some particle cannot be detected. The *g12* Kinematic Fitter requires "tuned parameters" for the π^+, π^- and p which matches the data in all kinematic ranges of CLAS. Also, the fitter uses some additional scaling to the simulations to match the resolution of the final state particles with the data. All these "tuned parameters" and scaling inputs are obtained from the decay channel in equation 3.2.

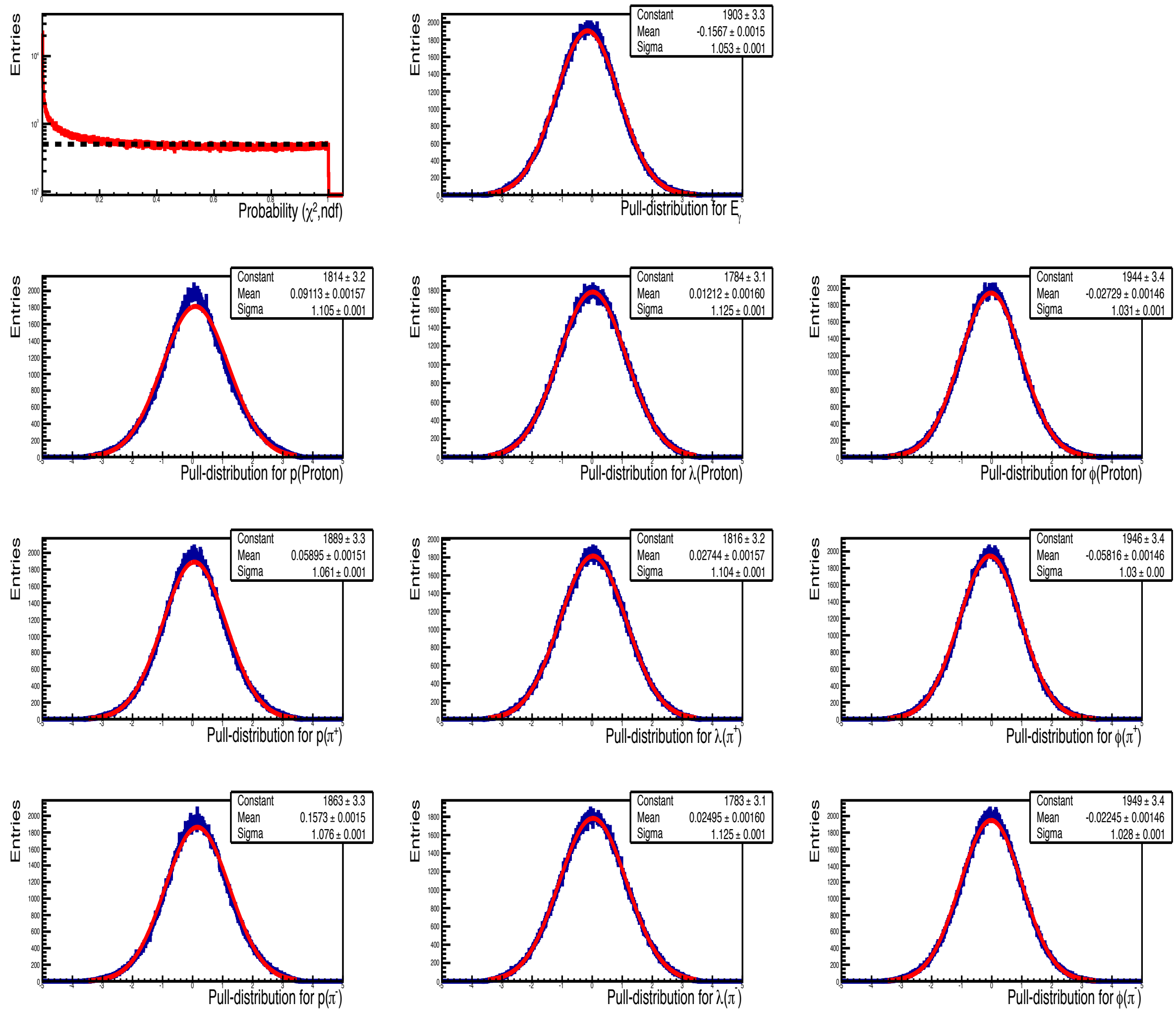

Figure 3.5: The probability and pull-distributions for all the variables (momentum (p), dipolar angle (λ) and azimuthal angle (ϕ)) of all the particles for a 4-C kinematic fit to γ p $\rightarrow \pi^+$ π^- p from *g12* simulation after a 1% probability cut.

$$\gamma p \rightarrow (\eta)_{Missing}\pi^+\pi^- p.(1C) \tag{3.3}$$

As the Kinematic Fitter is tuned for a 4-C fit with the same set of final state particles, so the fitter can be directly implemented to the 1C reaction hypothesis in Eqn. 3.3. The η meson mass constrained 1-C pull-distributions from data and simulation after a 1% probability cut is shown in Fig. 3.7 and 3.8 and the mean of the distribution is centered near to zero is observed as expected. The probability for the channel is shown in Fig. 3.6 and the magenta line at 0.01 shows the 1%

probability cut which rejects events spike with very low probabilities. The first look at the data is available in the form of a M_x(p) versus M_x(pπ+π-) plot in Fig. 3.9. It shows that the probability cut rejects events which do not follow the 1-C constraint of being an η meson and finally one observes η peak with improved signal to background ratio in Fig. 3.9.(b).

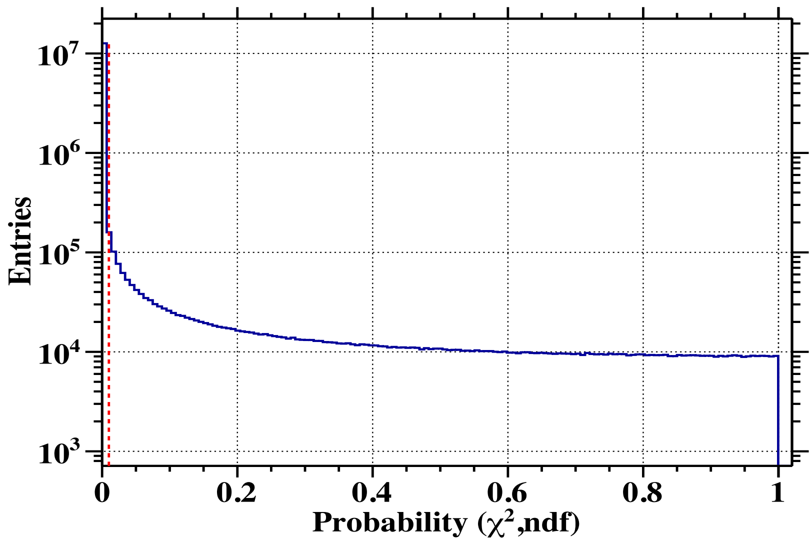

Figure 3.6: The probability for the 1-C kinematic fit to γ p $\rightarrow$ ($\eta_{Missing}$) π^+ π^- p from the *g12* data and the red line represent the position of the cut on the probability.

3.4.2 Vertex Cut

In the *g12* experiment, the target was positioned -90 cm from the CLAS center. The target cell was 40 cm long and 2 cm in radius and has a form of a cylinder filled with unpolarized liquid hydrogen [34]. The vertices of an event in the lab system of the CLAS detector [50] (v_x,v_y, and v_z) are calculated by the backtracking the charged tracks to its origin. The geometrical information of the target is imposed on all events production vertices and it discards all events produced outside the target region. The cuts to confine the events inside the target region is obtained via the condition that $\sqrt{v_x^2+v_y^2} \leq 2$ cm and -110 $\geq v_z \leq$ -70 cm. The Fig. 3.10 shows the v_z (target length) and $\sqrt{v_x^2+v_y^2}$ (cross-sectional radius) from data and simulation along with the position of cuts. Sources of events outside the geometry of the target are due to the interaction of the beam photon with the target walls

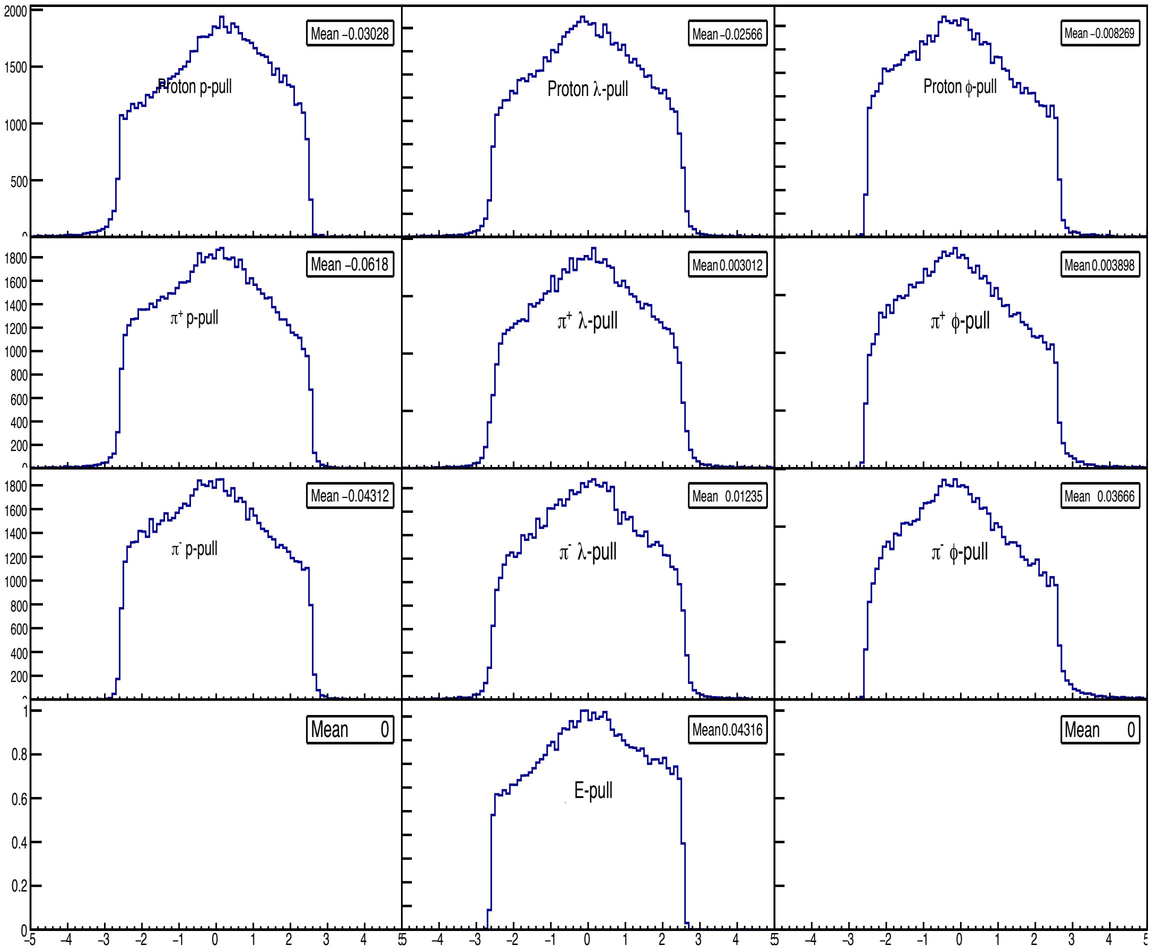

Figure 3.7: The pull-distributions for all the variables (momentum (p), dipolar angle (λ) and azimuthal angle (ϕ)) of all the particles (proton, π^+ and $\pi-$) and E_γ for a 1-C kinematic fit to $M_x(\mathrm{p}\pi^+\pi-)$ being η meson from *g12* data after a 1% probability cut.

and its support structures. One can observe that the number of events varies inside the target geometry, which is because of varying detector acceptance inside the target.

3.4.3 Timing Cuts on proton, π^+ and π^-

Here, the final state particles in an event are rejected if there is a mismatch of timing between TOF sub-detector and Tagger counter. The vertex time (t_{vert}) is the instant of time when the particle left the target [42]. It can be calculated in two different ways, the first way is by using the information from the TOF

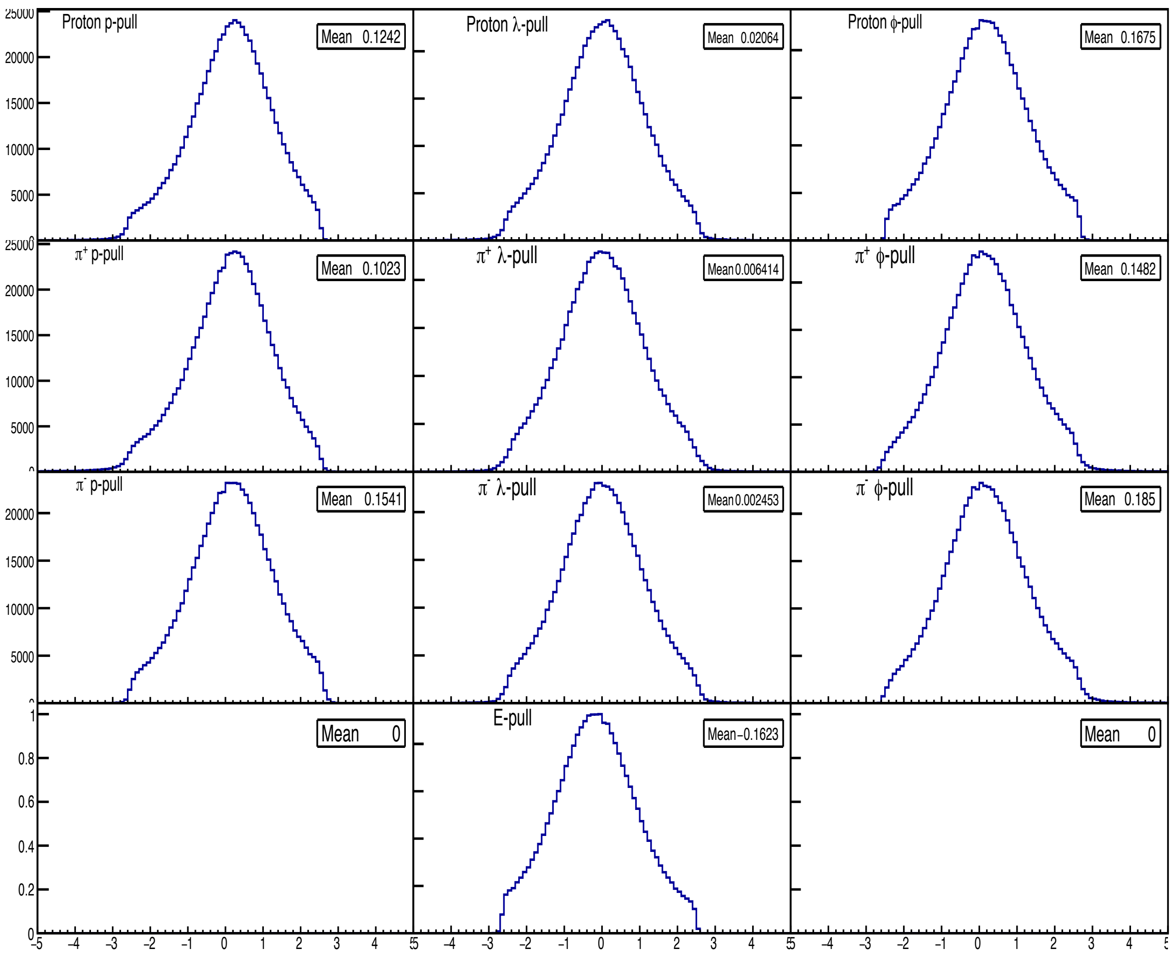

Figure 3.8: The pull-distributions for all the variables (momentum (p), dipolar angle (λ) and azimuthal angle (ϕ)) of all the particles (proton, π^+ and $\pi-$) and E_γ for a 1-C kinematic fit to $M_x(\mathrm{p}\pi^+\pi-)$ being η meson from *g12* simulation after a 1% probability cut.

detectors as,

$$t_{vert}(TOF) = t_{TOF} - \frac{l_{TOF}}{c\beta}$$

where t_{TOF} and l_{TOF} are the measured time and length of the particle in the TOF sub-detector. Here, c is the velocity of light in vacuum and β is the Lorentz factor of the particle calculated by knowing the velocity (v) of the particle as $\beta = \frac{v}{c}$.

The second way to obtain the same vertex timing (t_{vert}) is through the tagger and RF timing information. The timing instant of electrons hitting the radiator can be calculated by propagating the RF-timing of the electron beam bunch. The

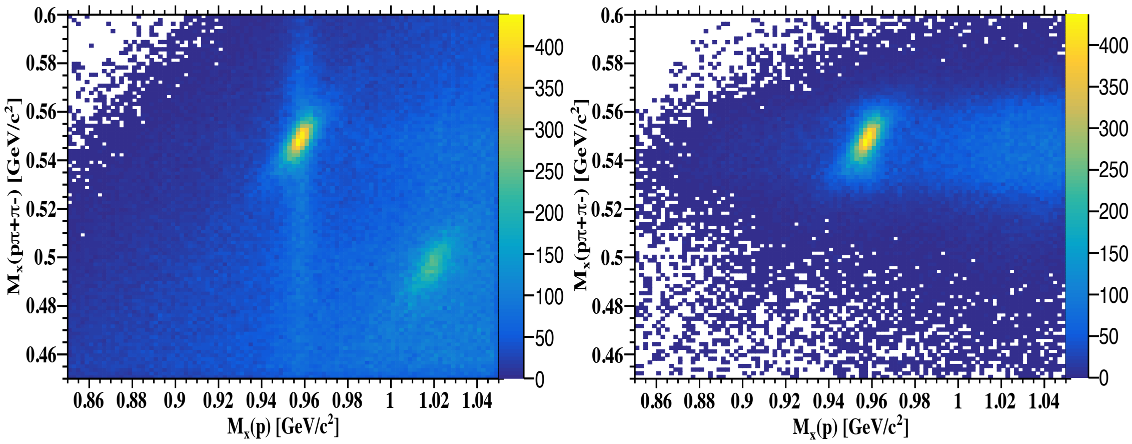

a b

Figure 3.9: M_x(p) versus M_x(pπ+π-) distribution (a) before applying probability cut and, (b) after rejecting events with a probability less than 1%.

time instant of photon crossing the target center (t_{photon}) can be calculated using the tagger information and RF-corrected time instant at the radiation. The t_{photon} combined to the t_{prop}, which is the propagation time from the center of the target to track vertex of the events gives the vertex time using tagger (t_{vert}(Tagger)). It is given by,

$$t_{vert}(Tagger) = t_{photon} + t_{prop}.$$

The difference of the vertex timing $t_{vert}(TOF)$ and $t_{vert}(Tagger)$ is shown in the Fig. 3.11. A cut of $\pm$ 1.0 ns of the timing difference around the mean of 0.0 ns for all the final state particles are placed in both simulation and data to improve particle identification.

3.4.4 Condition on $\cos\theta_{center-of-mass}$ of η' Meson

The generated Monte Carlo events in the simulation are distributed according to the differential cross sections measured by the previous *g11* experiment. However, the previous measurement shows a drop of acceptance in the higher and lower region of $\cos\theta_{center-of-mass}$ of η' distribution [43]. This drop in acceptance of the

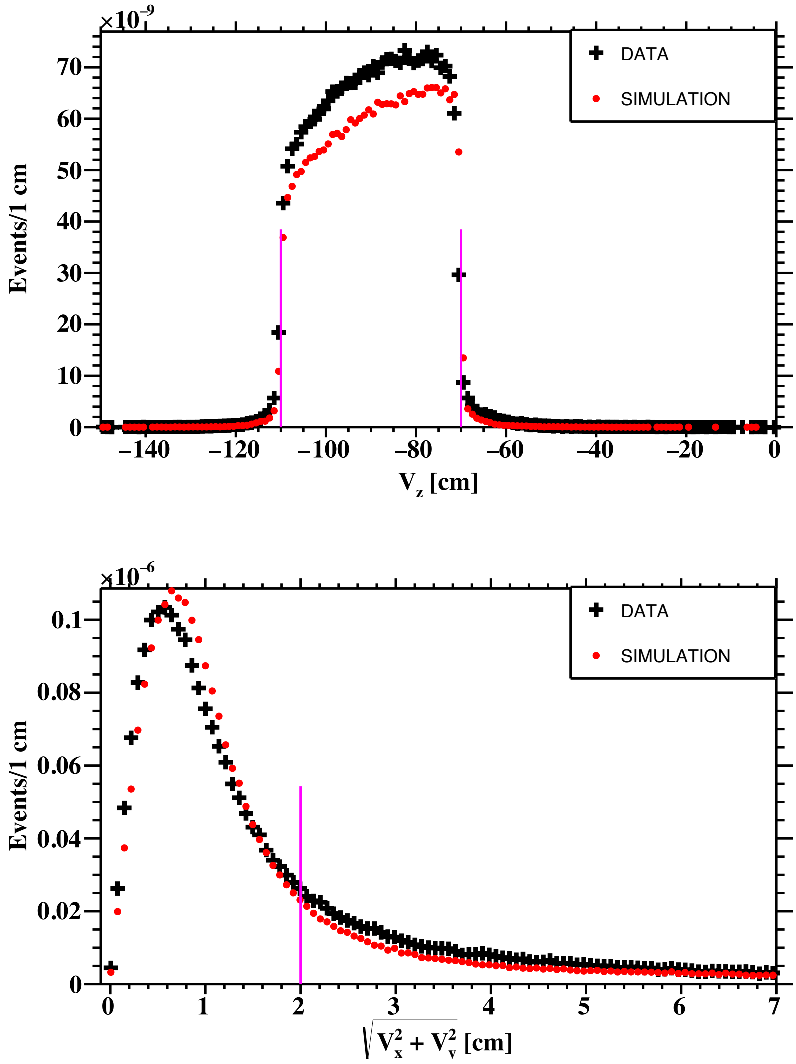

Figure 3.10: The upper plot is v_z position and the lower plot is the cross-sectional radius $\sqrt{v_x^2 + v_y^2}$ of the γ p $\to \eta'$ ($\eta_{Missing}$ π^+ π^-) p events vertex from data (black) and simulation (red) and the lines show the position of the cuts in the analysis.

region is from events that travel to the beam pipe in the forward and backward direction. To take care of events in this region a condition of $|\cos\theta_{center-of-mass}$ of $\eta'| \leq 0.85$ is placed in the analysis unambiguously in both the data and simulation. The elimination of the region from the analysis is made to ensure that there is no additional inconsistency in the data and simulation from this less understood region.

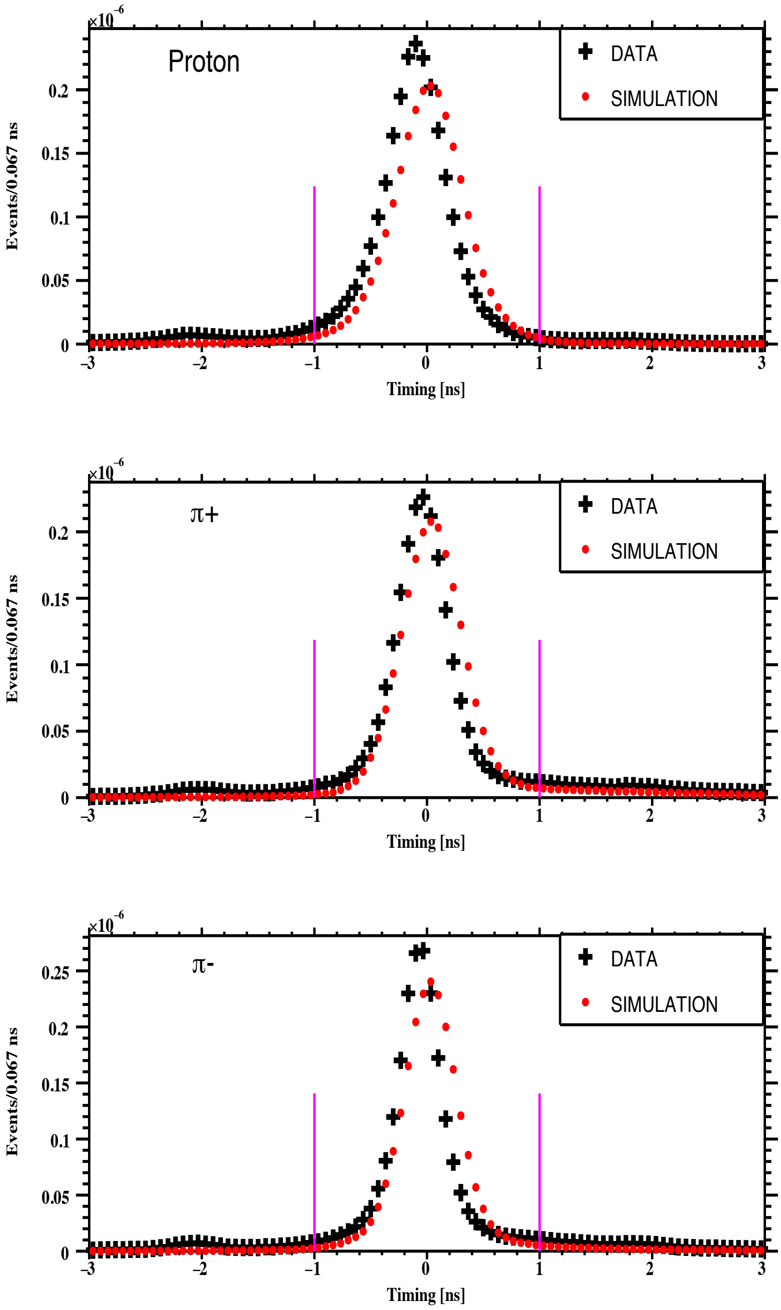

Figure 3.11: $[t_{vert}(TOF)$ - $t_{vert}(Tagger)]$ distribution from the simulation and data for proton(Upper), π^+(Middle) and π^-(Lower), the region between the lines show position of the cut in the analysis.

3.4.5 Condition on the Measured Missing Mass of η Meson

The reconstruction of η meson is achieved using the information of the final state particles by performing a missing mass M_x(pπ+$\pi-$). The distribution of

M_x(pπ+$\pi-$) shows a clear peak of η meson and background as shown in the Fig. 3.12. The η meson events are selected from this distribution using a range on M_x(pπ+$\pi-$) - 0.547 $\leq \pm 2\sigma$ (0.015 GeV). The 2σ condition around the mean of the distribution ensures that the events are symmetrically picked in the range from the distribution and this selection decreases the chances of biasness towards the selection of events. This condition is placed in both data and simulation. The reason behind the 2σ selection is explained by the resolution of the η meson which is calculated after fitting the difference distribution between the true and reconstructed values of $M_x(\text{p}\pi^+\pi^-)$ from the simulation which is shown in the Fig. 3.13.

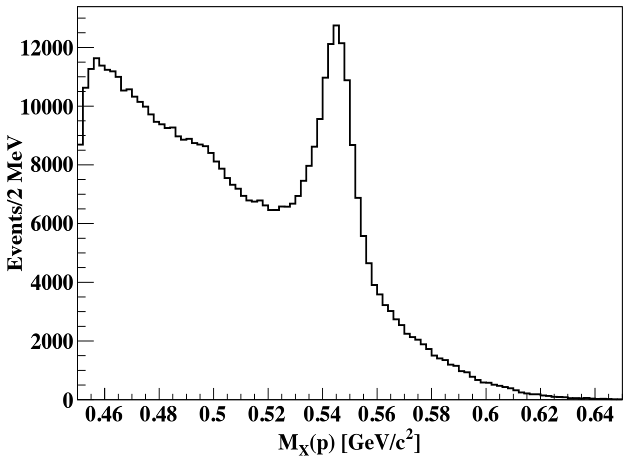

Figure 3.12: The distribution $M_x(\text{p}\pi^+\pi^-)$ from the *g12* data.

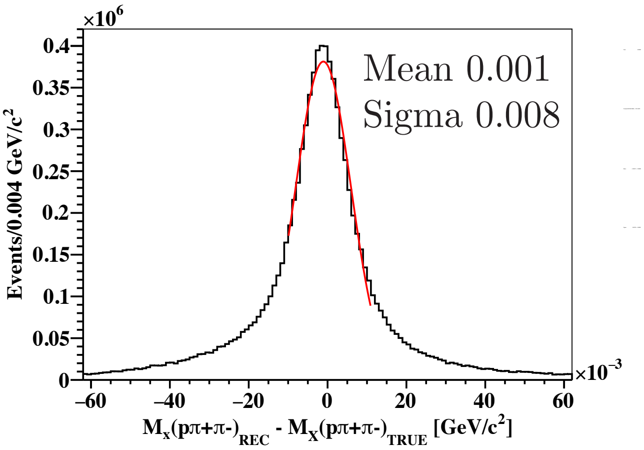

Figure 3.13: Difference between true and reconstructed value of $M_x(\text{p}\pi^+\pi^-)$ from simulation.

Table 3.2: The list of conditions and corrections implemented to the "*g12*" data and simulation:

"*g12*" Experiment data	Simulation
Beam Photon Multiplicity	NA
Beam Energy Correction	NA
Momentum Correction	NA
Removal of bad TOF Paddle	Applicable
Geometric Fiducial Cut	Applicable
Kinematic Fit (1% probability cut)	Applicable
Vertex Length Cut (-110 $\leq v_z \leq$ -70 cm)	Applicable
Vertex cross-sectional radius ($\sqrt{v_x^2 + v_y^2} \leq 2$ cm)	Applicable
Timing Cuts on proton, π^+ and π^- ($\mid t_{vert}(TOF)$ - $t_{vert}(Tagger) \mid \leq 1.0$ ns)	Applicable
$\mid \cos\theta_{center-of-mass}$ of $\eta' \mid \leq 0.85$	Applicable
$\mid M_x$(p $\pi+$ $\pi-$) - 0.547 $\mid \leq 0.015$ GeV	Applicable

Chapter 4

Data Analysis

This chapter explains the detailed steps involved to obtain the Dalitz plot and its parameters for the $\eta' \to \eta\ \pi^+\ \pi^-$ decay. In the analysis, the reconstructed events are first fed to a binned Dalitz plot and then all the bins outside and on the boundary are removed. The low acceptance bins are also removed after that. Furthermore, the background subtraction is performed in the remaining bins of the Dalitz plot. It is performed for two types of background, first the non-resonant background and second the in-peak background. The in-peak background reduction is done using realistic Monte-Carlo (MC) simulations. The cross-check of the simulated model used in the analysis is done by comparing the kinematic variables from the data and the simulation for all the final state particles. Then the η' meson photoproduction cross-section is measured and compared with the previous measurements. In addition, the Dalitz variables distributions are compared in various sub-ranges of kinematic variables. The background subtracted Dalitz plot is then fitted to a general parameterization using two different methods along with acceptance correction to obtain the final Dalitz plot parameters and finally, the best method is selected for further study. All these steps are shown as a flow diagram in the Fig. 4.1.

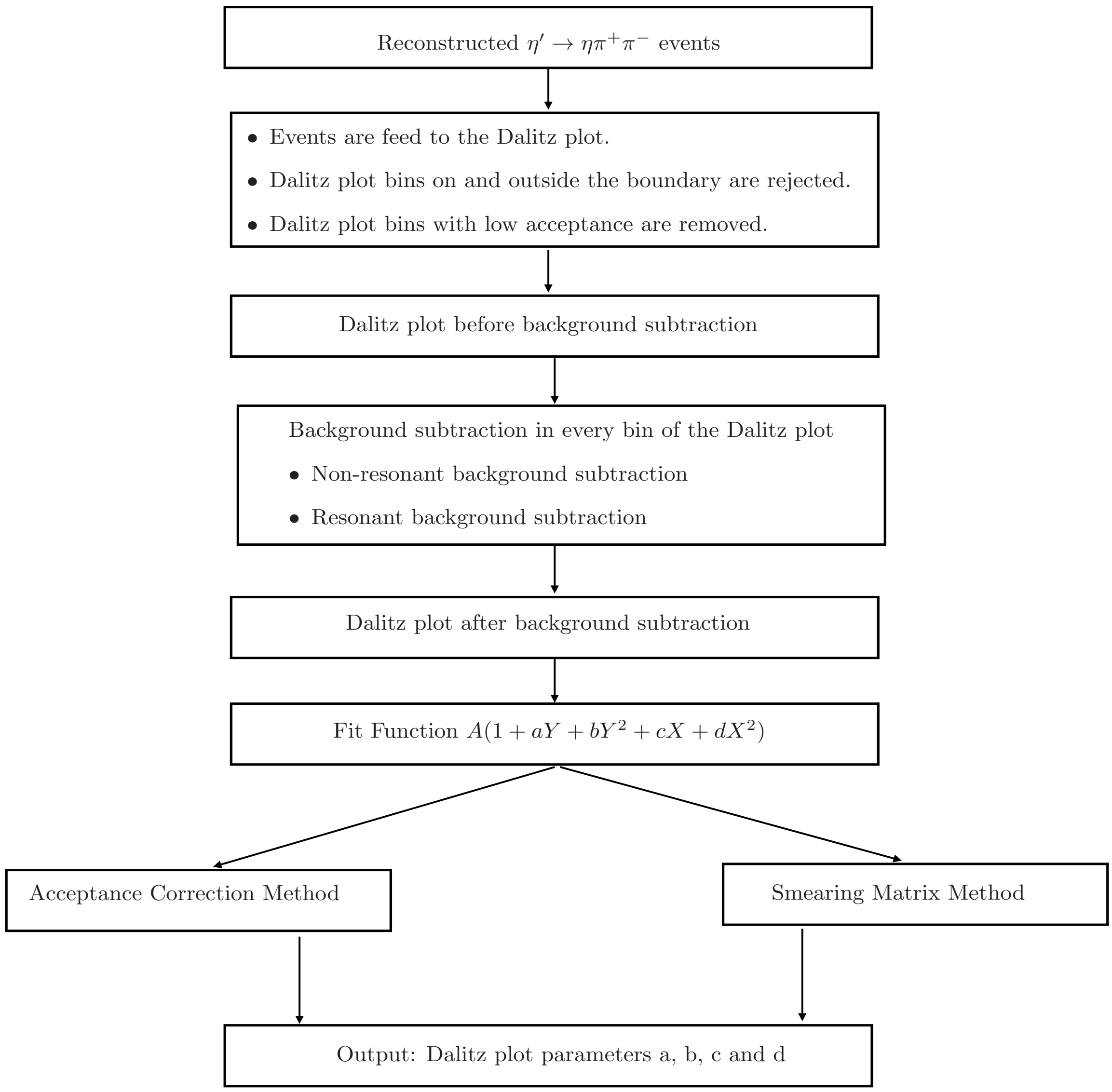

Figure 4.1: Pictorial diagram of the steps involved to obtain the Dalitz plot parameters .

4.1 Selection of Bins in the Dalitz Plot

In this section, the background subtraction method is explained and finally, a Dalitz plot of $\eta' \to \eta\ \pi^+\ \pi^-$ events are achieved with the *g12* data. A quick recap of selections imposed to the *g12* dataset are as follows:

- Selection of the Beam Photon energy range E_γ (= 1.45-3.60 GeV)
- *g12* Corrections
- CLAS *g12* Kinematic Fitter (probability > 0.01)

- Vertex Cut (-110 cm $\leq v_z \leq$ -70 cm & $\sqrt{v_x^2 + v_y^2} \leq$ 2 cm)

- Timing Cut ($\pm$ 1.0 ns)

- $|\cos\theta_{center-of-mass}$ of η' $| \leq 0.85$

- $| M_x$(pπ+$\pi-$) - 0.547 $| \leq$ 0.015 GeV

The M_x(p) distribution after each cut is shown in the Fig. 4.2. The X and Y variables are calculated for events surviving after these cuts, and then a Dalitz plot of 30 bins in X and 30 bins in Y are filled with those events. Equal number of bins in the Dalitz plot are selected as the resolution of the X and Y variables are of the same order (0.03). The Fig. 4.3 shows the qualitative estimate of X and Y resolution. The two dimensional Dalitz plot has 900 bins. To keep a better track of the 2-D Dalitz bins, each bin is assigned a unique single number which is called the "Global Bin". The unique global bin number is assigned using a formula given as:

$$GlobalBin(X, Y) = Floor[\frac{Y + Y_{max}}{\delta}] + N_{bins}.Floor[\frac{X + X_{max}}{\delta}] + 1. \quad (4.1)$$

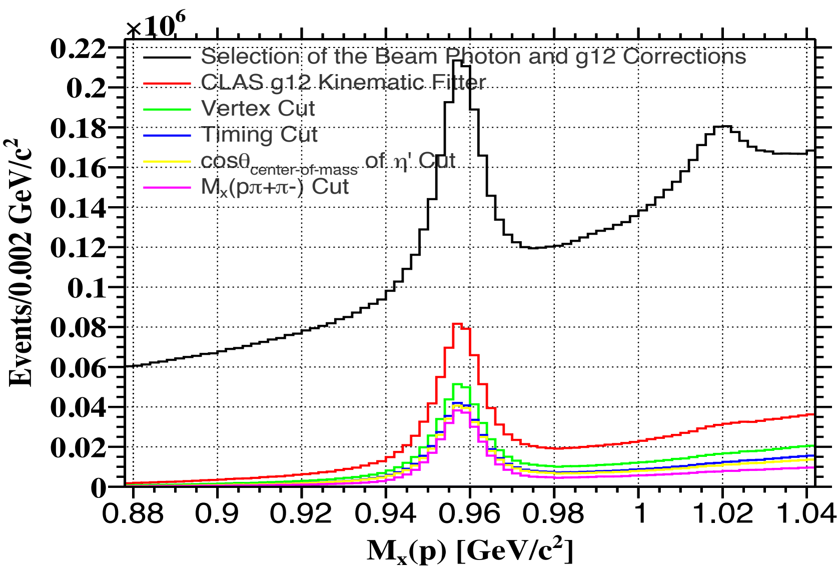

Figure 4.2: The M_x(p) distribution after applying the selections and conditions in order is listed in the plot.

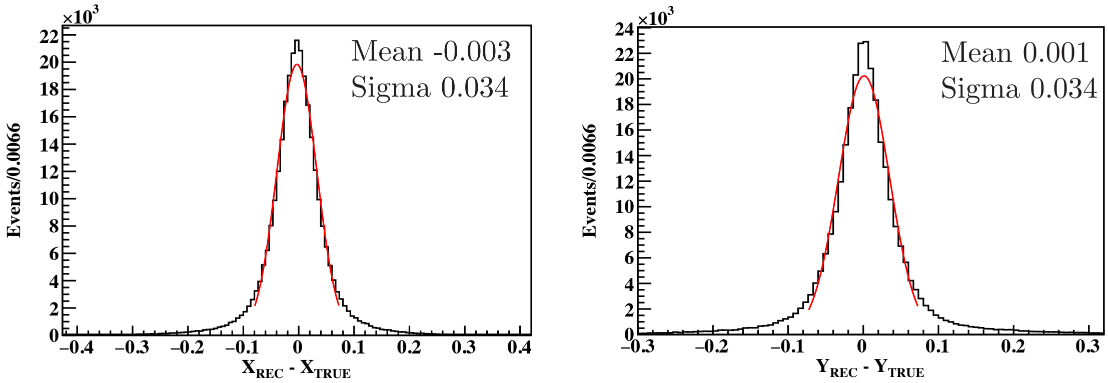

a b

Figure 4.3: The figure (a) shows the difference of reconstructed (X_{REC}) and true (X_{TRUE}) value of the events versus the number of events and the figure (b) shows the difference of reconstructed (Y_{REC}) and true (Y_{TRUE}) value of the events versus the number of events from simulation.

where, X and Y are the central values of a bin, X_{max} (1.5) and Y_{max} (1.5) are the maximum values of X and Y respectively. The N_{bins} are the number of bins (30) chosen along X and Y axis and δ is the bin-width (0.1) of each bin. The Floor is a function that takes as input a real number and gives as output the greatest integer less than or equal to that number. The N_{bins} stands with X in the second term in Eqn. 4.1, so the consecutive global bin number increases vertically along the Y-axis of the Dalitz plot. To give a clear picture on how the two-dimensional Dalitz plot bins translates to a global bin, the Dalitz plot bins are plotted along with global bin numbers in Fig. 4.4.

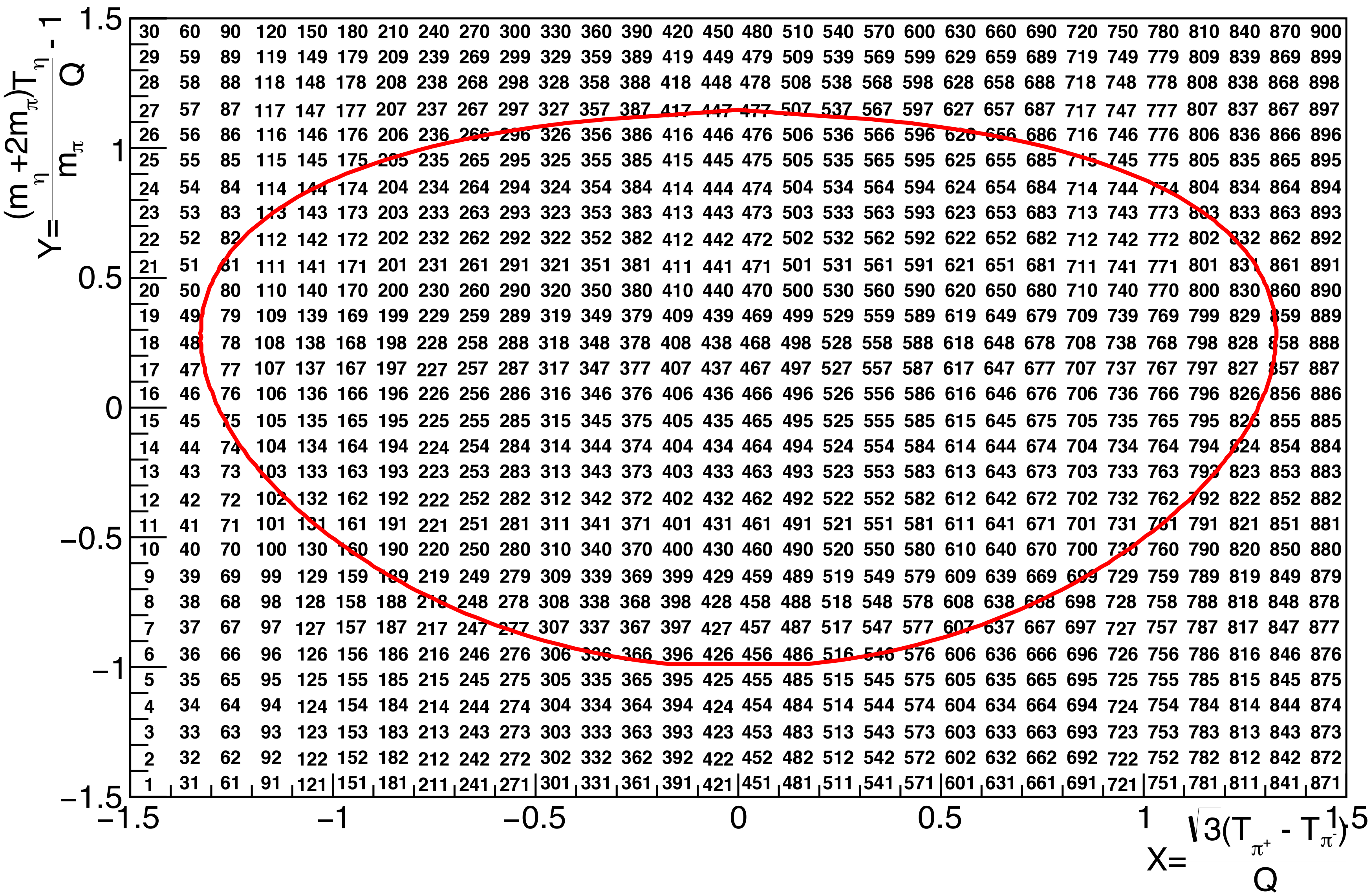

Figure 4.4: Position of the global bins in a two-dimensional Dalitz plot.

The Dalitz plot of $\eta' \to \eta\ \pi^+\ \pi^-$ decay has a phase-space boundary. The boundary of the $\eta' \to \eta\ \pi^+\ \pi^-$ decay can be calculated from the fact that the addition of three momenta of particles $\vec{P}_\eta$, $\vec{P}_{\pi+}$ and $\vec{P}_{\pi-}$ for η, π^+ and π^- respectively is 0 in the rest frame of η' meson.

$$\vec{P}_\eta + \vec{P}_{\pi+} + \vec{P}_{\pi-} = 0 \tag{4.2}$$

Squaring and equating gives:

$$\vec{P}^2_\eta = \vec{P}^2_{\pi+} + \vec{P}^2_{\pi-} + 2\vec{P}_{\pi-}\vec{P}_{\pi-}cos(\theta_{\vec{P}_{\pi+},\vec{P}_{\pi-}}) \tag{4.3}$$

The $cos(\theta_{\vec{P}_{\pi+},\vec{P}_{\pi-}})$ determines the boundary and region of the Dalitz plot, and assumes the maximum value at boundary, when $cos(\theta_{\vec{P}_{\pi+},\vec{P}_{\pi-}}) = 1$.

$$|{P_\eta}^2 - {P_{\pi+}}^2 - {P_{\pi-}}^2| \leq 2\vec{P}_{\pi+}\vec{P}_{\pi-} \tag{4.4}$$

The boundary of the decay $\eta' \to \eta\ \pi^+\ \pi^-$ is given in the equation 4.4. The boundary of the $\eta' \to \eta\ \pi^+\ \pi^-$ decay is calculated in this analysis from the MC generator, which is consistent with equation 4.4. The calculated boundary from MC is finally a function of Dalitz variables X and Y unlike in equation 4.4. Those bins which lie completely inside the Dalitz plot boundary and the events inside those bins are considered for the further analysis.

The acceptance of all the Dalitz plot bins are also calculated. The procedure of the calculation of the acceptance is discussed in Section 4.6. In order to reject bins with a very low probability of detection, an acceptance cut is implemented to the Dalitz plot bins, which rejects all events inside those bins with an acceptance smaller than 0.5%. The acceptance of the Dalitz plot bins is shown in the Fig. 4.5. It is observed that the acceptance drops down at higher X and eliminated by the acceptance cut. It is due to the fact that π^+ curls outward and π^- curls inward inside the magnetic field in the CLAS detector [34]. The opposite direction of curling is because of the opposite charge carried by the particle inside the magnetic field. A particle which curls inward has a higher possibility of detection since it has to traverse a larger distance inside the detector compared to a particle curling outwards. Hence, π^+ meson is expected to have less acceptance when compared to a π^- meson. On top of it, π^+ meson with higher kinetic energy curls more outward which makes it more difficult to detect. The explained process can be seen in the Dalitz plot as well. The higher X region which corresponds to a high kinetic energy region of the π^+ meson thus suffers from poor acceptance.

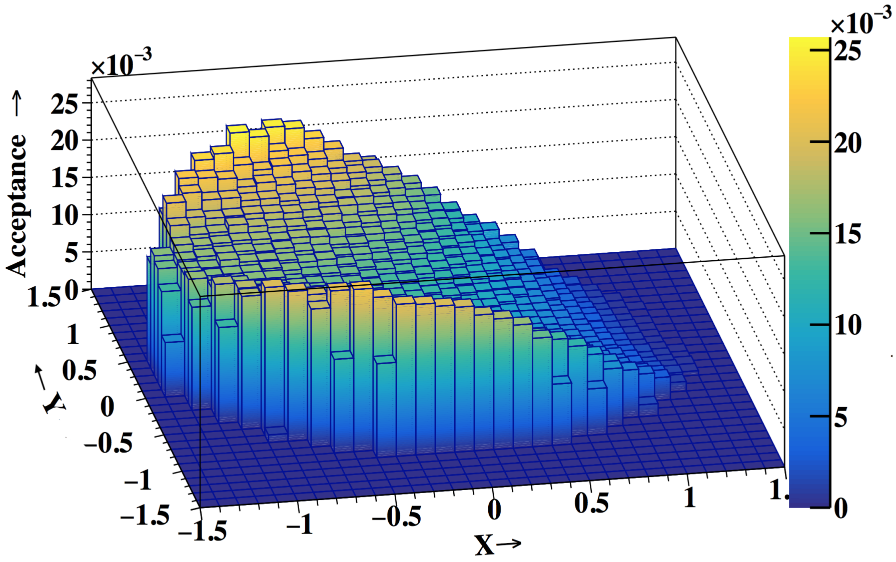

Figure 4.5: Acceptance in each bin of the Dalitz plot.

The boundary of the $\eta' \to \eta\ \pi^+\ \pi^-$ phase space removes 504 bins out of the 900 bins in a 30×30 Dalitz plot. The removal of Dalitz plot bins with less than 0.5% acceptance rejects another 59 bins from the Dalitz plot. Finally, 337 bins and events inside those bins take part in the further analysis. The background subtraction are performed to all these 337 bins individually. There are two types of background present in the data which are described below.

4.2 Non-resonant Background Subtraction

To every Dalitz plot bin considered for the analysis, a non-resonant background subtraction is performed to the M_x(p) distribution. The M_x(p) distribution of a bin is fitted with a Voigtian function explaining the signal and the background is fitted with a Polynomial of order three. In our experiment, the η' meson distribution actually is a convolution of a Lorentz function with a Gaussian, which

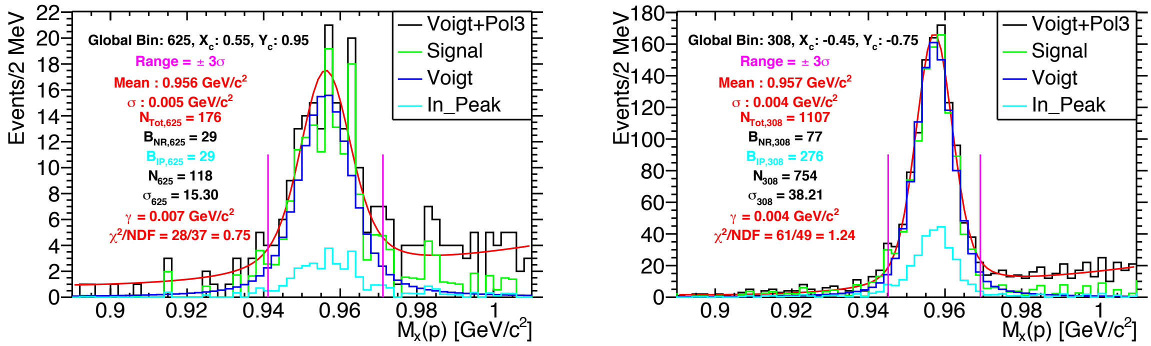

a b

Figure 4.6: The figure (a) is a fit to a low statistics bin and figure (b) is to the highest statistics bin of the M_x(p) distribution in the Dalitz plot. The symbols appearing in the figure are described below:
- X_c and Y_c denotes the central values of Dalitz variable coordinates X and Y for the global bin number i. - $N_{Tot,i}$ denotes the total number of events in the global bin no. i in the 3σ range. - $B_{NR,i}$ denotes the number of non-resonant background events calculated from the smooth non-resonant background subtraction for the global bin number i in the 3σ range. - $B_{IP,i}$ denotes the number of in-peak background events for the global bin number i in the 3σ range. - $N_i = N_{Tot,i}$ - $(B_{NR,i} + B_{IP,i})$ is the number of signal events after background subtraction in the global bin number i in the 3σ range. - $\sigma_i = \sqrt{(N_{Tot,i} + B_{NR,i} + B_{IP,i})}$ is statistical error in the global bin number i.

arise due to the detector resolution of the CLAS detector. So, the η' meson can be described well with a Voigtian function. The fits to two of the bins out of the 337 fitted bins [51] in the Dalitz plot are shown in the Fig. 4.6. Fits to all the 337 bins are given in Appendix C. The χ^2/ndf from the fits to all the bins are shown as a function of global bin numbers in Fig. 4.7.

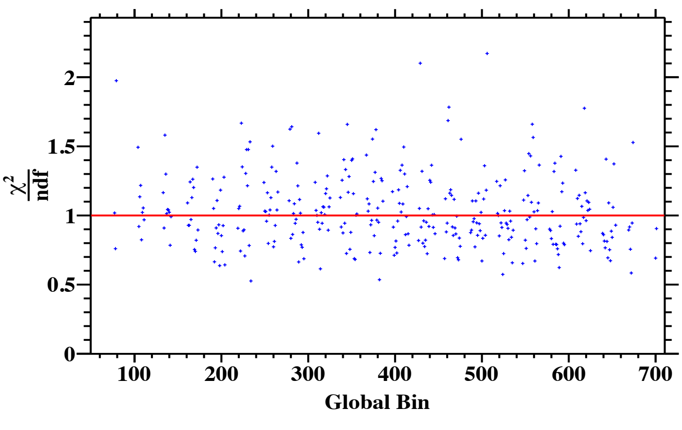

Figure 4.7: Global bin versus the χ^2/ndf of the fits to the individual bin.

4.3 In-peak Background Subtraction

In addition to the non-resonant smooth background, an in-peak background is also present from the channel $\eta' \rightarrow (\eta \rightarrow (\pi^+\pi^-\pi^0 \ \& \ \pi^+\pi^-\gamma))\pi^+\pi^-$ (decay mode 2) and channel $\eta' \rightarrow (\eta \rightarrow (\pi^+\pi^-\pi^0 \ \& \ \pi^+\pi^-\gamma))\pi^0\pi^0$ (decay mode 3) given in the Table 4.1. A calculation of these in-peak background contributions in each Dalitz plot bin is done by generating all the decay modes with production cross-section of the η' meson and a corresponding relative branching ratio [12]. The η' decay is named as primary decay and the η decay as secondary decay. The Fig. 4.8 shows the distribution of the generated signal and in-peak background events in $M_x(p\pi^+\pi^-)$ and $M_x(p)$ mass region, all these modes peaks in the signal region and the contribution to $M_x(p\pi^+\pi^-)$ is asymmetric. The first decay mode in the Table 4.1 is the signal channel for the analysis. In this mode, the secondary decay is given with a combined branching ratio of 72.9 from η into $\gamma\gamma$ (39.41) and $3\pi^0$ (32.68), as the neutral particles are not included in the analysis and set of final state particles are the same for both the secondary decays. Similarly, a secondary decay of η meson for decay mode second and third, the branching ratio is 27.14 for both. The second decay mode has two $\pi^+\pi^-$ and acts as a combinatoric background channel with a different acceptance and is present within the η' meson mass peak. The third decay mode is a pure in-peak background channel and gives the same set of final state particles as the signal channel. The source of this combinatoric background arises from π^+ and π^- decayed through $\eta' \rightarrow (\eta)\pi^+\pi^-$ and $\eta' \rightarrow (\eta)\pi^0\pi^0$, which leaves the π^+ and π^- in both the decays with the similar available energy. Once the contribution of the signal channel in each bin of the Dalitz plot is known, then a scaling is performed to the non-resonant background subtracted spectrum of each Dalitz plot bin [52], and the numbers of events are estimated in each bin of the Dalitz plot. The 2D Dalitz plot before and after the background subtraction are shown in the Fig. 4.9.(a) and (b) respectively. The final Dalitz plot bins with the total number of events used in the further analysis is shown in the Fig. 4.9.(c) and as a function of global bins in the Fig. 4.10.

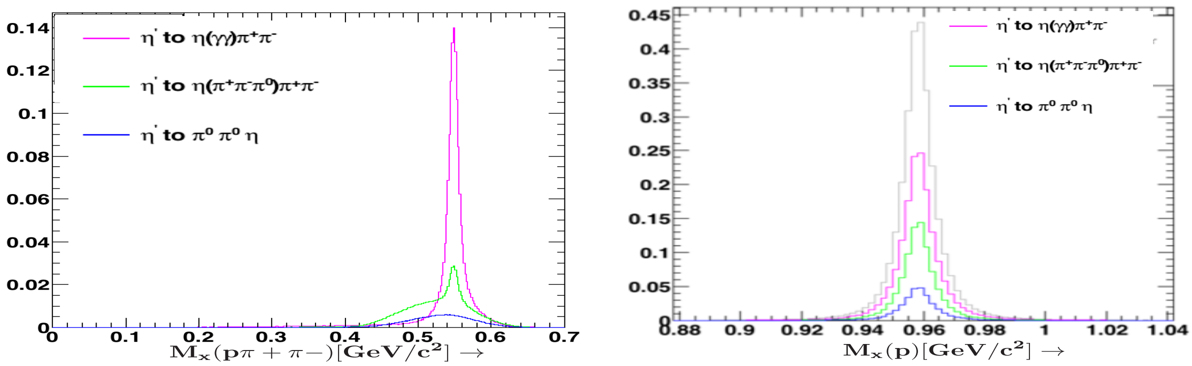

Figure 4.8: The $M_x(p\pi{+}\pi-)$ (left) and $M_x(p)$ (right) for all the three different modes of decay.

Table 4.1: Decay modes along with their relative branching ratio.

Mode	Primary Decay	Br_P (in %)	Secondary Decay	Br_S (in %)	Rel. BR= (Br_PxBr_S)/100 (in %)
1.	$\eta' \rightarrow (\eta)\pi^+\pi^-$	42.9	($\gamma\gamma$ & $3\pi^0$)	72.09	$\frac{(42.9*72.09)}{100} = 30.92$
2.	$\eta' \rightarrow (\eta)\pi^+\pi^-$	42.9	($\pi^+\pi^-\pi^0$ & $\pi^+\pi^-\gamma$)	27.14	$\frac{(42.9*27.14)}{100} = 11.64$
3.	$\eta' \rightarrow (\eta)\pi^0\pi^0$	22.2	($\pi^+\pi^-\pi^0$ & $\pi^+\pi^-\gamma$)	27.14	$\frac{(22.2*27.14)}{100} = 6.02$

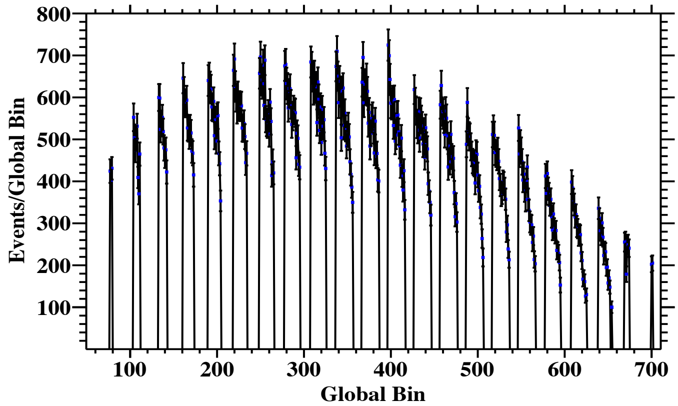

Figure 4.10: Global bin versus background subtracted $\eta' \rightarrow \eta\ \pi^+\ \pi^-$ events.

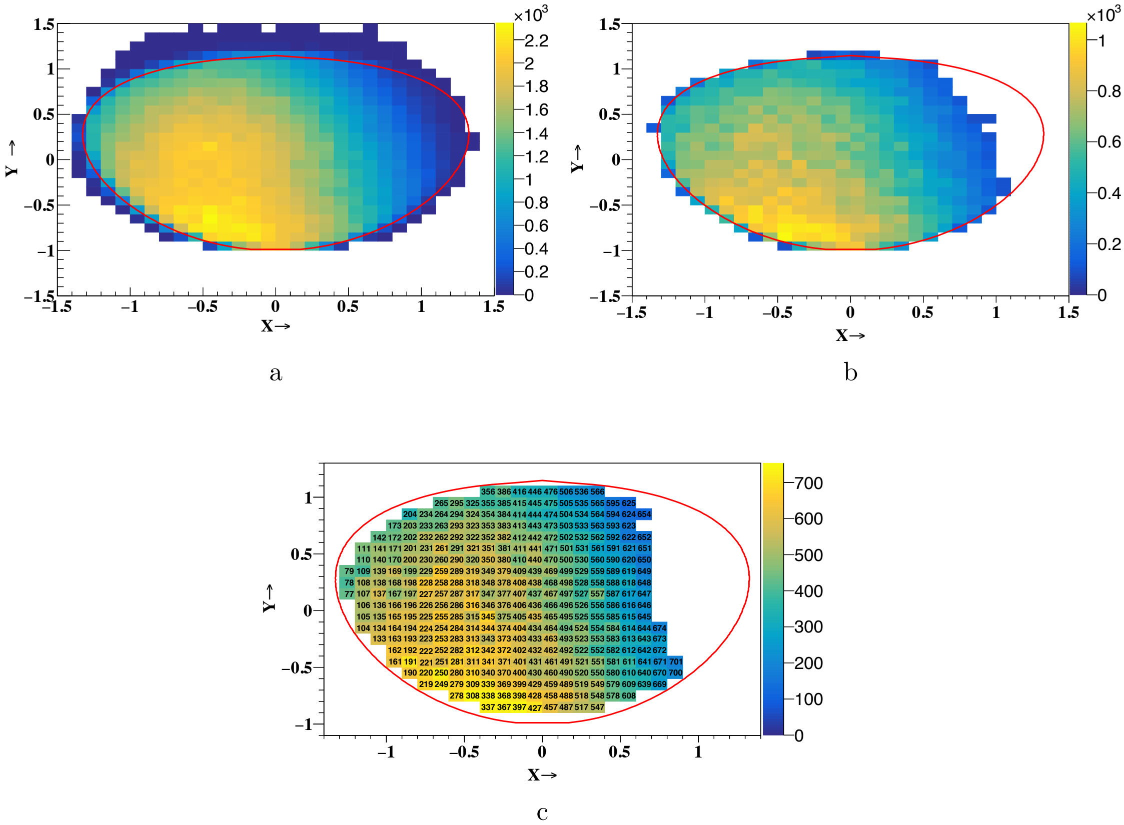

Figure 4.9: Dalitz plot shown in figure (a) has all events before background subtraction and (b) is after bin-wise non-resonant and in-peak background subtraction. The figure (c) shows the Dalitz plot with global bin number after rejecting bins with low acceptance, outside and on the boundary bins. The red curve shown in the figure is the phase space boundary of the $\eta' \to \eta\, \pi^+\, \pi^-$ decay.

4.4 Comparison of Kinematic Variables from Data and Simulation

The comparison of the kinematic variables are done with 5×10^8 generated events of the γ p $\rightarrow \eta'$ p $\rightarrow \eta\ \pi^+\ \pi^-$ p decay from the simulation and *g12* data. The incident number of beam photon in the event generation model is inversely proportional to the energy of the incident beam photon to produce a bremsstrahlung nature. The η' meson production angle is also made to follow the differential cross-section distribution of the η' from *g11* experiment [43]. To check how well the simulation explains the *g12* data a comparison of the kinematic variables namely the momentum (P), polar angle (θ) and azimuthal angle (ϕ) for π^+, π^- and p along with beam photon energy in the center-of-mass ($\sqrt{s}$) are shown in the Fig. 4.12, 4.13, 4.14 & 4.11 respectively. The simulated events and *g12* data are passed through all the selection criterion described in Section 3.3 and Section 3.4. The simulation shows reasonable agreement with the *g12* data. Even the ϕ distribution of particles in simulation mimics the sector dependent behavior of data well. These agreements led us to select this model in simulation for further analysis.

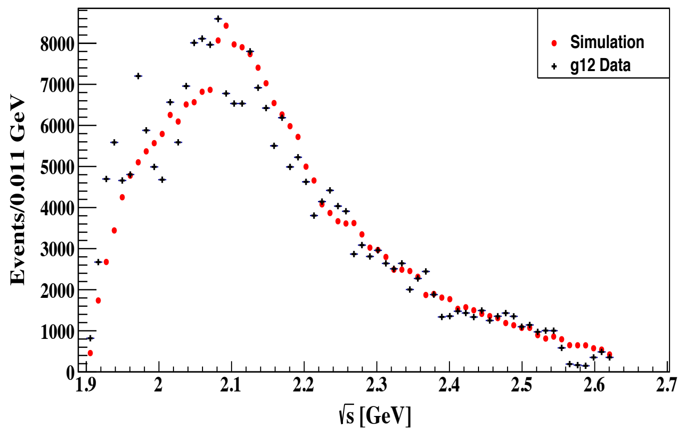

Figure 4.11: Distribution of the number of beam photons as a function of $\sqrt{s}$, the center of mass energy. Black points are for data, red points are results of MC simulation.

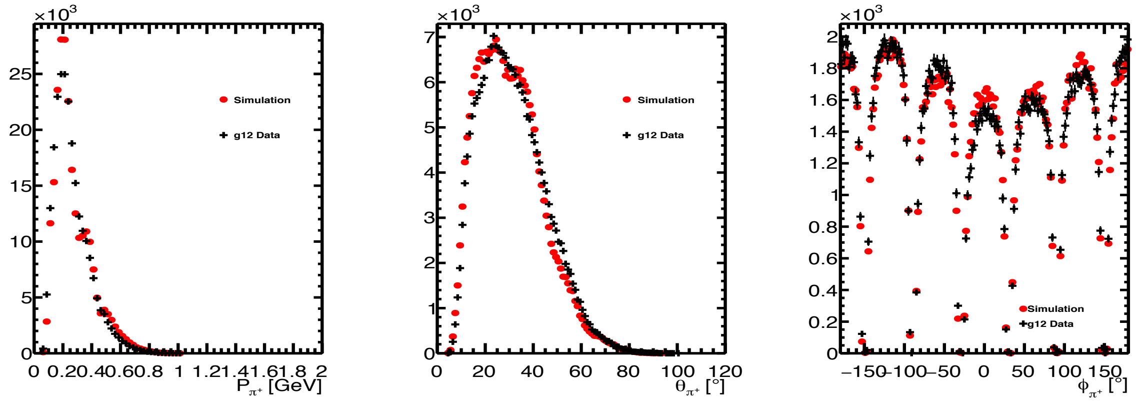

Figure 4.12: Comparison of momentum (left), polar angle (middle) and azimuthal angle (right) for π^+ meson between simulated (red) events and *g12* data (black).

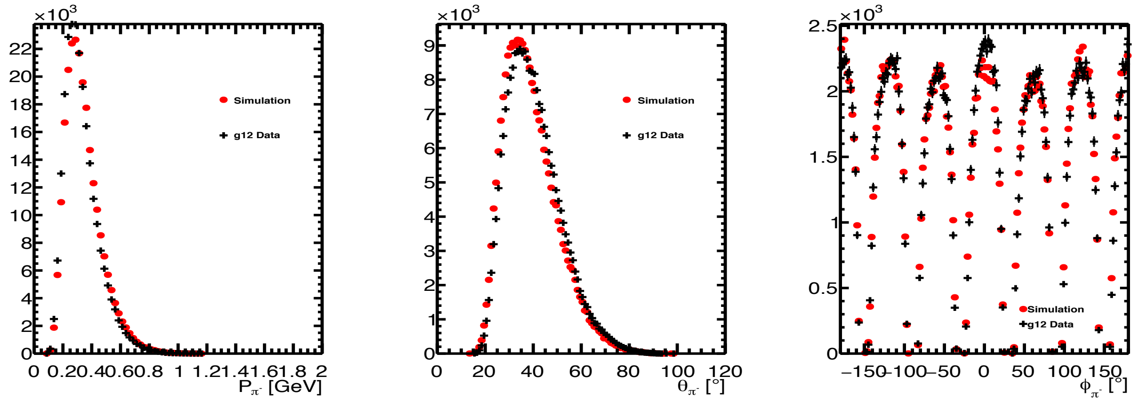

Figure 4.13: Comparison of momentum (left), polar angle (middle) and azimuthal angle (right) for π^- meson between simulated (red) events and *g12* data (black).

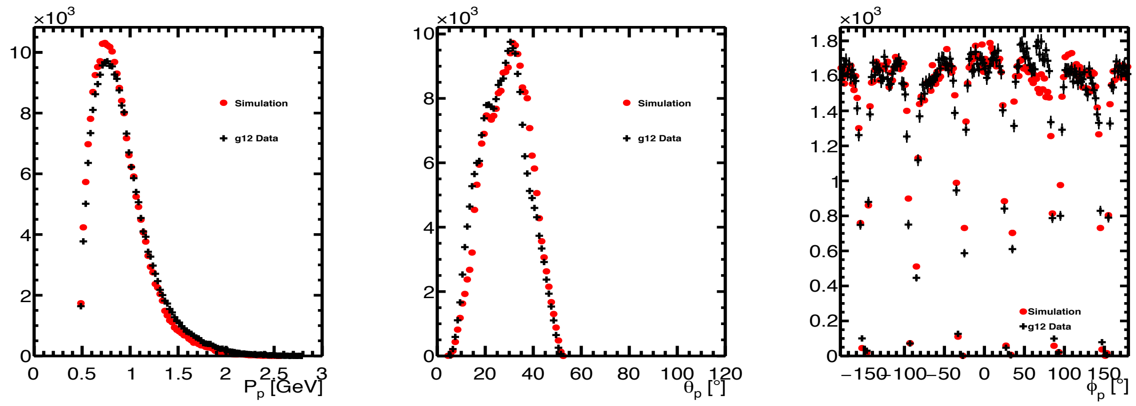

Figure 4.14: Comparison of momentum (left), polar angle (middle) and azimuthal angle (right) for proton between simulated (red) events and *g12* data (black).

4.5 Comparison of Normalized Cross-section

As a cross-check to the analysis a comparison of the differential cross-section ($d\sigma/d\Omega$) with the $cos(\theta)_{cm}$ (in center of mass frame of η') and $\sqrt{s}$ (energy in center of mass frame) are presented in the Fig. 4.15 for the γ p $\rightarrow$ p η' channel. The comparison of the differential cross-section from the *g12* dataset containing "good" [38] run numbers to the *g11* data [43] extracted from the Durham database [44] are presented here. All the comparisons use a common coverage of $\sqrt{s}$ spanning from 1.96 to 2.73 GeV and $cos(\theta)_{cm}$ from -0.65 to 0.65 rad. Fig. 4.15(a) shows distribution $\sqrt{s}$ integrated from 1.96 to 2.73 GeV and used an arbitrary scaling of 0.06. The Fig. 4.15(b) shows $cos(\theta)_{cm}$ distribution integrated from -0.65 to 0.65 rad and used an arbitrary scaling of 2.6 to normalize.

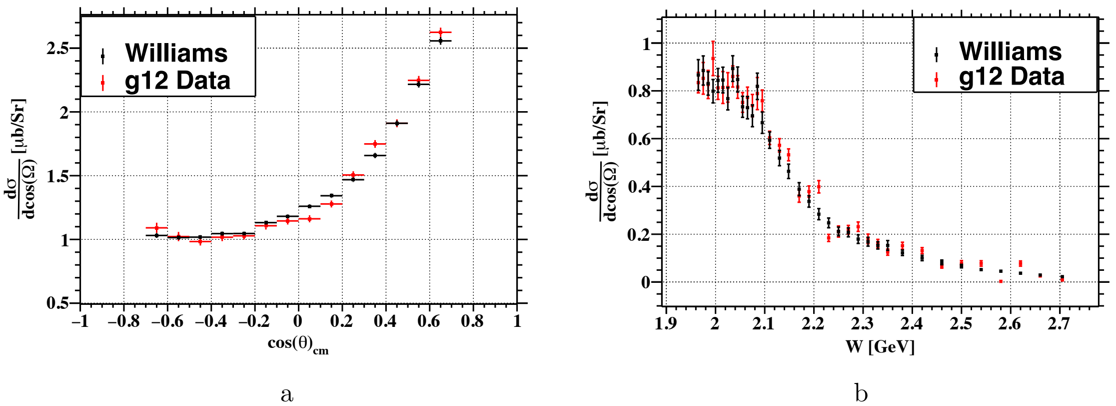

Figure 4.15: Comparison of $d\sigma/d\Omega$ versus (a) $cos(\theta)_{cm}$ and versus (b) W (or $\sqrt{s}$) for the γ p $\rightarrow$ p η' channel from the *g12* data and the published results from the *g11* data [43].

In the present analysis, however, $cos(\theta)_{cm}$ in center of mass frame of η' meson ranges from 0.85 to -0.85 rad and E_γ(Beam Energy) from 1.45 to 3.6 GeV for the $\eta' \rightarrow \eta\ \pi^+\ \pi^-$ decay. A comparison of acceptance corrected Dalitz variables X and Y distribution is made with 15 bins in both X and Y in different subranges of $cos(\theta)_{cm}$ and E_γ. The X and Y distributions are normalized to the central bin positioned at zero. Fig. 4.16 shows the distribution of X and Y for the whole $cos(\theta)_{cm}$ of η' from -0.85 to 0.85 rad and then in the subranges from 0 to 0.85 rad and -0.85 to 0 rad. In a similar way the X and Y distributions are compared for three E_γ subranges (1.45 to 1.8 GeV, 1.8 - 2.3 GeV and 2.3 - 3.6 GeV) shown in Fig. 4.17.

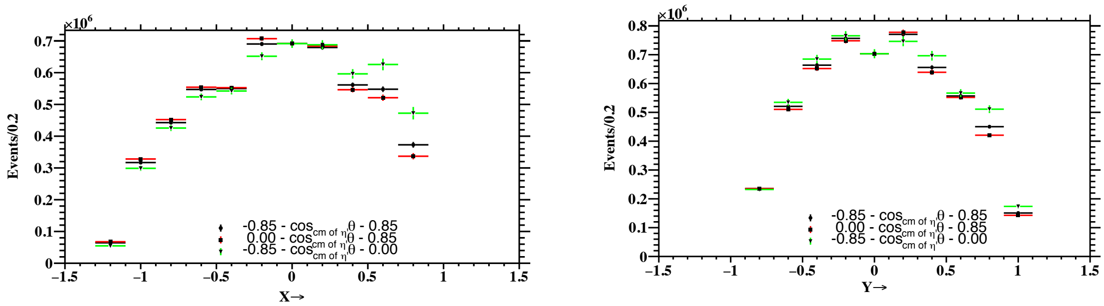

a b

Figure 4.16: Comparison of normalized and acceptance corrected Dalitz variables (a) X and (b) Y distribution for $\eta' \rightarrow \eta\ \pi^+\ \pi^-$ decay for the subranges of $\cos(\theta)_{cm}$ in center of mass frame of η'.

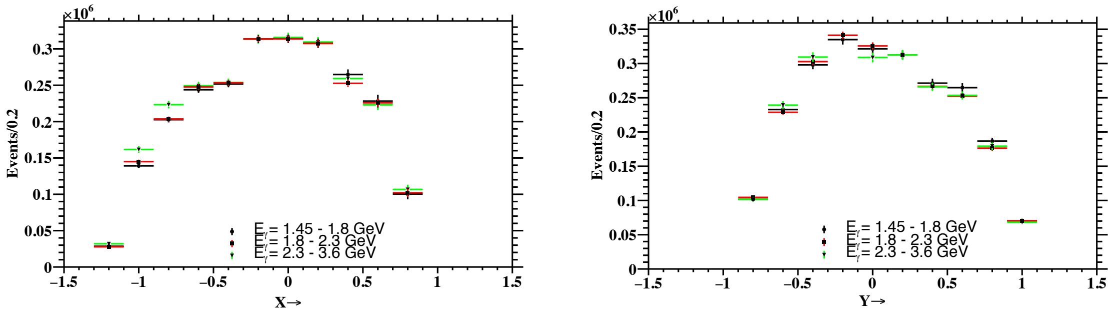

a b

Figure 4.17: Comparison of normalized and acceptance corrected Dalitz variables (a) X and (b) Y distribution for $\eta' \rightarrow \eta\ \pi^+\ \pi^-$ decay for the subranges of E_γ in center of mass frame of η'.

4.6 Fit Method and Results

In this section following two methods are described which has been used to calculate the Dalitz plot parameters.

- Acceptance correction method
- Smearing matrix method

In the first method, the $\eta' \rightarrow \eta\, \pi^+\, \pi^-$ contribution for each Dalitz plot bin is corrected for acceptance, without considering the migration of events from one bin to the other. Whereas, in the second method the fits are performed directly to the Dalitz plot from data along with a function. This function takes care of the acceptance in the same bin and also acceptance due to the migration from neighboring bins using a smearing matrix.

To calculate the acceptance function for both the methods a total of 0.5 billions events were generated with the set of input Dalitz plot parameters a = -0.150, b = -0.150, c = 0.0 and d = -0.080 in the MC simulation. Many iterations with different input Dalitz plot parameters were performed and finally, the above mentioned parameters were used as an input, which is close to the final Dalitz plot parameter values from this analysis.

In both the methods, a binned Dalitz plot is fitted with a general parametrization function ($A(1+aY+bY^2+cX+dX^2)$) also given in equation 1.14 is used for reporting the Dalitz plot parameters. The fitting is performed with the least square fitting procedure using MINUIT package available in the ROOT [40], which minimizes the χ^2 in each bin of the Dalitz plot [53]. The total number of 337 bins are fitted in the Dalitz plot and 5 parameters are included in the fit, which leads to a number of degrees of freedom (ndf) = 337 - 5 = 332.

4.6.1 Acceptance Correction Method

A calculation of X and Y variable is done for all the events and filled in the 30 $\times$ 30 binned Dalitz plot. In every bin of this Dalitz plot, background subtraction and elimination of bins are performed as explained in Section. 4.1. Every bin of this Dalitz plot has been corrected for acceptance.

Calculation of Acceptance

The generated and the reconstructed events are filled separately in two 30×30 binned Dalitz plot. Then a calculation of acceptance (ϵ_i) and error on acceptance (σ_{ϵ_i}) for each bin are made as follows:

$$\epsilon_i = \frac{N_{rec,i}}{N_{gen,i}} \tag{4.5}$$

$$\sigma_{\epsilon_i} = \sqrt{\frac{\epsilon_i(1-\epsilon_i)}{N_{gen,i}}} \tag{4.6}$$

where, $N_{rec,i}$ and $N_{gen,i}$ are the number of reconstructed and generated events in i^{th} bin [54]. The error on the acceptance for global bin i are calculated considering the binomial distribution of events [55].

Acceptance Correction

The number of corrected events ($N_{Cor,i}$) and propagated error ($\sigma_{Cor,i}$) for each bin after the acceptance correction are given by,

$$N_{Cor,i} = \frac{N_i}{\epsilon_i} \tag{4.7}$$

$$\sigma_{Cor,i} = \sqrt{\left(\frac{\sigma_i}{\sigma_{\epsilon_i}}\right)^2 + \left(\frac{N_i \sigma_{\epsilon_i}}{\epsilon_i^2}\right)^2}. \tag{4.8}$$

Extraction of Parameters

The χ^2 minimization to each bin of the Dalitz plot is done using the equation given below.

$$\chi^2 = \sum \left(\frac{N_{Cor,i} - f(X_i, Y_i)}{\sigma_{Cor,i}}\right)^2 \tag{4.9}$$

where X_i and Y_i are the central value of each bin, and $f(X_i, Y_i)$ denotes the fitted form of the polynomial for Dalitz plot bin i ($i = 1, 2, ..., n$). The fit includes five

Table 4.2: The correlation matrix for the Dalitz plot parameters in the acceptance correction method.

	A	a	b	c	d
A	1.000	0.324	-0.661	-0.051	-0.465
a	0.324	1.000	-0.519	0.079	-0.114
b	-0.661	-0.519	1.000	0.005	0.172
c	-0.051	0.079	0.005	1.000	0.727
d	-0.465	-0.114	0.172	0.727	1.000

free parameters, the fitted values of these parameters and the correlation matrix are given below :

A : 18915.851235 $\pm$ 112.470024

a : -0.151113 $\pm$ 0.006797

b : -0.158291 $\pm$ 0.011547

c : 0.013823 $\pm$ 0.009166

d : -0.077950 $\pm$ 0.012170

χ^2/ndf : 392.7/332 = 1.18

The correlation matrix given in the Table 4.2 shows the correlation between the fit parameters. It shows that parameters a and b have high anti-correlation among them. The parameters c and d show strong correlation. The overall fit to the Dalitz plot shows a reasonable χ^2/ndf of 1.18. These parameters from the fit are the Dalitz plot parameters.

4.6.2 Smearing Matrix Method

The events are migrated in the neighboring bins due to a varying resolution of final state particles proton, π^+ and π^-. These migrations are also non-uniform within the phase space of the $\eta' \to \eta\ \pi^+\ \pi^-$ decay, as the resolution is energy dependent phenomena. This method can take care of migrated events from one bin to the other, by calculating an acceptance in the form of the smearing matrix ($\epsilon_{n,m}$). To calculate the matrix, events are generated in each bin of the Dalitz plot and the acceptance for all the bins are calculated and stored in the form of a matrix. The final matrix contains the pure acceptance of an individual bin and also the acceptance from neighboring migrated bins. For events generated in the j^{th} bin, the acceptance is calculated for all i^{th} Dalitz plot bins as shown below:

$$\epsilon_{i,j} = \frac{N_{rec,gen}(i,j)}{N_{gen}(j)} \tag{4.10}$$

where $N_{rec,gen}$(i,j) denotes the number of events reconstructed in i^{th} bin when events are generated in the j^{th} bin.

Fit to the Dalitz Plot

Similar to the earlier method, a 30 $\times$ 30 binned Dalitz plot of the $\eta' \to \eta\ \pi^+\ \pi^-$ events from the data is filled after background subtraction and bins are eliminated. Thereafter a fit to the Dalitz plot is performed with the general parameterization function as given by the equation 1.14 is performed. The χ^2 minimization of the Dalitz plot bins are given by,

$$\chi^2 = \sum_{i=1}^{Nbins} \left(\frac{N_i - \sum_{j=1}^{Nbins} \epsilon_{i,j} N_{theory,j}}{\sigma_{Tot,i}} \right)^2 \tag{4.11}$$

where,

- the N_i is the number of $\eta' \to \eta\ \pi^+\ \pi^-$ events in the i^{th} Dalitz plot bin.
- $\epsilon_{i,j}$ is acceptance in a smearing matrix, which is equal to the acceptance of j^{th} bin when events are generated in the ith bin only.
- $\sigma_{Tot,i} = \sqrt{\sigma_i^2 + \sum_{j=1}^{Nbins} N^2_{theory,j} \frac{\epsilon_{i,j}(1-\epsilon_{i,j})}{N_{gen,j}}}$ is the total error associated with i^{th} Dalitz plot bin assuming binomial distribution and neglecting the contribution from $N_{theory,j}$ [56].
-

$$N_{theory,j} = \oiint\limits_{Boundary} A(1 + aY + bY^2 + cX + dX^2)dXdY \tag{4.12}$$

To calculate the integral function given by equation 4.12, the integration using the Monte-Carlo method is applied within the boundary of the Dalitz plot.

$$N_{theory,j} = A \oiint\limits_{Boundary} dXdY + Aa \oiint\limits_{Boundary} YdXdY + Ab \oiint\limits_{Boundary} Y^2dXdY$$
$$+Ac \oiint\limits_{Boundary} XdXdY + Ad \oiint\limits_{Boundary} X^2dXdY$$

$$N_{theory,j} = A(\alpha_1 + a\alpha_2 + b\alpha_3 + c\alpha_4 + d\alpha_5)$$

Where,

$$\alpha_1 = \oiint\limits_{Boundary} \text{dX dY}$$
$$\alpha_2 = \oiint\limits_{Boundary} \text{Y dX dY}$$
$$\alpha_3 = \oiint\limits_{Boundary} Y^2 \text{ dX dY}$$
$$\alpha_4 = \oiint\limits_{Boundary} \text{X dX dY}$$
$$\alpha_5 = \oiint\limits_{Boundary} X^2 \text{ dX dY}$$

The aim here is to evaluate the integral α_1, α_2, α_3, α_4 and α_5. To accomplish the task, uniform random numbers are generated in pair of Dalitz variable X and Y within -1.5 to 1.5 using TRandom3 random number algorithm in the ROOT [40] framework and saved in a binned two-dimensional histogram. If the generated pair lies inside the kinematic boundary of the decay then the binned two-dimensional histogram for each integral is filled, where the integrand becomes the weight of the histogram. For instance: histogram for integral α_1 is assigned a weight of 1, the histogram for integral α_2 is assigned a weight of Y, integral α_3 is assigned a weight of Y^2 so on and so forth. These histograms for each integral are then divided by the generated histogram and multiplied by the bin size to give the value of integration inside the Dalitz plot for each bin. It is later translated into a global binning and used directly in the equation 4.11. The error from integration is proportional to $(\frac{1}{\sqrt{N}})$, where, "N" being the sample size, which is safely neglected due to the generation of 10^8 events in the MC integration.

Results from the Smearing Matrix Method Fit

The fits to each global bin of the Dalitz plot is shown in the Fig. 4.18 and the fits to the individual Dalitz plot bins in 30 different X bins for the whole Y range and vice-versa are shown in the Fig. 4.19 and Fig. 4.20 respectively. The fit results of the general parameterization to the data Dalitz plot as shown below along with the correlation matrix is given in the Table 4.3. The correlation matrix shows strong anti-correlation between a and b and high correlation among variable c and d. The parameter a or b are very loosely correlated to either of the parameter c and d. A loose correlation among two variables signifies that the measurement of one parameter does not affect the other.

A : 1857201.9098 $\pm$ 11506.4247

a : -0.1508 $\pm$ 0.0069

b : -0.1514 $\pm$ 0.0120

c : 0.0128 $\pm$ 0.0094

d : -0.0813 $\pm$ 0.0127

χ^2/ndf : 385.67/332 = 1.16

Table 4.3: Correlation matrix for the Dalitz plot parameters calculated by the smearing matrix method.

	A	a	b	c	d
A	1.000	0.319	-0.669	-0.079	-0.490
a	0.319	1.000	-0.526	0.079	-0.108
b	-0.669	-0.526	1.000	0.013	0.185
c	-0.079	0.079	0.013	1.000	0.731
d	-0.490	-0.108	0.185	0.731	1.000

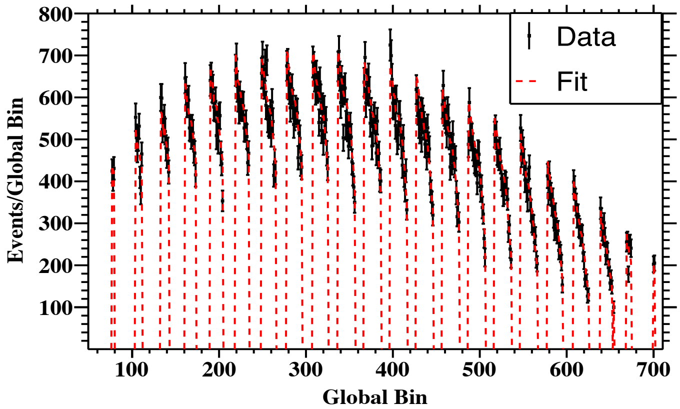

Figure 4.18: Global bin versus background subtracted $\eta' \rightarrow \eta\ \pi^+\ \pi^-$ events and in the red is the fitted function from the smearing matrix method.

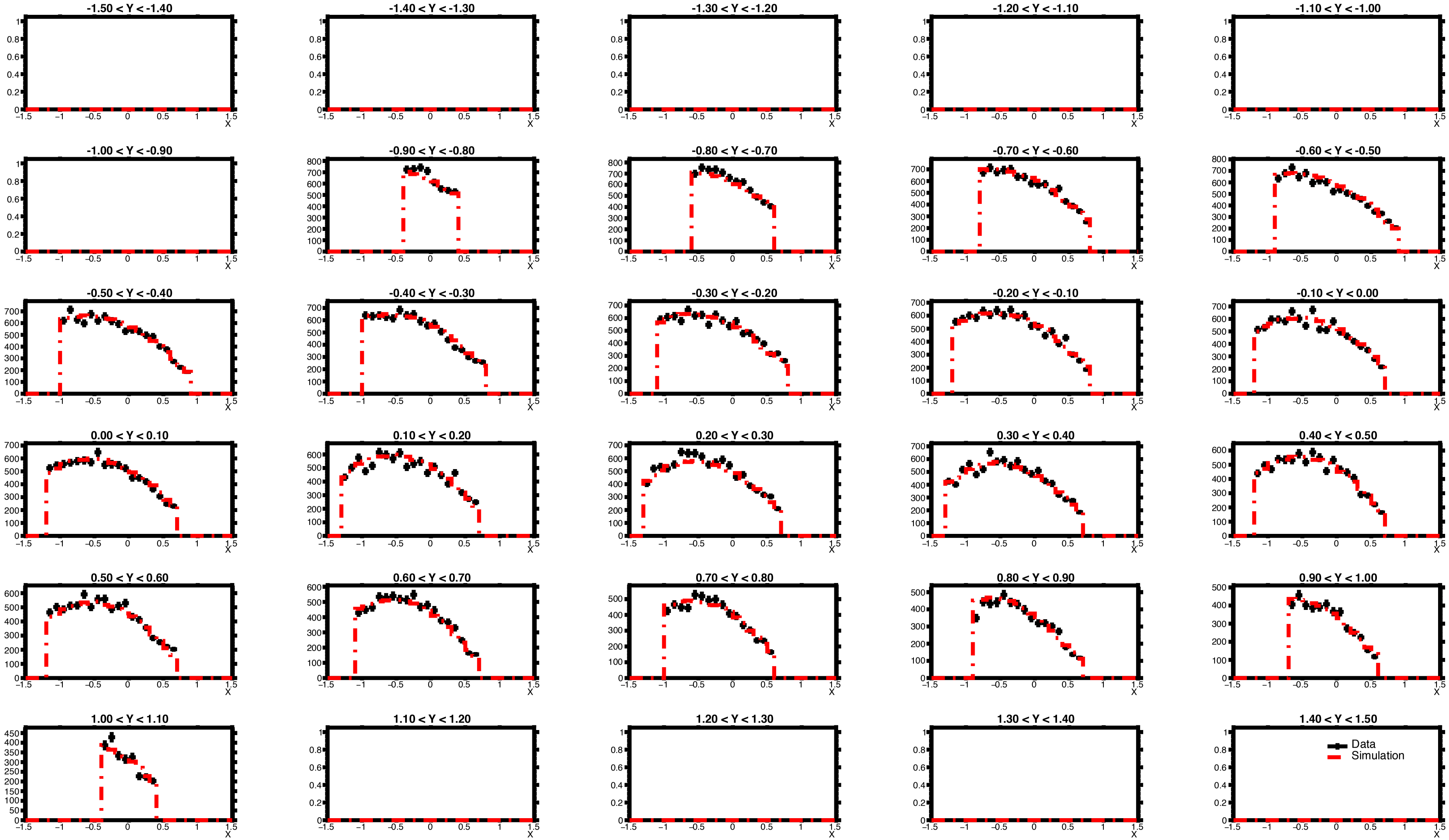

Figure 4.19: The projection of the Dalitz variable X in all 30 different bins of Y. The black point is the pure data with error bar and the red line is the fit with parameters values from the smearing matrix method.

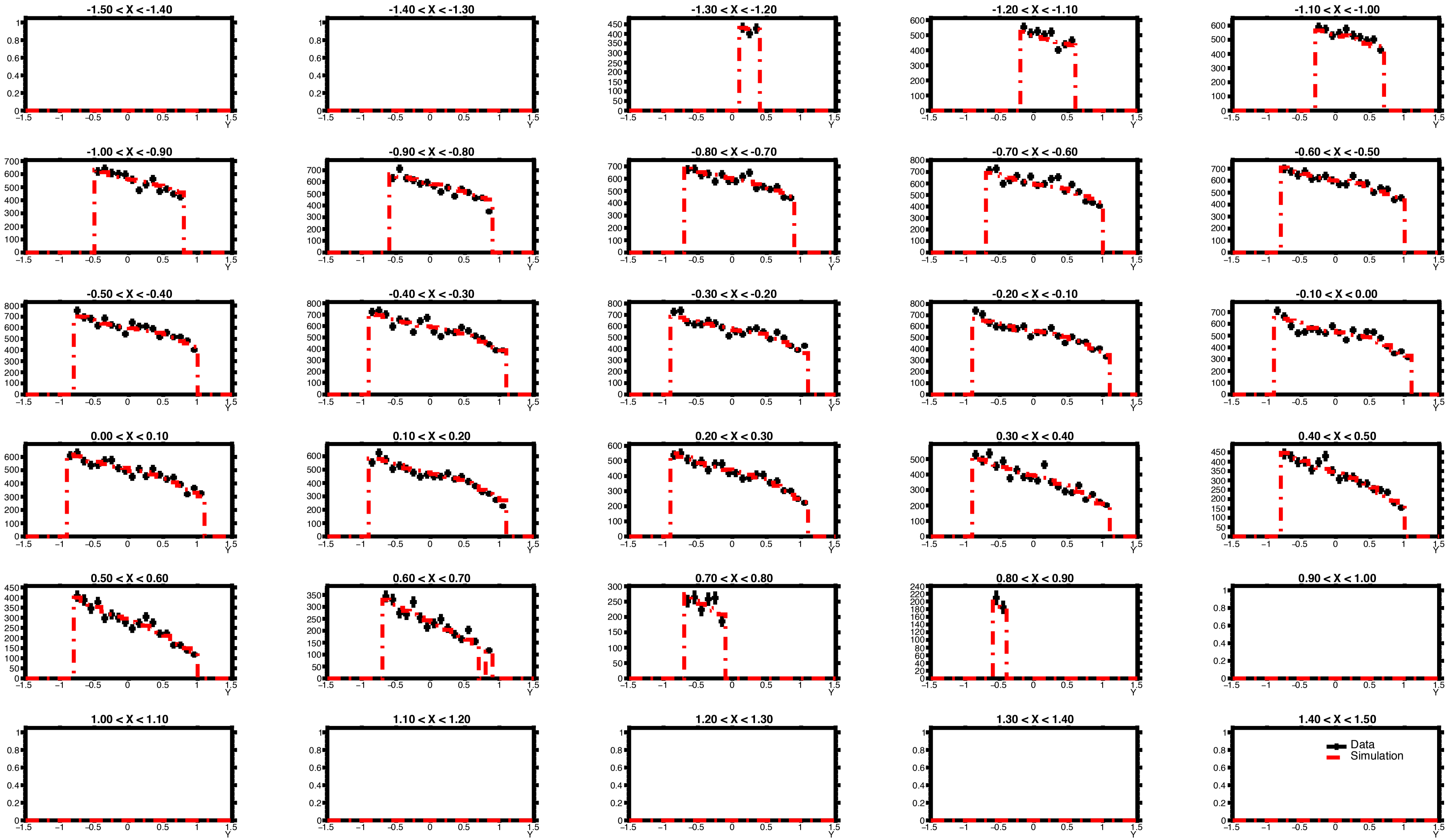

Figure 4.20: The projection of the Dalitz variable Y in all 30 different bins of X. The black point is the pure data with error bar and the red line is the fit with parameters values from the smearing matrix method.

4.7 Selection of the Fit Method

Both the methods yield very close results, primarily because of the reason that the Dalitz plot uses wide binning roughly three times the resolution of X and Y. All the required quantities to reproduce the results of both the methods are listed in Appendix B. The correlation matrix from both methods shows similar correlations among the variables. The parameters a and b being function of variable Y are c and d being function of variable X is expected to have a correlation among them which is observed in both matrix in the Table 4.2 & 4.3. The fits in both the methods yield a χ^2/ndf which is closer to 1. The advantage of Acceptance Correction Method over Smearing Matrix Method are the space and time complexity of the computation. Acceptance Correction Method utilizes less memory, computation time and power when compared to Smearing Matrix Method. However, the Smearing Matrix Method Fit presents a more accurate way to deal with the acceptances separately from the generated and the reconstructed bins after migration. Hence, the Smearing Matrix Method fit has been accepted as the way forward to present the final results as well as to do the systematic studies for further analysis.

Chapter 5

Systematic Errors

Any measurement with some tool, instrument or method comes with an error which cannot be removed. These errors are described in the chapter as systematic errors. These errors are generally tedious to exactly quantify and sometimes the exact source of error is challenging to point out in the final output of the measurement. An estimate of the highest contribution is generally considered and added as a variance to the measurement. In order to calculate systematics from the sources, different datasets are created by varying only one condition at a time. These datasets are sometimes independent or dependent determined by the source of systematic error. Hence, in this thesis the sources of systematic errors are divided into two types, first, assuming the different dataset for sources to be independent and second, the different dataset for sources to be dependent. Systematic calculations for these type of sources are different and presented in two distinct sections. The calculation of the Dalitz parameters are done using the smearing matrix method and the error estimates are different for these two types of systematic error sources. The final section summarizes the final systematic errors of each parameter.

This chapter describes in details the calculation of the systematic errors for the sources and is also shown in Fig. 5.1. All the sources does not contribute to the systematics, but it depends on the magnitude of the error [57]. Errors which are large and cannot be explained by the statistical fluctuation of the measurement finally contribute to the result by adding all the errors from the sources in quadrature.

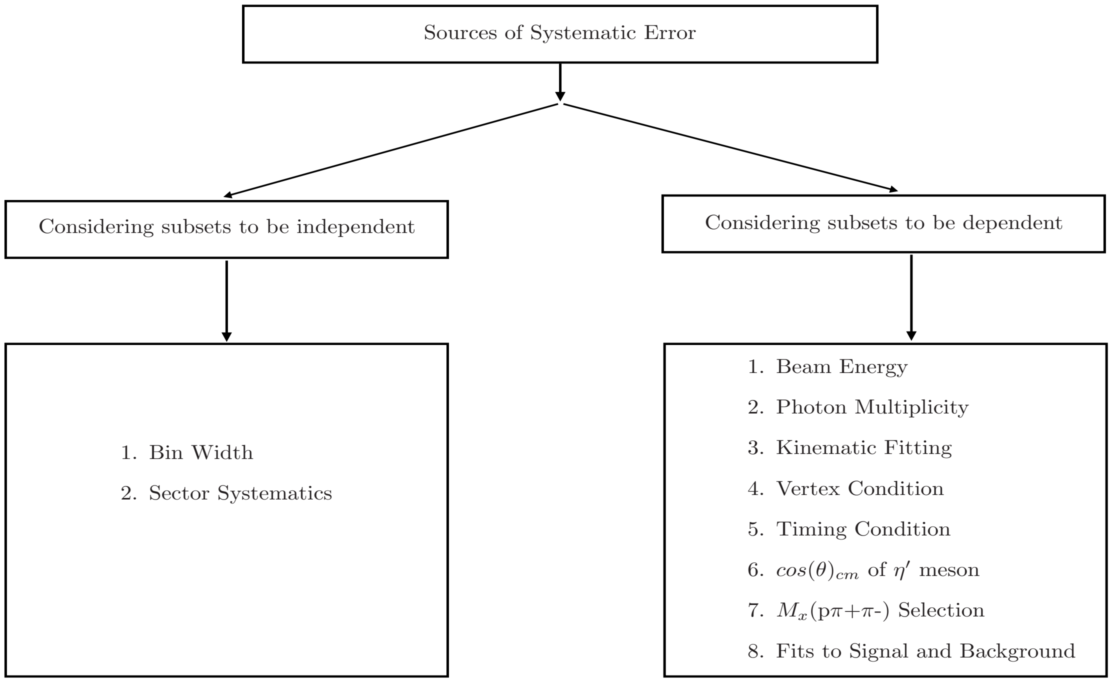

Figure 5.1: Pictorial diagram enumerating the sources of the systematic errors studied.

5.1 Independent Subsets for a Source

In this section, the systematical effects have been studied for the conditions and selections. The following two systematics are studied assuming that the sources of systematic errors are uncorrelated.

- Bin Width
- Sector Systematics

Different configuration for the above factor is studied and Dalitz plot parameters are calculated for each of the configuration from the smearing matrix method. The systematic error is then calculated as the weighted standard deviation, thus the weighted mean ($\bar{x}$) and standard deviation (σ_x) for parameter x_i with error σ_{x_i} for the configuration "i" is given by,

$$\bar{x} = \frac{\sum_{i=1}^{i=max} \frac{x_i}{\sigma_{x_i}^2}}{\sum_{i=1}^{i=max} \frac{1}{\sigma_{x_i}^2}}, \sigma_x = \sqrt{\frac{\sum_{i=1}^{i=max} \frac{(x_i-\bar{x})^2}{\sigma_{x_i}^2}}{\sum_{i=1}^{i=max} \frac{1}{\sigma_{x_i}^2}}}. \tag{5.1}$$

5.1.1 Bin Width

The present section is meant to analyse the effect on the choice of binning on the Dalitz plot parameters. This analysis used an optimum binning based on 160090 $\eta' \to \eta\, \pi^+\, \pi^-$ events from the *g12* data. The optimization is between the quality of the fits of the individual Dalitz plot bins and maximum ndf of the Dalitz plot parameters. Finally, in the standard analysis, a bin width of $\approx 3\sigma$ is used which corresponds to a 30 $\times$ 30 bins ranging from -1.5 to 1.5 for X and Y variables. The reason behind the selection of equal numbers of bins for X and Y is the same resolution of X and Y variables. Further, the Dalitz plot binning are allowed to vary from 25 $\times$ 25 bins to 35 $\times$ 35 bins for the systematic studies. The Dalitz plot parameters are extracted keeping all the other conditions fixed for all these 11 different configurations of different binning in which the standard 30 x 30 bins being the central configuration. The systematic error is calculated as the weighted standard deviation, thus, the weighted mean ($\bar{x}$) and standard deviation (σ_x) of parameter x_i with error σ_{x_i} for the configuration "i" is given by,

$$\bar{x} = \frac{\sum_{i=1}^{11} \frac{x_i}{\sigma_{x_i}^2}}{\sum_{i=1}^{11} \frac{1}{\sigma_{x_i}^2}} \tag{5.2}$$

$$\sigma_x = \sqrt{\frac{\sum_{i=1}^{11} \frac{(x_i-\bar{x})^2}{\sigma_{x_i}^2}}{\sum_{i=1}^{11} \frac{1}{\sigma_{x_i}^2}}}. \tag{5.3}$$

The value of the Dalitz plot parameters for all configurations along with the calculated systematic error is given in the Table 5.1 and also shown in the Fig. 5.2.

5.1.2 Sector Systematics

The CLAS detector comprises of six different sectors with different acceptance and resolution, which makes every sector acts as an individual detector. To study the systematic arising from different CLAS sectors, six different configurations are studied, wherein, a single sector is excluded every time and the Dalitz plot parameters are calculated. It is repeated for all six sectors, the weighted mean ($\bar{x}$)

Table 5.1: The number of bins for the calculation of the systematic error and the corresponding Dalitz plot parameters.

Bins	a	b	c	d	χ^2**/ndf**
25 × 25	-0.153 ± 0.007	-0.152 ± 0.013	0.020 ± 0.009	-0.068 ± 0.013	$\frac{290.65}{229}$ = 1.27
26 × 26	-0.155 ± 0.007	-0.152 ± 0.012	0.018 ± 0.009	-0.081 ± 0.012	$\frac{260.80}{248}$ = 1.05
27 × 27	-0.157 ± 0.007	-0.153 ± 0.012	0.024 ± 0.009	-0.071 ± 0.013	$\frac{330.92}{265}$ = 1.25
28 × 28	-0.163 ± 0.007	-0.151 ± 0.012	0.014 ± 0.010	-0.074 ± 0.013	$\frac{361.46}{289}$ = 1.25
29 × 29	-0.156 ± 0.007	-0.152 ± 0.012	0.014 ± 0.009	-0.085 ± 0.012	$\frac{358.64}{313}$ = 1.15
30 × 30	-0.151 ± 0.007	-0.151 ± 0.012	0.013 ± 0.009	-0.081 ± 0.013	$\frac{385.67}{332}$ = 1.16
31 × 31	-0.153 ± 0.007	-0.149 ± 0.012	0.017 ± 0.010	-0.078 ± 0.013	$\frac{417.10}{352}$ = 1.18
32 × 32	-0.161 ± 0.007	-0.148 ± 0.011	0.008 ± 0.010	-0.089 ± 0.013	$\frac{428.97}{375}$ = 1.14
33 × 33	-0.156 ± 0.007	-0.153 ± 0.012	0.011 ± 0.010	-0.084 ± 0.013	$\frac{444.53}{398}$ = 1.12
34 × 34	-0.157 ± 0.007	-0.149 ± 0.012	0.012 ± 0.010	-0.081 ± 0.013	$\frac{467.48}{418}$ = 1.12
35 × 35	-0.163 ± 0.007	-0.147 ± 0.012	-0.002 ± 0.010	-0.096 ± 0.013	$\frac{458.76}{441}$ = 1.04
$\bar{x}$	-0.157	-0.151	0.014	-0.080	
± σ_x	0.0038	0.0020	0.0064	0.0075	

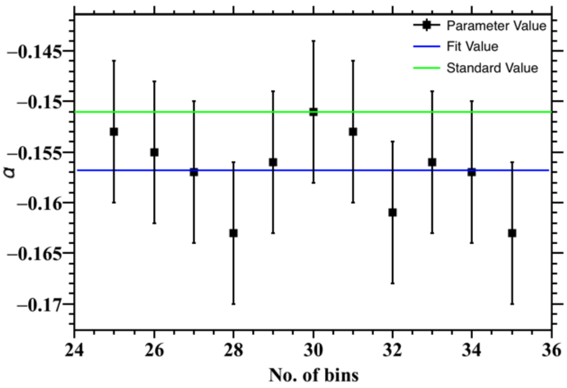

a

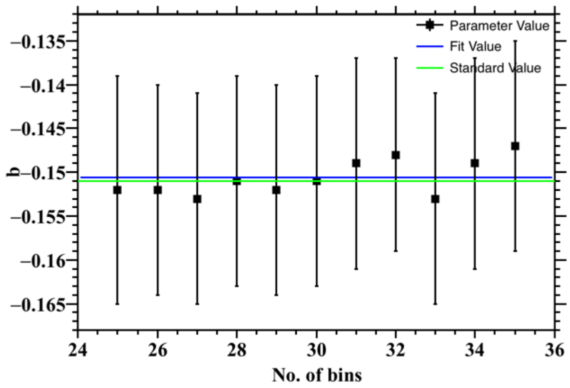

b

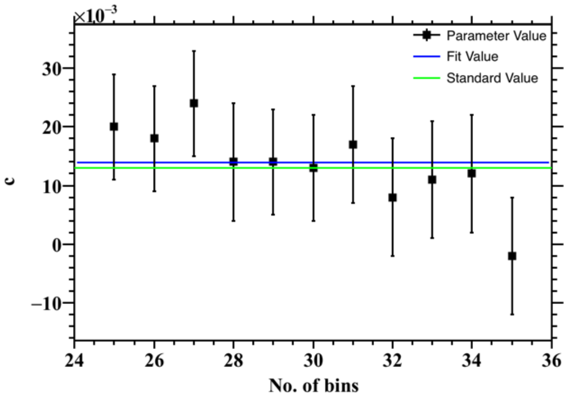

c

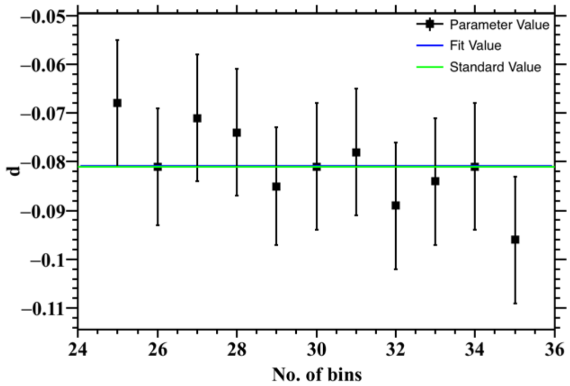

d

Figure 5.2: The four figures (a), (b), (c) and (d) shows the Dalitz plot parameters a, b, c, and d respectively, calculated for 25 × 25 bins to 35 × 35 bins for the X and Y variables. The green lines show the results of the standard analysis (30 × 30 bins) and the blue lines depict the weighted mean value.

and standard deviation (σ_x) for parameters x_i with error σ_{x_i} are used to give the systematic error for the CLAS sectors. The value of the Dalitz plot parameters for six different configurations along with the calculated systematic error is given in the Table 5.2 and also shown in the Fig. 5.3.

Table 5.2: Systematic errors in the Dalitz plot parameters from different combinations of five sectors of CLAS detector, excluding one sector each time.

Excluded	a	b	c	d	χ^2/**ndf**
Sector 1	-0.153 ± 0.008	-0.145 ± 0.014	0.011 ± 0.011	-0.081 ± 0.014	$\frac{359.97}{329} = 1.09$
Sector 2	-0.142 ± 0.008	-0.145 ± 0.013	0.007 ± 0.011	-0.082 ± 0.014	$\frac{363.90}{328} = 1.11$
Sector 3	-0.150 ± 0.008	-0.149 ± 0.013	0.009 ± 0.011	-0.083 ± 0.014	$\frac{366.26}{326} = 1.12$
Sector 4	-0.164 ± 0.008	-0.152 ± 0.013	0.008 ± 0.010	-0.081 ± 0.014	$\frac{357.88}{330} = 1.08$
Sector 5	-0.156 ± 0.008	-0.160 ± 0.013	0.011 ± 0.011	-0.086 ± 0.015	$\frac{394.68}{325} = 1.21$
Sector 6	-0.146 ± 0.008	-0.146 ± 0.013	0.021 ± 0.010	-0.071 ± 0.014	$\frac{370.26}{330} = 1.12$
$\bar{x}$	-0.152	-0.150	0.011	-0.081	
$\pm\ \sigma_x$	0.0071	0.0053	0.0048	0.0046	

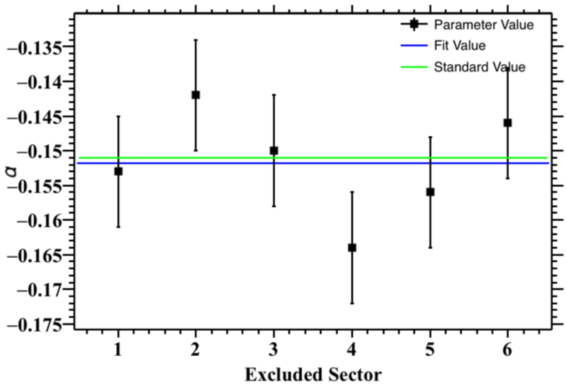

a

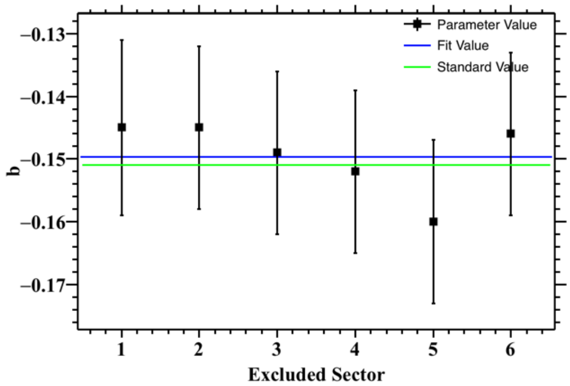

b

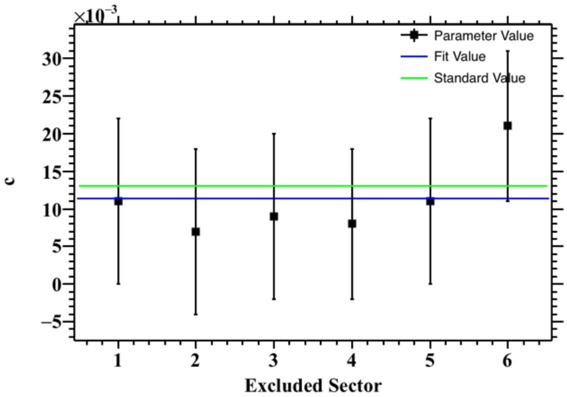

c

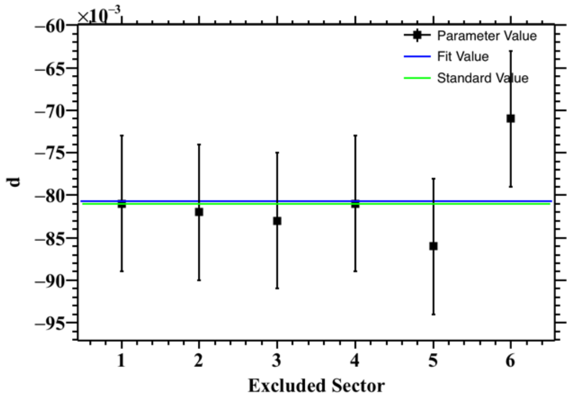

d

Figure 5.3: The four figures (a), (b), (c) and (d) shows the Dalitz plot parameters a,b,c and d respectively. The parameters a,b,c and d are calculated after excluding one sector each time for six different sectors in CLAS . The green lines show the results of the standard analysis and the blue lines depict the weighted mean value.

5.2 Dependent Subsets for a Source

In this section, those sources of systematic errors are studied which are correlated because independent datasets cannot be created for them. In these systematic studies, a single condition is changed at a time from the standard condition of the analysis for the whole dataset. Here, parameter error DP_x is of the same order of the standard parameter errors DP_{std}, so a new parameter ΔDP [57] is calculated as follows,

$$\Delta DP = \left| \frac{DP_{std} - DP_x}{\sigma_{std}} \right|. \tag{5.4}$$

If this new parameter ΔDP is greater than 1, then the systematic error is calculated for the source corresponding to this parameter.

These studies include the following sources of systematic errors:

- Beam Energy
- Photon Multiplicity
- Kinematic Fitting
- Vertex Condition
- Timing Condition
- $\cos(\theta)$ in the Center of Mass Frame of the η' meson
- M_x(pπ+π-) Selection
- Systematics from Fits to Signal and Background

5.2.1 Beam Energy

In the present analysis, the beam energy of the photon (E_γ) from the standard analysis is ranging from the threshold energy of the η' meson, 1.455 GeV to 3.6 GeV because the η' meson photo production drops after 3.6 GeV. The different subranges of the photon beam energy versus the number of $\eta' \to \eta\ \pi^+\ \pi^-$ events are shown in the Fig. 5.4. This leaves four subsets of E_γ while keeping all other conditions unchanged.

- 1.455 to 3.2 GeV
- 1.455 to 3.4 GeV
- 1.455 to 3.8 GeV
- 1.455 to 4.0 GeV

The reason behind selecting these overlapping subsets is that the Dalitz plot has a systematic dependency on a number of events and number of bins chosen. Therefore, choosing different subranges will not only drastically decrease the number of events to do the analysis, but also affect the fitting performed to the individual bins and the number of bins in the Dalitz plot. This will complicate the determination of systematic errors.

The systematic error is calculated from the difference between the standard analysis and the most deviated value of the parameters from these sets. The value of the Dalitz plot parameters for these four different sets are given in Table 5.3 and can be seen to have no effect on the parameters.

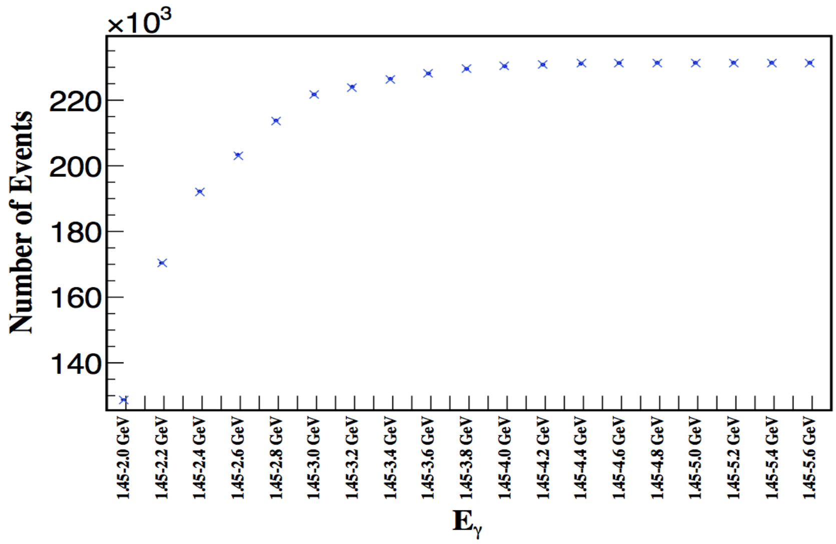

Figure 5.4: The different subranges of photon beam energy (E_γ) range versus background subtracted numbers of the η' meson events.

Table 5.3: The different subranges of beam energy (E_γ) and the corresponding Dalitz plot parameters.

E_γ **range (in GeV)**	a	Δa	b	Δb	c	Δc	d	Δd	χ^2**/ndf**
Standard	-0.151 $\pm$ 0.007		-0.151 $\pm$ 0.012		0.013 $\pm$ 0.009		-0.081 $\pm$ 0.013		$\frac{385.67}{332} = 1.16$
1.455-3.2	-0.153 $\pm$ 0.007	0.3	-0.148 $\pm$ 0.012	0.3	0.010 $\pm$ 0.009	0.3	-0.077 $\pm$ 0.013	0.3	$\frac{385.30}{331} = 1.16$
1.455-3.4	-0.153 $\pm$ 0.007	0.3	-0.146 $\pm$ 0.012	0.4	0.010 $\pm$ 0.009	0.3	-0.079 $\pm$ 0.013	0.2	$\frac{402.94}{332} = 1.21$
1.455-3.8	-0.149 $\pm$ 0.007	0.3	-0.156 $\pm$ 0.012	0.4	0.015 $\pm$ 0.009	0.2	-0.075 $\pm$ 0.013	0.5	$\frac{386.10}{332} = 1.16$
1.455-4.0	-0.149 $\pm$ 0.007	0.3	-0.155 $\pm$ 0.012	0.3	0.014 $\pm$ 0.009	0.1	-0.079 $\pm$ 0.013	0.2	$\frac{395.76}{333} = 1.19$

5.2.2 Photon Multiplicity

In the standard Dalitz plot analysis, the multiple beam photons in a single event are considered as individual events, which is already explained in Section. 3.3. Due to these combinations, there are 12 % more events than best-timed photon events. The Dalitz plot parameters are obtained for a set of events containing only the best-timed photon and compared to the standard Dalitz plot parameters in order to check the systematic error. The value of the Dalitz plot parameters is given in the Table 5.4. The parameters a and d seems to be affected by the selection of best-timed photon and their difference with the standard Dalitz plot parameters are taken as the systematic error. The systematic error comes out to be asymmetric with a value of $\sigma_a = {}^{+0.0}_{-0.009}$ and $\sigma_d = {}^{+0.0}_{-0.015}$ for parameter a and d respectively.

5.2.3 Kinematic Fitting

The standard analysis used a pull probability greater than 1% for all the selected events. To understand the systematics from this cut the pull probability cut is varied with an increment of 5% in four sets. The Dalitz plot parameters for all the sets are listed in the Table 5.5. It comes out that the pull probability greater than 1% has not contributed to the systematic error.

Table 5.4: The Dalitz plot parameters are calculated considering one photon in each event, and the chosen photon happens to be the best-timed photon.

Set	a	Δa	b	Δb	c	Δc	d	Δd	χ^2/**ndf**
Standard	-0.151 $\pm$ 0.007		-0.151 $\pm$ 0.012		0.013 $\pm$ 0.009		-0.081 $\pm$ 0.013		$\frac{385.67}{332} = 1.16$
Best-time γ	-0.142 $\pm$ 0.007	1.3	-0.157 $\pm$ 0.012	0.5	0.017 $\pm$ 0.010	0.4	-0.066 $\pm$ 0.013	1.2	$\frac{340.23}{332} = 1.02$

Table 5.5: A list of pull probability cut on the kinematic fitter and the corresponding Dalitz plot parameters.

KF Set	a	Δa	b	Δb	c	Δc	d	Δd	χ^2/**ndf**
Standard	-0.151 $\pm$ 0.007		-0.151 $\pm$ 0.012		0.013 $\pm$ 0.009		-0.081 $\pm$ 0.013		$\frac{385.67}{332}$ = 1.16
5%	-0.147 $\pm$ 0.007	0.6	-0.152 $\pm$ 0.012	0.1	0.016 $\pm$ 0.010	0.3	-0.073 $\pm$ 0.013	0.6	$\frac{390.08}{331}$ = 1.18
10%	-0.144 $\pm$ 0.007	1.0	-0.159 $\pm$ 0.012	0.7	0.019 $\pm$ 0.010	0.7	-0.069 $\pm$ 0.013	0.9	$\frac{358.63}{327}$ = 1.10
15%	-0.144 $\pm$ 0.007	1.0	-0.156 $\pm$ 0.013	0.4	0.018 $\pm$ 0.010	0.6	-0.074 $\pm$ 0.014	0.5	$\frac{343.72}{327}$ = 1.05
20%	-0.147 $\pm$ 0.007	0.6	-0.151 $\pm$ 0.013	0.0	0.015 $\pm$ 0.010	0.2	-0.072 $\pm$ 0.014	0.7	$\frac{317.93}{327}$ = 0.97

5.2.4 Vertex Condition

A cut on the target length along the z-vertex (-110 cm $\leq V_z \leq$ -70 cm) and the radius ($\sqrt{(V_x^2 + V_y^2)} \leq 2.0$ cm) of the target was placed to ensure that the γ and proton reaction takes place within the target dimension. The resolution of V_z and $\sqrt{(V_x^2 + V_y^2)}$ are 1 cm and 0.5 cm respectively. The systematic study is performed by varying V_z and $\sqrt{(V_x^2 + V_y^2)}$ cut independently within the resolution without changing any other cut. The parameter values for these studies are listed in Table 5.6.

It is found that the V_z and $\sqrt{(V_x^2 + V_y^2)}$ cut does not give any systematics to the measurement.

5.2.5 Timing Condition

The time difference $\mid (t_{vert}(TOF)$ - $t_{vert}(Tagger)) \mid$ less than equal to 1.0 ns on the detected final state particles p, π^+ and π^- was used in the standard analysis as shown in the Fig. 3.11. The systematic error is calculated by varying the standard

Table 5.6: The event vertex cut V_z and the $\sqrt{(V_x^2 + V_y^2)}$ cut are varied within the resolution and the corresponding Dalitz plot parameters.

Set	a	Δa	b	Δb	c	Δc	d	Δd	χ^2/**ndf**
Standard	-0.151 $\pm$ 0.007		-0.151 $\pm$ 0.012		0.013 $\pm$ 0.009		-0.081 $\pm$ 0.013		$\frac{385.67}{332}$ = 1.16
-109$\leq$ V_z $\leq$-71	-0.158 $\pm$ 0.007	1.0	-0.144 $\pm$ 0.012	0.6	0.011 $\pm$ 0.010	0.2	-0.085$\pm$ 0.013	0.3	$\frac{385.64}{329}$ = 1.17
$(V_x^2 + V_y^2)^{1/2}$ $\leq$ 1.5	-0.154 $\pm$ 0.007	0.4	-0.140 $\pm$ 0.013	0.9	0.013 $\pm$ 0.010	0.0	-0.081$\pm$ 0.014	0.0	$\frac{394.09}{327}$ = 1.17

Table 5.7: The list of timing cuts used in the systematic error calculation and the corresponding Dalitz plot parameters.

Set	a	Δa	b	Δb	c	Δc	d	Δd	χ^2/**ndf**
Standard	-0.151 $\pm$ 0.007		-0.151 $\pm$ 0.012		0.013 $\pm$ 0.009		-0.081 $\pm$ 0.013		$\frac{385.67}{332}$ = 1.16
0.8 ns	-0.155 $\pm$ 0.007	0.6	-0.148 $\pm$ 0.012	0.3	0.007 $\pm$ 0.010	0.7	-0.086$\pm$ 0.013	0.4	$\frac{404.49}{329}$ = 1.23
1.2 ns	-0.154 $\pm$ 0.006	0.4	-0.152 $\pm$ 0.012	0.1	0.011 $\pm$ 0.009	0.2	-0.079$\pm$ 0.013	0.2	$\frac{405.11}{332}$ = 1.22

cut by $\pm$0.2 ns (at 0.8 ns and 1.2 ns), the corresponding Dalitz plot parameters from these sets are given in the Table 5.7. It is found that timing cut does not contribute to systematic error.

5.2.6 cos(θ) in Center of Mass Frame of the η' meson

The analysis used cos(θ) in center of mass frame of the η' from -0.85 rad to 0.85 rad. To calculate the systematic error arising from this variable, the Dalitz plot parameters are calculated for three subranges in which the cos(θ) in center of mass frame of η' varied from -0.8 to 0.8, -0.75 to 0.75, and -0.7 to 0.7 and is given in the Table 5.8, while, all other conditions remain unchanged. The systematic error

Table 5.8: The cos(θ) (in the center of mass frame of the η' meson) window is varied to calculate the systematic error and the corresponding Dalitz plot parameters.

Set	a	Δa	b	Δb	c	Δc	d	Δd	χ^2/**ndf**
Standard	-0.151 $\pm$ 0.007		-0.151 $\pm$ 0.012		0.013 $\pm$ 0.009		-0.081 $\pm$ 0.013		$\frac{385.67}{332}$ = 1.16
$\pm$0.8	-0.153 $\pm$ 0.007	0.3	-0.144 $\pm$ 0.012	0.6	0.020 $\pm$ 0.010	0.8	-0.079 $\pm$ 0.013	0.2	$\frac{380.86}{331}$ = 1.15
$\pm$0.75	-0.149 $\pm$ 0.007	0.3	-0.149 $\pm$ 0.013	0.2	0.026 $\pm$ 0.010	1.4	-0.079 $\pm$ 0.013	0.2	$\frac{362.38}{331}$ = 1.09
$\pm$0.7	-0.153 $\pm$ 0.008	0.3	-0.145 $\pm$ 0.013	0.5	0.026 $\pm$ 0.010	1.4	-0.071 $\pm$ 0.014	0.8	$\frac{366.52}{331}$ = 1.11

contributes asymmetrically to the parameter c only (systematic error of c, $\sigma_c = {}^{+0.013}_{-0.0}$).

5.2.7 M_x(pπ+π-) Selection

The systematic error from the cut on the missing mass of | M_x(pπ+$\pi-$) - 0.547 | less than equal to 0.015 GeV/c^2 is calculated. The cut window is varied by 0.005 GeV/c^2 to the standard selection window in order to calculate systematic error. The parameter values are given in the Table 5.9. The parameters c and d are sensitive to the cut, and the systematic error on the cut is calculated by taking the difference between the standard result and the two results. The systematic error comes out to be asymmetric with a value of $\sigma_c = {}^{+0.007}_{-0.018}$ and $\sigma_d = {}^{+0.014}_{-0.015}$ for parameter c and d respectively.

5.2.8 Systematics Error from Fits to the Signal and the Background

The systematic uncertainty from the polynomial fit to the background and a Voigtian fit to the signal are estimated here. A polynomial fit of second and

Table 5.9: The M_x(pπ+π-) cut window varied to calculate the systematic error and the corresponding Dalitz plot parameters.

Set	a	Δa	b	Δb	c	Δc	d	Δd	χ^2/**ndf**
Standard	-0.151 $\pm$ 0.007		-0.151 $\pm$ 0.012		0.013 $\pm$ 0.009		-0.081 $\pm$ 0.013		$\frac{385.67}{332}$ = 1.16
10 MeV	-0.157 $\pm$ 0.007	0.9	-0.154 $\pm$ 0.013	0.3	-0.005 $\pm$ 0.010	2	-0.095 $\pm$ 0.013	1.1	$\frac{302.06}{329}$ = 0.92
20 MeV	-0.148 $\pm$ 0.007	0.4	-0.147 $\pm$ 0.012	0.3	0.020 $\pm$ 0.010	0.7	-0.066 $\pm$ 0.013	1.2	$\frac{406.77}{331}$ = 1.23

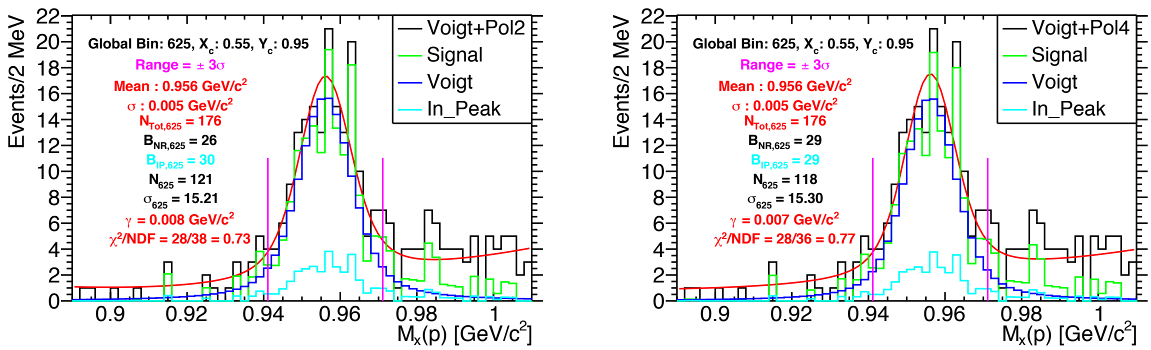

a b

Figure 5.5: The figure (a) M_x(p) distribution of a bin is fitted with a polynomial of second order and figure (b) is the same bin fitted with a polynomial of fourth order in the Dalitz plot.

fourth order is done to the background in the experimental data while keeping all other conditions unchanged. The Fig. 5.5 shows a fit to the background of a low statistics bin with second and fourth order polynomial. The signal is also fitted with a Gaussian function instead of the Voigtian function and the background is fitted with a third order polynomial, keeping all other conditions unchanged and is shown in the Fig. 5.6. The Dalitz plot parameters calculated from different background fits and the signal fit are listed in the Table 5.10. It is found that the fits do not contribute to the systematic error.

Table 5.10: The M_x(pπ+π-) cut window varied to calculate the systematic error and the corresponding Dalitz plot parameters.

Set	a	Δa	b	Δb	c	Δc	d	Δd	χ^2/**ndf**
Standard	-0.151 $\pm$ 0.007		-0.151 $\pm$ 0.012		0.013 $\pm$ 0.009		-0.081 $\pm$ 0.013		$\frac{385.67}{332}$ = 1.16
pol-2	-0.154 $\pm$ 0.007	0.4	-0.146 $\pm$ 0.012	0.4	0.005 $\pm$ 0.009	0.9	-0.090 $\pm$ 0.013	0.7	$\frac{384.15}{332}$ = 1.16
pol-4	-0.151 $\pm$ 0.007	0.0	-0.152 $\pm$ 0.012	0.1	0.008 $\pm$ 0.009	0.6	-0.088 $\pm$ 0.013	0.5	$\frac{395.74}{330}$ = 1.20
Gauss	-0.158 $\pm$ 0.007	1.0	-0.149 $\pm$ 0.013	0.2	0.004 $\pm$ 0.010	1.0	-0.090 $\pm$ 0.013	0.7	$\frac{231.55}{331}$ = 0.70

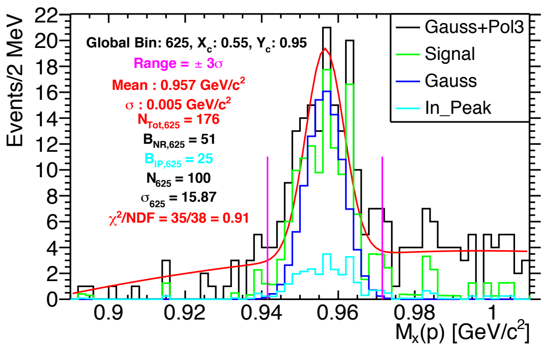

a

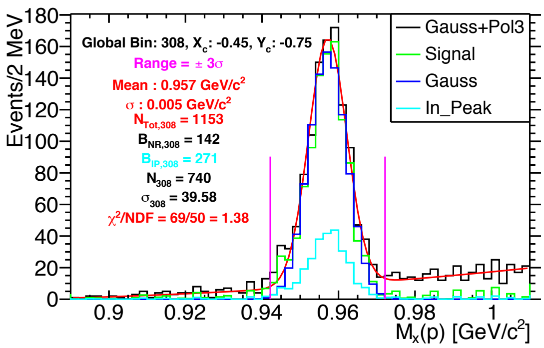

b

Figure 5.6: The figure (a) is the fit to a low statistics bin and the figure (b) is to the highest statistics bin of the M_x(p) distribution in the Dalitz plot, where the signal peak is fitted with a Gaussian function.

5.3 Total Systematics

The systematic error for bin width and CLAS sector is directly calculated from the weighted standard deviation of the different configurations. The possible systematic error from the different cuts are considered only when the Dalitz plot parameters cannot be explained by the statistical error of the standard parameters and it is beyond the understanding. The systematic error arising from different sources are listed in the Table 5.11. The errors obtained from these studies are both symmetric and sometimes asymmetric. The total error on each parameter is obtained by adding the upper and lower bound separately for all the sources in quadrature and then taking their square root as shown below:

$$\sigma_{x_{Total}} = \sqrt{\sigma^2_{x_{source_1}} + \sigma^2_{x_{source_2}} + \sigma^2_{x_{source_3}}} \tag{5.5}$$

where, $\sigma_{x_{Total}}$ stands for the total systematic error on the parameter x. $\sigma_{x_{source_1}}$ stands for the error from source 1. The same calculation is done separately for both the upper and lower bound error to a parameter.

Table 5.11: Systematic errors on the Dalitz plot parameters.

Syst Err.	a	b	c	d
Bin Width	$\pm$ 0.0038	$\pm$ 0.002	$\pm$ 0.0064	$\pm$ 0.0075
Sector	$\pm$ 0.0071	$\pm$ 0.0053	$\pm$ 0.0048	$\pm$ 0.0046
Photon Multiplicity	$^{+0.0}_{-0.009}$	–	–	$^{+0.0}_{-0.015}$
$\cos(\theta)_{cm}$ of η'	–	–	$^{+0.013}_{-0.0}$	–
$M_x(p\pi+\pi-)$	–	–	$^{+0.007}_{-0.018}$	$^{+0.014}_{-0.015}$
Total	$^{+0.0081}_{-0.0121}$	$^{+0.0057}_{-0.0057}$	$^{+0.0167}_{-0.0197}$	$^{+0.0165}_{-0.0230}$

Chapter 6

Results and Outlook

This chapter presents the final Dalitz plot parameters of $\eta' \to \eta\, \pi^+\, \pi^-$ decay using the CLAS *g12* data. The conclusion of the analysis is discussed and it includes comparisons of results to other experiments. In addition to that, an investigation to understand the decay of intermediate σ meson ($\eta' \to \sigma\, \eta$) to π^+ and π^- in the $\eta' \to \eta\, \pi^+\, \pi^-$ decay mode is presented and compared to different theoretical models.

6.1 Final Dalitz plot parameters

The final Dalitz plot parameters of the η' meson through subsequent decay of $\eta' \to \eta\, \pi^+\, \pi^-$ using the CLAS *g12* photoproduction dataset along with the statistical and systematical errors are reported below :

a : -0.151 $\pm$ 0.007 (Stat) $^{+0.008}_{-0.012}$ (Syst)

b : -0.151 $\pm$ 0.012 (Stat) $^{+0.006}_{-0.006}$ (Syst)

c : 0.013 $\pm$ 0.009 (Stat) $^{+0.017}_{-0.020}$ (Syst)

d : -0.081 $\pm$ 0.013 (Stat) $^{+0.017}_{-0.023}$ (Syst)

6.2 Conclusion and Summary

In this study, the decay of $\eta' \to \eta\, \pi^+\, \pi^-$ is studied with a total of 160090 events which survived after all conditions. The statistics reported here is three times higher than the highest statistics reported by BESIII collaboration [29]. The decay of these events are studied with a Dalitz plot and the results from the fit to the Dalitz plot are reported as Dalitz plot parameters. The measurement of the Dalitz plot parameters are dominated by systematic error. The fit to the Dalitz plot yields a reasonable χ^2/ndf of the value 1.16 which shows the quality of the fit is good. However, there is another recent measurement of the Dalitz plot parameters for the $\eta' \rightarrow \eta\ \pi^+\ \pi^-$ decay again by BESIII collaboration [58] which used a total of 351016 events.

The thesis also presents two unbiased methods to calculate the Dalitz plot parameters described in Sec. 4.6. The "Acceptance correction method" does not consider the effects on acceptance from the migration of events from bins during the reconstruction of an event. The "Smearing matrix method" on the other hand presents a way to calculate the acceptances more accurately as it takes care of the migration of the events from nearby bins. The results, however, matches within the statistical errors from both the methods because of the choice of wide binning. The bin width is 3 times the resolution of both Dalitz variable X and Y in both the methods. The choice of the binning is based on the optimization of the total number of events and the resolution of the Dalitz variables. The "Smearing matrix method" being a more realistic approach has been used to present the final Dalitz plot parameters and to perform systematic studies in the analysis.

A comparison of the *g12* Dalitz plot parameters with the other experimental results are shown in the Table 6.1. The parameters a and b from the CLAS *g12* measurement are consistent within 1 standard deviation to results reported by the VES [28] and shows disagreements with the parameters provided by BESIII [29, 58] experiment. The Dalitz parameter c has direct physical significance which indicates C-parity violation in the strong interaction. A value of c closer to zero indicates that the C-parity is conserved in the strong decay of $\eta' \rightarrow \eta\ \pi^+\ \pi^-$. In the measurement, it is found that c parameter is consistent to zero within 1.5 standard deviation. The parameters c and d from the *g12* measurement is consistent with both the VES [28] and the BESIII [29, 58] experiment. The Dalitz plot parameters from $\eta' \rightarrow \eta\ \pi^+\ \pi^-$ decay are also compared to neutral decay mode of η' meson, the $\eta' \rightarrow \eta\ \pi^0\ \pi^0$ decay [58–60], are given in the Table 6.3. In the isospin limit, the two channels are expected to yield the same Dalitz plot parameters. Both, the recent measurements from the A2 Collaboration [60] at MAMI and the BESIII Collaboration [58] have shown agreement among them. However, the recent measurement from the BESIII [58] shows a discrepancy of 2.6 standard deviations for the parameter a in the charged and neutral decay modes of $\eta' \rightarrow \eta\ \pi\ \pi$ decay. The present work, however, seems deviated by 4 standard deviations from the recent results for the Dalitz parameters a and b. Our measurement seems to agree within statistical limits for the parameter d. One of the reasons behind the deviation of most measurements for Dalitz parameters a and b with the CLAS *g12* could be that we could not detect all the final state particles. The reconstruction of the η meson as a missing particle affects the Dalitz variable Y. This is reflected in the Dalitz plot parameters a and b because these parameters are the coefficients of Dalitz variable Y.

A comparison of the *g12* Dalitz plot parameters with the U(3) chiral effective theory is shown in the Table 6.2. The value of b and d from *g12* measurement as well as from the previous measurements largely deviate from zero. However, the framework U(3) chiral unitary approach [24] and U(3) chiral effective field theory in combination with a relativistic coupled-channels approach [30] predicts b and d to be zero. Therefore, the present analysis recommends the theory to include final state interaction corrections in the chiral model for pseudoscalar mesons [24]. The Theory [30]* in the Table 6.2 is resulting from theoretical fits which include VES data. A comparison of these (from theory and experiment) parameters are also shown in Fig. 6.1, where the errors shown are statistical only.

6.2.1 Invariant Mass of $\pi^+\ \pi^-$ Distribution

Apart from the goal of the thesis which is to perform the measurement of the Dalitz plot parameters for the $\eta' \rightarrow \eta\, \pi^+\, \pi^-$ decay, we also studied the scalar intermediate particle arising from the same decay. The η' and η mesons are pseudoscalars and both have an isospin (I) of 0. The isospin I, for both the π^+ and π^- is 1. Due to the conservation of 3^{rd} component of the isospin (I_3), the η' meson can decay into π^+ and π^- through an intermediate scalar meson as shown in the Fig. 6.2. Hence, we looked at the distribution of $\pi^+\ \pi^-$ invariant mass and compared it to the

Table 6.1: Comparison of *g12* Dalitz plot parameters of the $\eta' \to \eta\ \pi^+\ \pi^-$ decay with various experimental results.

Parameter	VES [28]	BESIII (Old) [29]	BESIII (New) [58]	CLAS $g12$
a	-0.127 $\pm$ 0.016 $\pm$ 0.008	-0.047 $\pm$ 0.011 $\pm$ 0.003	-0.056 $\pm$ 0.004 $\pm$ 0.002	-0.151 $\pm$ 0.007 $^{+0.008}_{-0.012}$
b	-0.106 $\pm$ 0.028 $\pm$ 0.014	-0.069 $\pm$ 0.019 $\pm$ 0.009	-0.049 $\pm$ 0.006 $\pm$ 0.006	-0.151 $\pm$ 0.012 $^{+0.006}_{-0.006}$
c	0.015 $\pm$ 0.011 $\pm$ 0.014	0.019 $\pm$ 0.011 $\pm$ 0.003	0.0027 $\pm$ 0.0024 $\pm$ 0.0018	0.013 $\pm$ 0.009 $^{+0.017}_{-0.020}$
d	-0.082 $\pm$ 0.017 $\pm$ 0.008	-0.073 $\pm$ 0.012 $\pm$ 0.003	-0.063 $\pm$ 0.004 $\pm$ 0.003	-0.081 $\pm$ 0.013 $^{+0.017}_{-0.023}$
χ^2/**ndf**	1.13	1.05	...	1.16

theoretical distributions which consider intermediate states of the decays [61, 62]. A good sensitivity to the parameters of the σ (slightly f_0) meson decay to the $\pi^+\ \pi^-$ in the $\eta' \to \eta\ \pi^+\ \pi^-$ decay is observed and shown in the Fig. 6.3. The figure also shows a comparison of the Nonlinear Sigma Model (NLSM) [13, 63] and Generalized Linear Sigma Model (GLSM) [63, 64]. The NLSM is shown with and without the contribution from σ meson. The inclusion of σ meson to NLSM changes the centeredness of M($\pi+\ \pi-$) from center to right. The right-centeredness of the distribution with the acceptance corrected invariant mass of the $\pi^+\ \pi^-$ mesons (M($\pi+\ \pi-$)) from CLAS *g12* data and NLSM thus indicates a clear presence of σ meson [13, 65–67].

Table 6.2: Comparison of *g12* Dalitz plot parameters of the $\eta' \to \eta\ \pi^+\ \pi^-$ decay with various theoretical predictions.

Parameter	Theory [24]	Theory [30]	Theory [30]*	**CLAS** *g12*
a	-0.093	-0.116 $\pm$ 0.024	-0.116 $\pm$ 0.011	-0.151 $\pm$ 0.007 $^{+0.008}_{-0.012}$
b	-0.059	0.0 $\pm$ 0.019	-0.042 $\pm$ 0.034	-0.151 $\pm$ 0.012 $^{+0.006}_{-0.006}$
c				0.013 $\pm$ 0.009 $^{+0.017}_{-0.020}$
d	-0.003	0.016 $\pm$ 0.035	0.010 $\pm$ 0.019	-0.081 $\pm$ 0.013 $^{+0.017}_{-0.023}$
χ^2/**ndf**				1.16

Table 6.3: Comparison of *g12* Dalitz plot parameters of the $\eta' \to \eta\ \pi^+\ \pi^-$ decay with various experimental results of the $\eta' \to \eta\ \pi^0\ \pi^0$ decay.

Parameter	GAMS 4π [59]	A2 Col. [60]	BESIII [58]	**CLAS** $g12$
a	-0.066 $\pm$ 0.016 $\pm$ 0.003	-0.074 $\pm$ 0.008 $\pm$ 0.006	-0.087 $\pm$ 0.009 $\pm$ 0.006	-0.151 $\pm$ 0.007 $^{+0.008}_{-0.012}$
b	-0.063 $\pm$ 0.028 $\pm$ 0.004	-0.063 $\pm$ 0.014 $\pm$ 0.005	-0.073 $\pm$ 0.014 $\pm$ 0.005	-0.151 $\pm$ 0.012 $^{+0.006}_{-0.006}$
c	-0.107 $\pm$ 0.096 $\pm$ 0.003	...	...	0.013 $\pm$ 0.009 $^{+0.017}_{-0.020}$
d	0.018 $\pm$ 0.078 $\pm$ 0.006	-0.050 $\pm$ 0.009 $\pm$ 0.005	-0.074 $\pm$ 0.009 $\pm$ 0.004	-0.081 $\pm$ 0.013 $^{+0.017}_{-0.023}$
χ^2/**ndf**	0.93	1.09	...	1.16

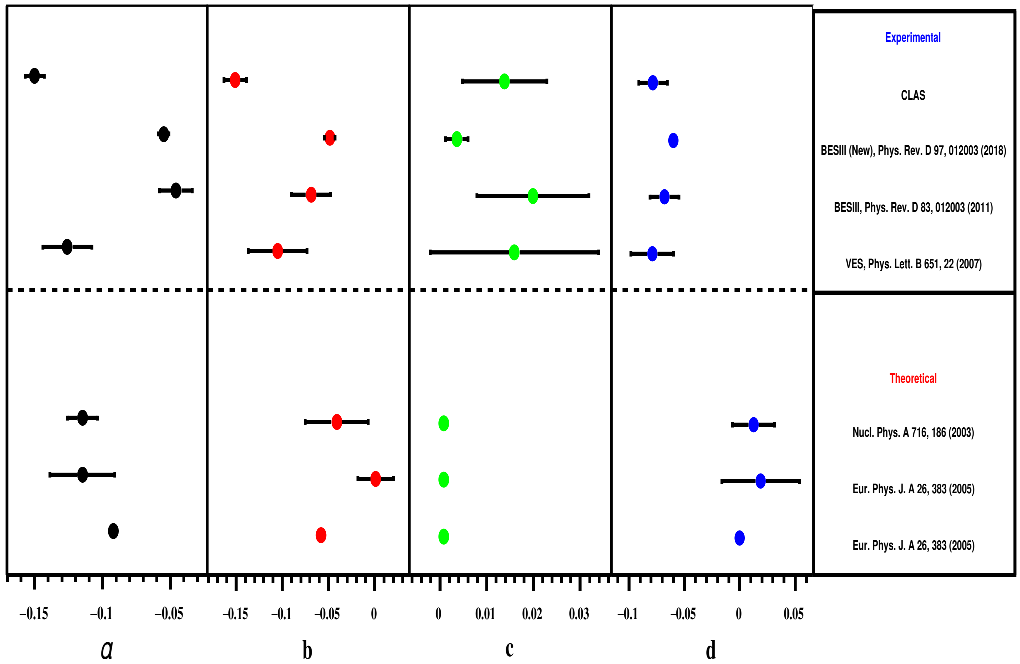

Figure 6.1: Comparison of different experimental (with stat errors) and theoretical measurements for Dalitz plot parameters of $\eta' \to \eta\ \pi^+\ \pi^-$ decay.

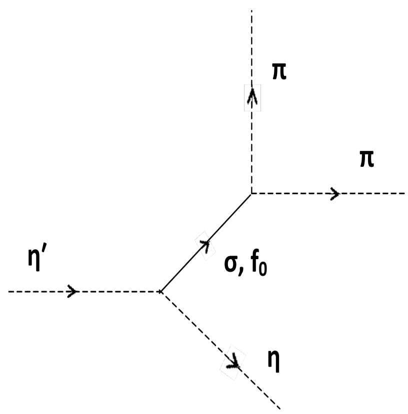

Figure 6.2: Feynman diagram showing the decay of a scalar meson to $\pi^+\ \pi^-$ for the $\eta' \to \eta\ \pi\ \pi$ decay channel.

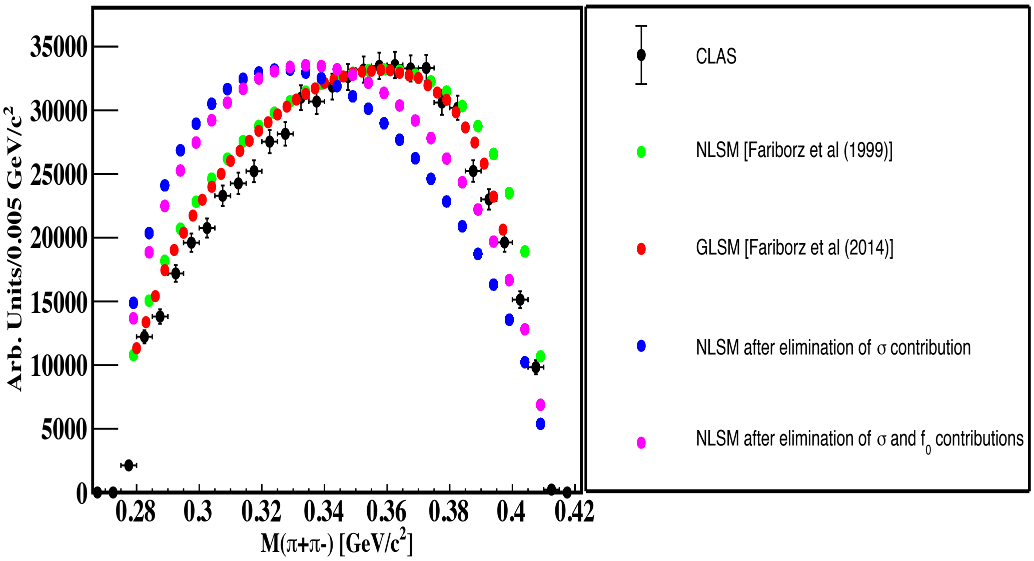

Figure 6.3: The M($\pi+\pi-$) distribution from CLAS *g12* data is compared to the NLSM and GLSM.

6.3 Outlook

In this thesis, the experimental results of Dalitz plot analysis of the decay $\eta' \to \eta$ $\pi^+ \pi^-$ are presented. This analysis is based on the CLAS *g12* data collected during photoproduction experiment γ p $\to \eta'$ p for the center-of-mass energy from 1.9 to 2.76 GeV at JLab. The analysis is based on the highest statistics data collected for this channel in comparison to the other experiments reported so far, except for the most recent BESIII measurement [58]. The CEBAF has been recently upgraded to 12 GeV [68], along with CLAS detector, which is expected to produce more high-quality data. These new experimental data will further improve the measurement of Dalitz plot parameters with higher accuracies. In addition to that, the signature of σ meson evidences for this channel will encourage the scientific society to gain more insight about the meson.

Bibliography

[1] Wilczek F. (2000), QCD made simple, Phys. Today, doi:10.1063/1.1310117

[2] Beisert N., Borasoy B. (2002), The eta-prime $\rightarrow$ eta pi pi decay in U(3) chiral perturbation theory, Nucl. Phys. A **705**, 433

[3] Gresham M. (2002), Preliminary Study of $D^0 \rightarrow K\pi\pi^0$ Decays with Dalitz Plots, SLAC-PUB-9401

[4] http://physics.tutorcircle.com/modern-physics/elementary-particles.html, Accessed June 2017

[5] David Griffiths, (2008) Introduction to Elementary Particles, second ed. WILEY-VCH Verlag GmbH & Co. KGaA, Page: 55 (ISBN-10: 0-471-60386-4)

[6] https://home.cern/about/physics/standard-model, Accessed June 2017

[7] The Nobel Prize in Physics 2004 (2004), Nobelprize.org

[8] https://www.physics.umd.edu/courses/Phys741/xji/chapter1.pdf. Accessed 9 May 2018

[9] Bethke S. (2000), Determination of the QCD Coupling α_s, J. Phys. G 26 , R27

[10] Petri T. (2010) Anomalous decays of pseudoscalar mesons, PhD Dissertation, University of Bonn

[11] https://commons.wikimedia.org/wiki/Particle_physics Accessed July 2017

[12] Particle Data Group, http://pdglive.lbl.gov. Accessed June 2017

[13] Fariborz, A. H. *et al.* (1999), $\eta' \to \eta\pi\pi$ decay as a probe of a possible lowest-lying scalar nonet, Phys. Rev. D 60, 034002

[14] VORGELEGT VON KONSTANTIN OTTNAD (2013) Properties of pseudoscalar flavor singlet mesons from lattice QCD, PhD Dissertation, WILHELMS UNIVERSITAT BONN

[15] Scherer S., (2002) Introduction to Chiral Perturbation Theory, arXiv:hep-ph/0210398

[16] Ecker G., (1995) CHIRAL PERTURBATION THEORY, arXiv:hep-ph/9501357

[17] Naito K. , Oka M. , Takizawa M. , Umekawa T. (2003), U(A)(1) breaking effects on the light scalar meson spectrum, Prog. Theor. Phys. **109**, 969

[18] Weinberg S. (1975), The U(1) Problem, Phys. Rev. D **11**, 3583

[19] R. Escribano, P. Masjuan and J. J. Sanz-Cillero (2011), "Chiral dynamics predictions for $\eta\prime \to \eta\pi\pi$", JHEP **1105**, 094

[20] Bressani T., Filippi A., Wiedner U., (2005) Hadron Physics, STM Publishing House Impacting the World of Science Books & Journals, (ISBN: 978-1-58603-526-7)

[21] Akhoury R., Leurer M. (1989), Low energy effective Lagrangian description of η and η' decays,Z. Phys. C **43**, 145-148

[22] Groom D. E. *et al.* [Particle Data Group] (2000), Review of particle physics. Particle Data Group, Eur. Phys. J. C **15**, 1

[23] Wuethrich A (2005) Dalitz Plots and Hadron Spectroscopy, Master's thesis, University of Bern

[24] Beisert N., Borasoy B. (2003), Hadronic decays of η and η' with coupled channels, Nucl. Phys. A **716**, 186

[25] Bass S. D. (2002), Gluonic effects in η and η' physics, Phys. Scripta T **99**, 96

[26] Bijnens J. (2006), Decays of η and η' and what can we learn from them?, acta physica slovaca vol. 56 No. 3, 305

[27] Bijnens J. (2007), eta and eta-prime physics, eConf C **070910**, 104

[28] Dorofeev V. *et al.* (2007), Study of $\eta' \to \eta\pi{+}\pi-$ Dalitz plot, Phys. Lett. B **651**, 22

[29] Ablikim M. *et al.* [BESIII Collaboration] (2011), Measurement of the matrix element for the decay $\eta' \to \eta\pi^+\pi^-$, Phys. Rev. D **83**, 012003

[30] Borasoy B., Nissler R. (2005), Hadronic eta and eta-prime decays, Eur. Phys. J. A **26**, 383

[31] Jefferson Lab, https://www.flickr.com/photos/ Accessed June 2017

[32] Jefferson Lab, The JLab Picture Exchange, http://www1.jlab.org/ul/jpix/ Accessed June 2017

[33] Sober D.I. *et al.* (2000), The bremsstrahlung tagged photon beam in Hall B at JLab, Nuclear Instruments and Methods in Physics Research Section A: Accelerators, Spectrometers, Detectors and Associated Equipment, Volume 440, Issue 2

[34] Mecking B.A. *et al.* (2003), The CEBAF large acceptance spectrometer (CLAS),Nuclear Instruments and Methods in Physics Research Section A: Accelerators, Spectrometers, Detectors and Associated Equipment, Volume 503, Issue 3

[35] Gohn W. *et al.* [CLAS Collaboration] (2014), Beam-spin asymmetries from semi-inclusive pion electroproduction, Phys. Rev. D **89**, no. 7, 072011

[36] *g12* Target, https://userweb.jlab.org/c̃hristo/g11a%20target.html Accessed June 2017

[37] Sharabian Y.G. *et al.* (2006), A new highly segmented start counter for the CLAS detector, Nuclear Instruments and Methods in Physics Research Section A Accelerators Spectrometers Detectors and Associated Equipment, Volume 556, Issue 1, 246-258

[38] Akbar Z. *et al.* (2016), *g12* Analysis Procedures, Statistics and Systematics. Technical report, CLAS Technical Note

[39] *G*12 _procedures_working_version.pdf, https://clasweb.jlab.org/rungroups/g12/wiki/index.php/Main_Page Accessed June 2017

[40] Brun R., Rademakers F., (1997) ROOT - An Object Oriented Data Analysis Framework, Proceedings AIHENP'96 Workshop, Lausanne, Sep. 1996, Nucl. Inst. & Meth. in Phys. Res. A 389 81

[41] Froehlich I., Cazon .L, Galatyuk T., Hejny V. *et al.*, (2007) Pluto: A Monte Carlo Simulation Tool for Hadronic Physics. PoS, ACAT2007:076

[42] Kunkel M. C. (2014) Photoproduction of π^0 on hydrogen with CLAS from 1.1 GeV - 5.45 GeV using e^+e^- decay, PhD Dissertation, Old Dominion University

[43] Williams M. *et al.* [CLAS Collaboration] (2009), Differential cross sections for the reactions γ p $\rightarrow$ p η and γ p $\rightarrow$ p η', Phys. Rev. C **80**, 045213

[44] Durham Database, http://durpdg.dur.ac.uk/ Accessed July 2017

[45] Bethe-Bloch equation, http://www.med.harvard.edu/jpnm/physics/nmltd/radprin/sect7/7.1/7_1.2.html Accessed July 2017

[46] Pasyuk E., (2007) Energy loss corrections for charged particles in CLAS, CLAS-NOTE 2007-016

[47] https://jlabsvn.jlab.org/svnroot/clas/users/mkunkel/clas/g12_corrections/All_Corrections Accessed August 2017

[48] http://hadron.physics.fsu.edu/ãlghoul/kinfit_note.pdf Accessed August 2017

[49] Dustin K., (2010) Techniques in Kinematic Fitting, CLAS-NOTE 2010-015

[50] Williams M. (2007) Measurement of Differential Cross Sections and Spin Density Matrix Elements along with a Partial Wave Analysis for γ p $\rightarrow$ p ω using CLAS at Jefferson Lab, PhD Dissertation, Carnegie Mellon University

[51] https://wiki.jlab.org/lmd/index.php/Main_Page (The plot of all 337 bins are available here $\rightarrow$) (Documents/Documents supporting the Dalitz plot of $\eta' \rightarrow \eta\ \pi^+\ \pi^-$ analysis note). Accessed August 2017

[52] Sowa C. (2016) Study of Excited η Mesons in Photoproduction at CLAS, PhD Dissertation, RUHR-UNIVERSITÄT BOCHUM

[53] Balkesthl L. C. (2016) Measurement of the Dalitz Plot Distribution for $\eta \rightarrow \pi^+\ \pi^-\ \pi^0$ with KLOE, PhD Dissertation, Uppsala University

[54] Adlarson P. (2012) Studies of the Decay $\eta \rightarrow \pi^+\ \pi^-\ \pi^0$ with WASA-at-COSY, PhD Dissertation, Uppsala University

[55] Paterno M., (2003) Calculating Efficiencies and Their Uncertainties, FNAL/CD/CEPA/SLD

[56] Cowan G., (2008) Error analysis for efficiency, RHUL Physics

[57] Barlow R., (2002) Systematic errors: Facts and fictions, Conference on Advanced Statistical Techniques in Particle Physics, Durham, England, 18-22, proc. ed. by Whalley, M.R., Lyons, L., Institute For Particle Physics Phenomenology, Durham, UK.

[58] Ablikim M.*et al.* (2018) [BESIII Collaboration], "Measurement of the matrix elements for the decays $\eta' \rightarrow \eta\pi^+\pi^-$ and $\eta' \rightarrow \eta\pi^0\pi^0$", Phys. Rev. D 97, 012003

[59] Blik . .*et al.* (2008) [GAMS-4π Collaboration], "Measurement of the Matrix Element for the Decay $\eta' \rightarrow \eta\pi 0\pi 0$ with the GAMS-4π Spectrometer", Physics of Atomic Nuclei, Vol. 72, Issue 2, 231236

[60] Adlarson P.*et al.* (2018) [A2 Collaboration], "Measurement of the decay $\eta' \rightarrow \pi 0\pi 0\eta$ at MAMI", Phys. Rev. D 98, 012001

[61] Borasoy B., Nissler R. (2007), eta, eta-prime $\rightarrow$ pi+ pi- l+ l- in a chiral unitary approach, Eur. Phys. J. A **33**, 95

[62] Amelino-Camelia G. *et al.*, (2010) Physics with the KLOE-2 experiment at the upgraded DAϕNE, arXiv:1003.3868

[63] "private communication with A. Fariborz" on October 2016

[64] Fariborz, A. H. *et al.* (2014), Chiral nonet mixing in $\eta' \to \eta\pi\pi$ decay, Phys. Rev. D 90, 033009

[65] Fariborz A. H., Schechter J. (2003), Effects of light scalar mesons in $\eta \to 3\pi$ decay, Phys. Rev. D 67, 054001

[66] Fariborz A.H. (2006), Phys. Rev. D 74, 054030

[67] Fariborz A.H. (2004), Int. J. Mod. Phys. A 19, 2095

[68] Lung A. (2012) 12 GeV CEBAF Upgrade, http://www.ciae.ac.cn/eng/hadron2012/program/Jefferson%20Laboratory %2012GeV%20CEBAF%20Upgrade.pdf Accessed November 2016

Appendix A

List of runs included in the analysis

The list of all the "good" runs recorded by the *g12* experiment is given in"G12_procedures_working_version.pdf" along with all intricate triggers used and other details. The file can be accessed at url:

https://clasweb.jlab.org/rungroups/g12/wiki/images/f/f0
G12_procedures_working_version.pdf [38].

All the corrections used in the data and simulations have been agreed upon by the *g12* collaboration and used in the analysis unanimously. The run numbers specifically used are listed in Table below.

Run Number	Run Number	Run Number	Run Number
56363-56363	56791-56794	56489-56490	56958-56958
56365-56365	56798-56802	56499-56499	56960-56975
56369-56369	56804-56815	56501-56506	56977-56983
56384-56384	56821-56827	56508-56510	56985-56986
56386-56386	56831-56835	56513-56517	56989-56989
56401-56401	56838-56839	56519-56542	56992-56994
56403-56406	56841-56845	56544-56550	56996-57006
56408-56408	56849-56849	56555-56556	57008-57017
56410-56410	56853-56862	56559-56559	57021-57023
56420-56422	56864-56866	56561-56564	57025-57027
56435-56436	56869-56870	56573-56583	57030-57032
56441-56443	56874-56875	56585-56593	57036-57039
56445-56450	56877-56877	56605-56605	57061-57069
56453-56462	56879-56879	56608-56612	57071-57073
56465-56465	56897-56908	56614-56628	57075-57080
56467-56472	56910-56919	56630-56644	57094-57097
56476-56476	56921-56930	56646-56646	57100-57103
56478-56483	56932-56940	56653-56656	57106-57108
56485-56487	56948-56956	56660-56661	57114-57152

Run Number	Run Number
56664-56670	57155-57156
56673-56675	57159-57168
56679-56681	57170-57185
56683-56683	57189-57229
56685-56697	57233-57239
56700-56708	57249-57253
56710-56744	57255-57258
56747-56772	57260-57268
56774-56778	57270-57288
56780-56784	57290-57291
56787-56788	57293-57312

Appendix B

Data points

All the information required to obtain the Dalitz plot parameters for the acceptance correction method are listed here. Starting from global bin no. i, its central co-ordinates of Dalitz plot variables X_i and Y_i, the number of events and error in the bin N_i, σ_i respectively before and after $N_{Cor,i}$, $\sigma_{Cor,i}$ acceptance correction and the acceptance ϵ_i of the bin. One can also use the data to obtain Dalitz plot parameters using the smearing matrix method. The required smearing matrix from simulation will be made available on request to the email: sghosh@jlab.org.

(i)	X_i	Y_i	N_i	σ_i	$\epsilon_i * 10^{-2}$	$N_{Cor,i}$	$\sigma_{Cor,i}$
77	-1.25	-1.25	432.44	26.90	2.76	16143.32	966.64
78	-1.25	-1.25	402.20	24.98	2.78	14438.25	897.51
79	-1.25	-1.25	427.79	27.28	2.85	14935.04	957.92
104	-1.15	-1.15	552.96	30.87	3.09	18231.36	994.42
105	-1.15	-1.15	513.00	31.48	3.00	17182.81	1047.82
106	-1.15	-1.15	525.11	29.98	2.98	17695.56	1004.28
107	-1.15	-1.15	502.87	28.86	2.94	16957.68	983.12
108	-1.15	-1.15	520.46	30.72	2.98	17583.87	1030.40
109	-1.15	-1.15	401.91	25.30	2.98	13520.68	849.16
110	-1.15	-1.15	439.70	27.10	3.00	14592.95	905.06
111	-1.15	-1.15	463.94	28.60	3.07	15029.95	933.70
133	-1.05	-1.05	589.61	32.22	3.22	18472.04	996.38
134	-1.05	-1.05	575.63	31.05	3.27	17723.50	948.32
135	-1.05	-1.05	529.44	30.24	3.16	16700.49	957.49
136	-1.05	-1.05	545.76	31.28	3.12	17577.34	1003.09
137	-1.05	-1.05	575.92	31.21	3.20	18179.49	973.19
138	-1.05	-1.05	532.99	31.86	3.16	16763.69	1009.32
139	-1.05	-1.05	518.06	29.83	3.16	16507.37	942.91
140	-1.05	-1.05	495.73	28.74	3.10	15827.14	928.33
141	-1.05	-1.05	502.01	29.26	3.12	15814.34	941.83
142	-1.05	-1.05	427.86	26.16	3.26	13039.89	802.83
161	-0.95	-0.95	620.26	33.28	3.51	17912.61	942.98
162	-0.95	-0.95	640.00	33.59	3.44	18675.25	976.42
163	-0.95	-0.95	608.61	33.10	3.35	18488.21	984.81
164	-0.95	-0.95	601.07	31.57	3.28	18199.81	964.81
165	-0.95	-0.95	595.61	33.17	3.23	18548.79	1025.79
166	-0.95	-0.95	556.78	32.08	3.25	17039.75	988.36
167	-0.95	-0.95	476.39	28.91	3.27	14687.54	881.90
168	-0.95	-0.95	521.37	31.54	3.28	16118.37	958.64
169	-0.95	-0.95	562.24	31.56	3.28	16959.48	965.15
170	-0.95	-0.95	468.91	28.02	3.30	14213.64	849.11
171	-0.95	-0.95	485.45	28.15	3.27	14717.63	863.60
172	-0.95	-0.95	448.09	26.72	3.30	13384.36	813.98
173	-0.95	-0.95	424.82	26.63	3.40	12377.41	785.89
190	-0.85	-0.85	633.26	34.62	3.66	17585.49	942.63
191	-0.85	-0.85	713.22	35.68	3.53	20097.84	1010.63
192	-0.85	-0.85	632.28	34.43	3.50	18660.61	974.58
193	-0.85	-0.85	615.44	33.65	3.44	18237.68	974.94
194	-0.85	-0.85	584.05	32.43	3.30	17604.12	984.80
195	-0.85	-0.85	595.25	32.57	3.37	17881.02	964.66

(i)	X_i	Y_i	N_i	σ_i	$\epsilon_i * 10^{-2}$	$N_{Cor,i}$	$\sigma_{Cor,i}$
196	-0.85	-0.85	566.57	30.52	3.36	16818.48	909.13
197	-0.85	-0.85	516.16	30.66	3.39	15200.64	906.16
198	-0.85	-0.85	551.94	32.13	3.26	17028.28	984.84
199	-0.85	-0.85	479.60	28.96	3.36	14274.29	863.13
200	-0.85	-0.85	539.76	29.40	3.29	16090.05	899.85
201	-0.85	-0.85	510.99	29.75	3.36	15200.07	884.26
202	-0.85	-0.85	463.98	27.89	3.31	13860.24	845.86
203	-0.85	-0.85	465.54	27.47	3.32	13754.76	831.90
204	-0.85	-0.85	349.03	24.88	3.40	10101.61	734.68
219	-0.75	-0.75	673.90	36.39	3.81	17897.17	952.35
220	-0.75	-0.75	679.53	35.59	3.64	18509.10	980.21
221	-0.75	-0.75	628.79	34.43	3.56	17591.14	967.74
222	-0.75	-0.75	638.48	35.01	3.42	18776.31	1020.29
223	-0.75	-0.75	576.77	32.64	3.44	17185.95	940.96
224	-0.75	-0.75	635.08	34.97	3.38	19195.66	1028.55
225	-0.75	-0.75	580.13	31.33	3.37	17210.97	930.41
226	-0.75	-0.75	578.92	31.86	3.33	17484.60	956.08
227	-0.75	-0.75	615.77	33.83	3.37	18578.88	999.45
228	-0.75	-0.75	648.59	33.13	3.38	19135.58	981.60
229	-0.75	-0.75	520.98	30.05	3.39	15251.46	888.80
230	-0.75	-0.75	534.89	30.81	3.36	15774.11	918.24
231	-0.75	-0.75	512.92	29.00	3.40	15003.57	855.90
232	-0.75	-0.75	533.42	30.67	3.38	15730.80	906.54
233	-0.75	-0.75	447.56	26.77	3.44	12780.26	781.59
234	-0.75	-0.75	443.76	26.87	3.39	12950.01	795.92
249	-0.65	-0.65	713.27	37.27	3.73	19383.22	996.11
250	-0.65	-0.65	727.90	37.10	3.66	19993.96	1012.70
251	-0.65	-0.65	597.78	33.83	3.55	16981.31	950.16
252	-0.65	-0.65	628.45	34.69	3.46	18525.98	997.22
253	-0.65	-0.65	665.40	34.42	3.39	19811.08	1011.26
254	-0.65	-0.65	607.49	33.59	3.35	18167.59	1001.44
255	-0.65	-0.65	660.38	34.46	3.28	19841.57	1055.47
256	-0.65	-0.65	584.00	32.06	3.27	17686.19	983.31
257	-0.65	-0.65	596.63	33.34	3.33	18126.07	997.28
258	-0.65	-0.65	639.49	34.59	3.33	19139.05	1041.41
259	-0.65	-0.65	654.73	34.49	3.39	19386.14	1017.35
260	-0.65	-0.65	533.07	30.45	3.42	15678.03	888.43
261	-0.65	-0.65	591.21	31.95	3.42	17241.63	935.45
262	-0.65	-0.65	527.75	30.50	3.39	15341.37	904.16
263	-0.65	-0.65	443.93	27.02	3.45	12854.79	782.53

(i)	X_i	Y_i	N_i	σ_i	$\epsilon_i * 10^{-2}$	$N_{Cor,i}$	$\sigma_{Cor,i}$
264	-0.65	-0.65	432.90	27.11	3.40	12712.50	796.48
265	-0.65	-0.65	405.90	25.65	3.38	11709.71	766.02
278	-0.55	-0.55	698.56	36.24	3.81	18547.01	949.70
279	-0.55	-0.55	675.76	35.36	3.72	18429.02	947.96
280	-0.55	-0.55	646.55	37.65	3.57	18255.34	1053.39
281	-0.55	-0.55	675.19	36.51	3.47	19822.82	1047.65
282	-0.55	-0.55	615.32	33.89	3.41	17891.36	995.08
283	-0.55	-0.55	620.41	33.67	3.34	18672.56	1008.48
284	-0.55	-0.55	639.63	35.11	3.29	19712.73	1064.66
285	-0.55	-0.55	602.36	33.58	3.26	18902.97	1023.76
286	-0.55	-0.55	570.30	32.24	3.30	17299.68	976.29
287	-0.55	-0.55	569.53	35.02	3.35	17127.65	1042.48
288	-0.55	-0.55	638.95	33.54	3.35	19210.88	999.05
289	-0.55	-0.55	581.55	31.15	3.40	16992.38	916.84
290	-0.55	-0.55	577.25	33.39	3.36	17212.77	991.44
291	-0.55	-0.55	501.63	28.85	3.29	15083.60	881.26
292	-0.55	-0.55	538.70	30.62	3.33	16216.55	918.56
293	-0.55	-0.55	527.47	31.02	3.34	15746.94	928.19
294	-0.55	-0.55	440.99	29.31	3.33	13209.44	879.31
295	-0.55	-0.55	456.66	29.79	3.31	13718.36	901.69
308	-0.45	-0.45	753.70	38.21	3.71	20344.22	1028.48
309	-0.45	-0.45	693.55	37.26	3.69	18974.13	1009.03
310	-0.45	-0.45	680.42	36.68	3.52	19652.28	1037.23
311	-0.45	-0.45	619.70	33.97	3.42	18135.59	991.83
312	-0.45	-0.45	683.01	36.95	3.34	20751.20	1101.17
313	-0.45	-0.45	625.69	33.29	3.30	18899.47	1008.17
314	-0.45	-0.45	603.31	32.93	3.23	18696.60	1020.46
315	-0.45	-0.45	544.49	31.68	3.27	16768.24	966.27
316	-0.45	-0.45	647.35	35.65	3.26	20076.65	1090.25
317	-0.45	-0.45	611.53	34.12	3.25	18719.66	1049.96
318	-0.45	-0.45	612.76	32.52	3.24	18572.84	1007.53
319	-0.45	-0.45	591.91	32.50	3.23	18114.17	1010.73
320	-0.45	-0.45	518.67	29.96	3.35	15356.45	897.46
321	-0.45	-0.45	556.14	33.31	3.36	16633.48	990.01
322	-0.45	-0.45	517.42	29.57	3.32	15681.95	888.77
323	-0.45	-0.45	518.29	29.18	3.26	15770.14	898.27
324	-0.45	-0.45	484.30	29.12	3.30	14561.60	885.66
325	-0.45	-0.45	401.82	25.97	3.24	12267.61	804.34
337	-0.35	-0.35	723.51	36.45	3.75	19323.00	971.57
338	-0.35	-0.35	734.38	37.41	3.67	20125.21	1018.44

(i)	X_i	Y_i	N_i	σ_i	$\epsilon_i * 10^{-2}$	$N_{Cor,i}$	$\sigma_{Cor,i}$
339	-0.35	-0.35	701.56	36.94	3.54	19627.12	1045.01
340	-0.35	-0.35	595.67	36.61	3.42	18077.56	1061.77
341	-0.35	-0.35	656.41	36.11	3.33	19929.69	1081.76
342	-0.35	-0.35	639.34	35.31	3.29	19491.08	1071.63
343	-0.35	-0.35	546.96	32.08	3.20	17119.24	1001.38
344	-0.35	-0.35	643.72	34.00	3.17	20342.24	1071.84
345	-0.35	-0.35	672.21	35.07	3.16	21271.49	1110.04
346	-0.35	-0.35	550.01	32.89	3.18	17217.35	1033.97
347	-0.35	-0.35	508.11	30.49	3.22	15947.56	942.97
348	-0.35	-0.35	550.94	31.39	3.20	17057.74	982.36
349	-0.35	-0.35	545.80	33.74	3.22	16778.23	1051.42
350	-0.35	-0.35	587.41	32.41	3.16	18322.37	1028.43
351	-0.35	-0.35	558.10	31.87	3.20	17190.99	1001.25
352	-0.35	-0.35	513.55	29.74	3.22	15866.28	926.23
353	-0.35	-0.35	492.47	29.52	3.10	15486.88	960.80
354	-0.35	-0.35	440.23	27.16	3.16	13748.63	863.02
355	-0.35	-0.35	387.80	26.87	3.06	12475.25	883.37
356	-0.35	-0.35	386.57	26.07	3.08	12356.06	850.51
367	-0.25	-0.25	726.96	36.57	3.60	20349.97	1012.06
368	-0.25	-0.25	736.26	37.84	3.54	21052.76	1067.05
369	-0.25	-0.25	636.52	35.09	3.38	18620.93	1041.77
370	-0.25	-0.25	616.28	34.69	3.32	18679.48	1042.42
371	-0.25	-0.25	616.43	34.72	3.29	18811.41	1056.16
372	-0.25	-0.25	648.18	35.27	3.19	20269.07	1104.58
373	-0.25	-0.25	626.94	33.93	3.14	19830.86	1081.73
374	-0.25	-0.25	589.91	33.47	3.11	19255.52	1072.07
375	-0.25	-0.25	515.50	31.63	3.10	16927.68	1016.68
376	-0.25	-0.25	554.41	33.76	3.05	18283.52	1107.15
377	-0.25	-0.25	530.71	30.78	3.07	17393.03	1002.28
378	-0.25	-0.25	566.67	33.10	3.10	18173.36	1069.31
379	-0.25	-0.25	582.83	33.42	3.08	18806.13	1088.02
380	-0.25	-0.25	549.79	31.82	3.14	17474.16	1013.51
381	-0.25	-0.25	488.00	29.53	3.07	15945.73	959.04
382	-0.25	-0.25	547.29	32.01	3.10	17456.04	1035.29
383	-0.25	-0.25	497.83	29.60	3.08	16117.51	961.77
384	-0.25	-0.25	428.12	27.05	3.02	13815.49	901.62
385	-0.25	-0.25	391.46	25.47	2.93	13128.21	874.69
386	-0.25	-0.25	428.40	26.90	2.85	14669.31	949.13
397	-0.15	-0.15	741.83	36.55	3.52	21098.13	1038.46
398	-0.15	-0.15	708.59	37.25	3.41	20837.32	1091.82

(i)	X_i	Y_i	N_i	σ_i	$\epsilon_i * 10^{-2}$	$N_{Cor,i}$	$\sigma_{Cor,i}$
399	-0.15	-0.15	634.31	35.86	3.36	19116.15	1062.91
400	-0.15	-0.15	601.74	35.44	3.24	18793.71	1090.92
401	-0.15	-0.15	592.02	33.88	3.12	19144.74	1082.80
402	-0.15	-0.15	592.31	35.88	3.11	19180.69	1149.97
403	-0.15	-0.15	581.01	32.76	2.92	19747.73	1123.42
404	-0.15	-0.15	603.37	33.62	2.95	20043.65	1144.55
405	-0.15	-0.15	510.48	31.30	2.97	17340.05	1053.58
406	-0.15	-0.15	548.71	31.61	2.99	18331.15	1056.96
407	-0.15	-0.15	548.74	33.37	3.00	18320.64	1111.91
408	-0.15	-0.15	588.57	33.37	2.98	19891.38	1117.97
409	-0.15	-0.15	517.02	31.45	2.98	17059.72	1061.38
410	-0.15	-0.15	455.73	28.11	2.99	15317.99	939.48
411	-0.15	-0.15	509.56	29.67	2.98	17002.31	998.64
412	-0.15	-0.15	466.68	28.31	2.98	15623.68	948.81
413	-0.15	-0.15	464.58	28.24	2.89	15755.52	983.87
414	-0.15	-0.15	397.28	27.94	2.81	14002.75	995.94
415	-0.15	-0.15	407.37	25.74	2.78	14364.13	930.64
416	-0.15	-0.15	333.22	24.14	2.70	12030.52	902.59
427	-0.05	-0.05	711.11	36.34	3.45	20996.89	1049.76
428	-0.05	-0.05	662.04	36.22	3.35	19832.78	1079.65
429	-0.05	-0.05	580.18	34.35	3.24	17987.08	1059.04
430	-0.05	-0.05	520.64	32.91	3.17	16736.05	1033.38
431	-0.05	-0.05	530.67	31.80	3.04	17377.42	1046.53
432	-0.05	-0.05	556.59	32.46	2.89	18993.74	1127.51
433	-0.05	-0.05	537.02	33.87	2.92	19024.99	1150.13
434	-0.05	-0.05	520.79	30.55	2.81	18514.55	1087.02
435	-0.05	-0.05	580.24	33.10	2.85	20336.97	1163.49
436	-0.05	-0.05	523.87	30.33	2.80	18621.93	1085.70
437	-0.05	-0.05	463.26	29.24	2.86	16128.67	1024.53
438	-0.05	-0.05	545.58	32.78	2.81	19658.36	1164.48
439	-0.05	-0.05	484.94	29.82	2.84	17240.11	1048.56
440	-0.05	-0.05	533.27	29.95	2.86	18473.85	1049.85
441	-0.05	-0.05	529.54	30.70	2.76	18684.90	1119.60
442	-0.05	-0.05	479.55	28.78	2.76	17112.12	1047.27
443	-0.05	-0.05	409.00	27.26	2.78	14634.02	984.04
444	-0.05	-0.05	348.50	24.11	2.59	13195.74	934.43
445	-0.05	-0.05	366.25	25.61	2.60	13955.74	986.57
446	-0.05	-0.05	315.35	24.39	2.53	12401.39	967.30
457	0.05	0.05	610.09	33.73	3.27	18702.48	1030.96
458	0.05	0.05	630.27	34.08	3.12	19737.56	1098.49

(i)	X_i	Y_i	N_i	σ_i	$\epsilon_i * 10^{-2}$	$N_{Cor,i}$	$\sigma_{Cor,i}$
459	0.05	0.05	568.45	32.89	3.10	18357.18	1058.55
460	0.05	0.05	538.16	33.13	2.90	18735.30	1138.97
461	0.05	0.05	541.30	31.79	2.88	18755.74	1104.23
462	0.05	0.05	572.60	33.10	2.81	20761.83	1172.95
463	0.05	0.05	576.28	32.31	2.71	21512.83	1189.50
464	0.05	0.05	515.28	30.21	2.69	19057.62	1122.84
465	0.05	0.05	495.89	30.20	2.72	18168.56	1113.20
466	0.05	0.05	450.26	30.56	2.62	17107.44	1168.82
467	0.05	0.05	508.81	30.87	2.65	19304.15	1161.00
468	0.05	0.05	455.33	29.68	2.69	17111.69	1099.05
469	0.05	0.05	509.11	31.26	2.65	19163.79	1181.03
470	0.05	0.05	466.01	29.12	2.63	17349.98	1113.80
471	0.05	0.05	432.60	27.77	2.64	16494.55	1048.51
472	0.05	0.05	444.20	29.15	2.56	16867.47	1144.83
473	0.05	0.05	392.76	26.06	2.51	15679.75	1038.08
474	0.05	0.05	319.02	23.30	2.44	13020.01	956.58
475	0.05	0.05	364.78	25.16	2.39	14903.76	1059.40
476	0.05	0.05	325.04	23.73	2.30	13796.38	1041.31
487	0.15	0.15	553.20	32.07	3.09	18056.30	1036.38
488	0.15	0.15	624.57	34.20	3.00	20900.62	1136.49
489	0.15	0.15	573.68	35.08	2.92	20323.92	1189.23
490	0.15	0.15	506.88	31.89	2.79	17896.09	1145.00
491	0.15	0.15	529.98	31.84	2.74	19014.97	1165.78
492	0.15	0.15	506.58	30.81	2.62	19506.67	1175.51
493	0.15	0.15	477.85	29.67	2.58	18761.67	1146.77
494	0.15	0.15	446.33	28.73	2.56	17436.53	1122.45
495	0.15	0.15	461.87	29.70	2.52	18197.39	1183.19
496	0.15	0.15	448.80	28.87	2.48	18123.92	1163.81
497	0.15	0.15	447.49	28.89	2.47	18135.15	1171.09
498	0.15	0.15	472.14	29.53	2.49	19098.36	1183.98
499	0.15	0.15	429.48	26.58	2.48	16927.16	1076.85
500	0.15	0.15	446.85	28.13	2.46	18088.06	1147.05
501	0.15	0.15	411.07	27.04	2.42	16875.97	1118.79
502	0.15	0.15	377.62	24.42	2.34	15796.99	1049.51
503	0.15	0.15	335.06	25.79	2.30	14700.38	1120.13
504	0.15	0.15	319.81	22.72	2.18	14370.00	1047.29
505	0.15	0.15	273.50	22.68	2.09	12763.56	1092.48
506	0.15	0.15	226.92	20.67	2.11	10536.22	986.12
517	0.25	0.25	539.27	31.06	2.90	18668.62	1069.85
518	0.25	0.25	551.48	31.85	2.75	19871.82	1162.98

(i)	X_i	Y_i	N_i	σ_i	$\epsilon_i * 10^{-2}$	$N_{Cor,i}$	$\sigma_{Cor,i}$
519	0.25	0.25	510.44	31.90	2.72	18725.38	1172.99
520	0.25	0.25	480.02	30.13	2.63	18390.91	1145.77
521	0.25	0.25	496.93	31.92	2.49	20120.33	1281.16
522	0.25	0.25	439.71	28.50	2.43	18059.90	1174.67
523	0.25	0.25	480.78	29.82	2.40	20047.62	1240.72
524	0.25	0.25	480.17	31.08	2.31	21178.07	1339.99
525	0.25	0.25	420.69	27.48	2.33	18235.77	1173.50
526	0.25	0.25	419.92	26.98	2.29	18153.03	1180.50
527	0.25	0.25	383.33	27.58	2.28	16761.51	1207.36
528	0.25	0.25	387.64	25.70	2.27	17165.33	1132.37
529	0.25	0.25	409.47	28.57	2.24	18141.20	1277.52
530	0.25	0.25	407.72	27.97	2.22	18130.72	1260.96
531	0.25	0.25	356.08	24.37	2.16	16406.87	1132.83
532	0.25	0.25	366.28	25.53	2.10	16915.10	1226.73
533	0.25	0.25	303.66	22.94	1.96	15073.23	1177.14
534	0.25	0.25	301.71	21.59	1.90	15520.10	1143.88
535	0.25	0.25	249.89	20.93	1.81	13526.71	1159.03
536	0.25	0.25	222.89	19.62	1.75	12376.21	1130.44
547	0.35	0.35	527.74	30.89	2.70	19735.98	1140.25
548	0.35	0.35	490.56	31.96	2.60	19025.84	1227.05
549	0.35	0.35	536.46	32.40	2.51	21570.21	1286.95
550	0.35	0.35	454.32	29.66	2.39	18927.57	1244.58
551	0.35	0.35	484.85	31.39	2.30	21549.85	1354.96
552	0.35	0.35	376.34	26.41	2.23	16912.18	1183.07
553	0.35	0.35	429.75	28.50	2.15	19911.67	1329.80
554	0.35	0.35	383.77	26.23	2.10	18073.30	1253.40
555	0.35	0.35	379.38	27.98	2.09	18179.74	1334.84
556	0.35	0.35	361.19	25.31	2.10	17457.34	1203.44
557	0.35	0.35	463.86	28.15	2.06	22346.91	1373.20
558	0.35	0.35	351.73	25.50	2.00	17414.88	1278.15
559	0.35	0.35	320.21	22.80	1.95	16271.73	1176.30
560	0.35	0.35	290.94	25.59	1.93	15087.33	1321.85
561	0.35	0.35	282.83	22.43	1.88	14761.27	1199.41
562	0.35	0.35	329.77	24.21	1.80	18499.77	1339.39
563	0.35	0.35	238.22	20.29	1.68	14121.57	1206.64
564	0.35	0.35	271.58	21.83	1.61	16780.55	1363.13
565	0.35	0.35	223.96	19.90	1.56	14177.60	1284.95
566	0.35	0.35	202.57	17.98	1.50	13297.17	1209.45
578	0.45	0.45	441.45	29.57	2.34	18698.63	1265.84
579	0.45	0.45	426.52	28.77	2.25	19411.87	1272.36

(i)	X_i	Y_i	N_i	σ_i	$\epsilon_i * 10^{-2}$	$N_{Cor,i}$	$\sigma_{Cor,i}$
580	0.45	0.45	397.32	26.81	2.14	18021.72	1262.18
581	0.45	0.45	400.81	27.15	2.11	18999.18	1287.81
582	0.45	0.45	357.50	26.09	2.01	17869.14	1293.16
583	0.45	0.45	396.88	26.78	1.90	20751.74	1413.83
584	0.45	0.45	429.90	28.39	1.89	23021.95	1497.86
585	0.45	0.45	349.77	26.16	1.83	19626.27	1421.45
586	0.45	0.45	306.44	25.29	1.81	16866.66	1398.95
587	0.45	0.45	319.04	25.40	1.75	18195.69	1452.76
588	0.45	0.45	317.56	24.67	1.75	18325.62	1404.54
589	0.45	0.45	284.88	23.48	1.73	16796.47	1353.91
590	0.45	0.45	283.61	21.96	1.69	16626.84	1306.32
591	0.45	0.45	253.41	21.79	1.59	16106.97	1370.60
592	0.45	0.45	248.34	21.39	1.48	16361.30	1458.79
593	0.45	0.45	236.37	19.38	1.45	16417.10	1335.26
594	0.45	0.45	180.13	18.54	1.33	13214.16	1400.14
595	0.45	0.45	154.00	17.03	1.22	12353.40	1404.21
608	0.55	0.55	406.73	28.45	2.12	19438.69	1339.51
609	0.55	0.55	387.44	28.40	2.00	19664.93	1412.32
610	0.55	0.55	345.60	26.88	1.91	18299.65	1403.89
611	0.55	0.55	376.74	26.44	1.83	20312.77	1446.41
612	0.55	0.55	297.05	23.34	1.73	17749.70	1336.79
613	0.55	0.55	316.21	24.94	1.67	19126.76	1486.49
614	0.55	0.55	300.42	24.53	1.64	18632.00	1494.71
615	0.55	0.55	277.52	22.64	1.58	17369.54	1439.67
616	0.55	0.55	246.50	21.71	1.50	16601.02	1441.18
617	0.55	0.55	272.82	23.26	1.52	18070.98	1533.28
618	0.55	0.55	304.56	23.10	1.46	20576.00	1582.27
619	0.55	0.55	275.29	21.65	1.40	19635.23	1548.18
620	0.55	0.55	221.26	20.37	1.35	15847.67	1515.54
621	0.55	0.55	221.77	19.86	1.29	17099.67	1540.90
622	0.55	0.55	164.52	17.13	1.17	13951.58	1469.34
623	0.55	0.55	164.50	17.93	1.12	14796.61	1602.43
624	0.55	0.55	137.70	15.57	1.02	13195.67	1533.31
625	0.55	0.55	118.01	15.30	0.96	12156.86	1597.87
639	0.65	0.65	343.88	25.22	1.76	19472.79	1437.73
640	0.65	0.65	330.47	24.57	1.65	19825.13	1491.49
641	0.65	0.65	273.90	22.54	1.54	17948.97	1454.86
642	0.65	0.65	268.33	23.36	1.49	18368.06	1556.13
643	0.65	0.65	320.32	23.99	1.42	22706.02	1681.54
644	0.65	0.65	254.02	22.80	1.36	18634.62	1682.29

(i)	X_i	Y_i	N_i	σ_i	$\epsilon_i * 10^{-2}$	$N_{Cor,i}$	$\sigma_{Cor,i}$
645	0.65	0.65	215.22	19.51	1.31	16526.82	1488.00
646	0.65	0.65	230.75	20.72	1.30	17690.53	1597.36
647	0.65	0.65	248.30	21.95	1.22	20821.43	1791.39
648	0.65	0.65	210.64	19.93	1.16	18073.66	1711.63
649	0.65	0.65	185.07	18.25	1.08	16828.86	1697.08
650	0.65	0.65	164.42	16.42	1.06	15411.13	1546.86
651	0.65	0.65	203.33	17.74	1.00	20478.13	1765.99
652	0.65	0.65	155.28	15.52	0.93	16668.46	1663.48
654	0.65	0.65	117.30	13.29	0.80	14567.32	1670.01
669	0.75	0.75	251.45	20.70	1.45	17392.24	1421.70
670	0.75	0.75	263.88	22.76	1.35	19562.36	1684.53
671	0.75	0.75	223.76	21.41	1.28	17421.42	1667.30
672	0.75	0.75	258.12	22.09	1.22	21478.57	1807.91
673	0.75	0.75	261.90	21.50	1.18	22301.68	1828.16
674	0.75	0.75	185.70	18.23	1.13	16776.61	1612.48
700	0.85	0.85	209.50	19.25	1.07	19738.40	1800.41
701	0.85	0.85	184.73	17.47	1.01	17923.94	1738.85

Appendix C

Plots of individual bins in the Dalitz plot

The 337 fitted Dalitz plot bins are made available in ascending global bin number. All the relevant information in the plot are also given in Appendix B in tabular form.

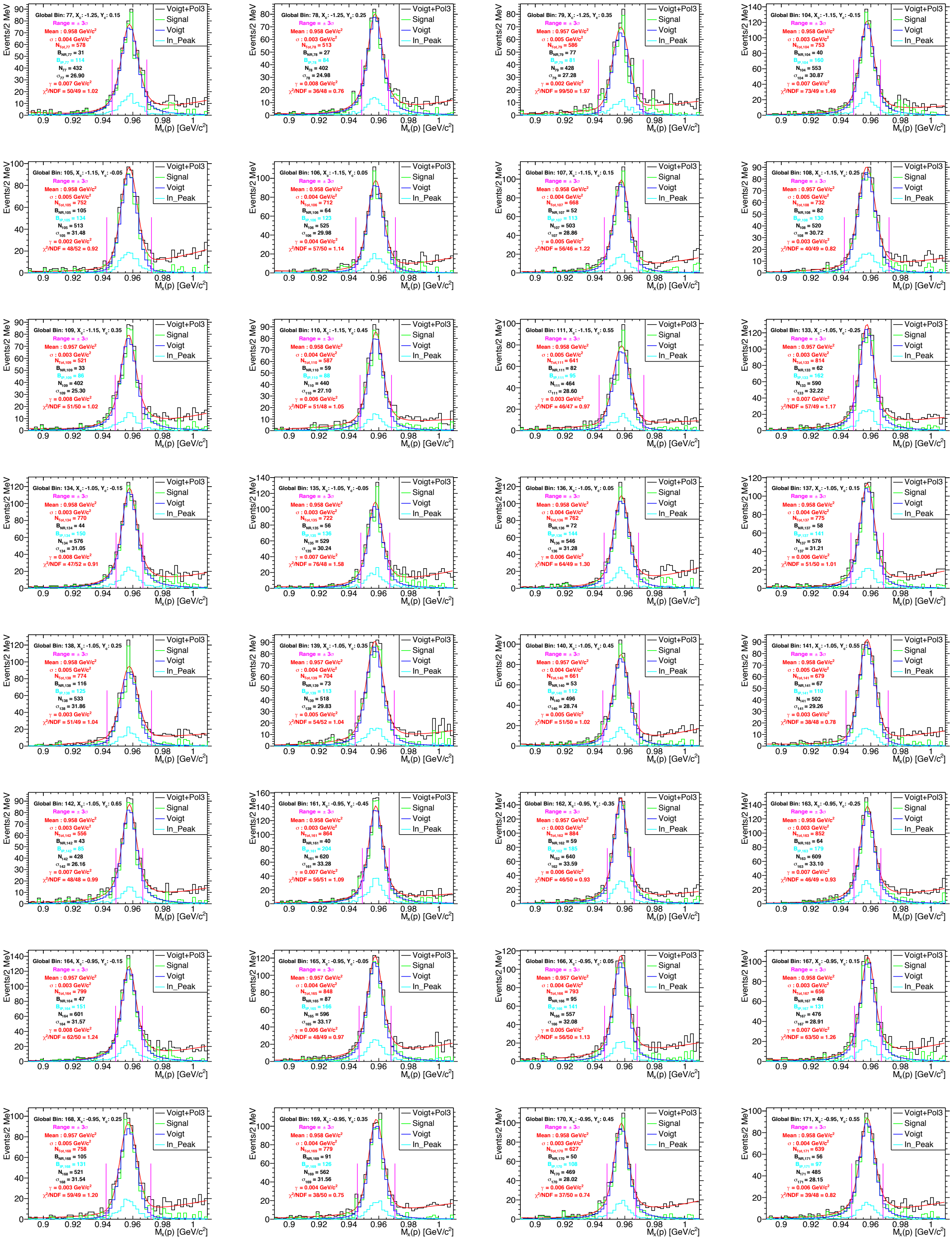

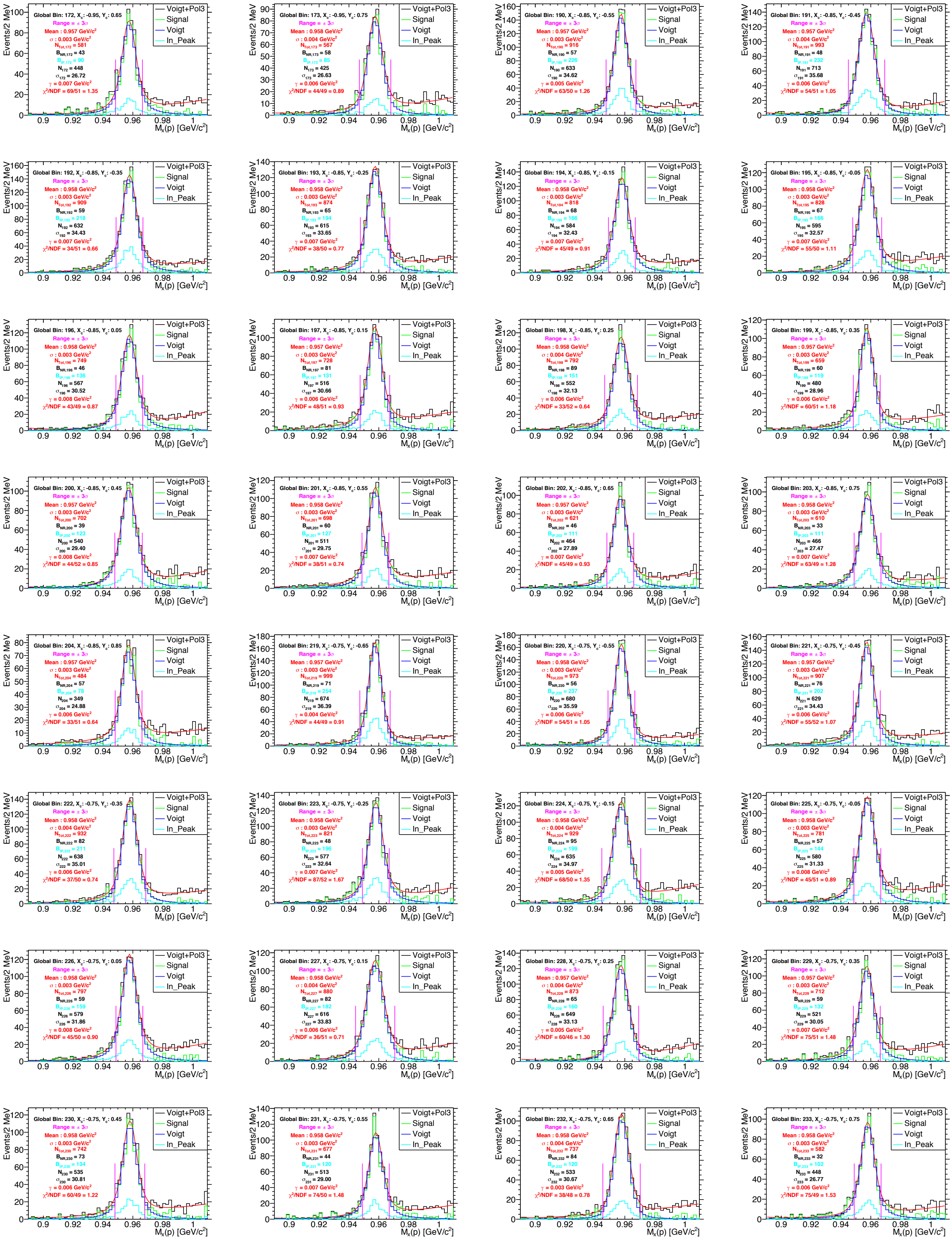

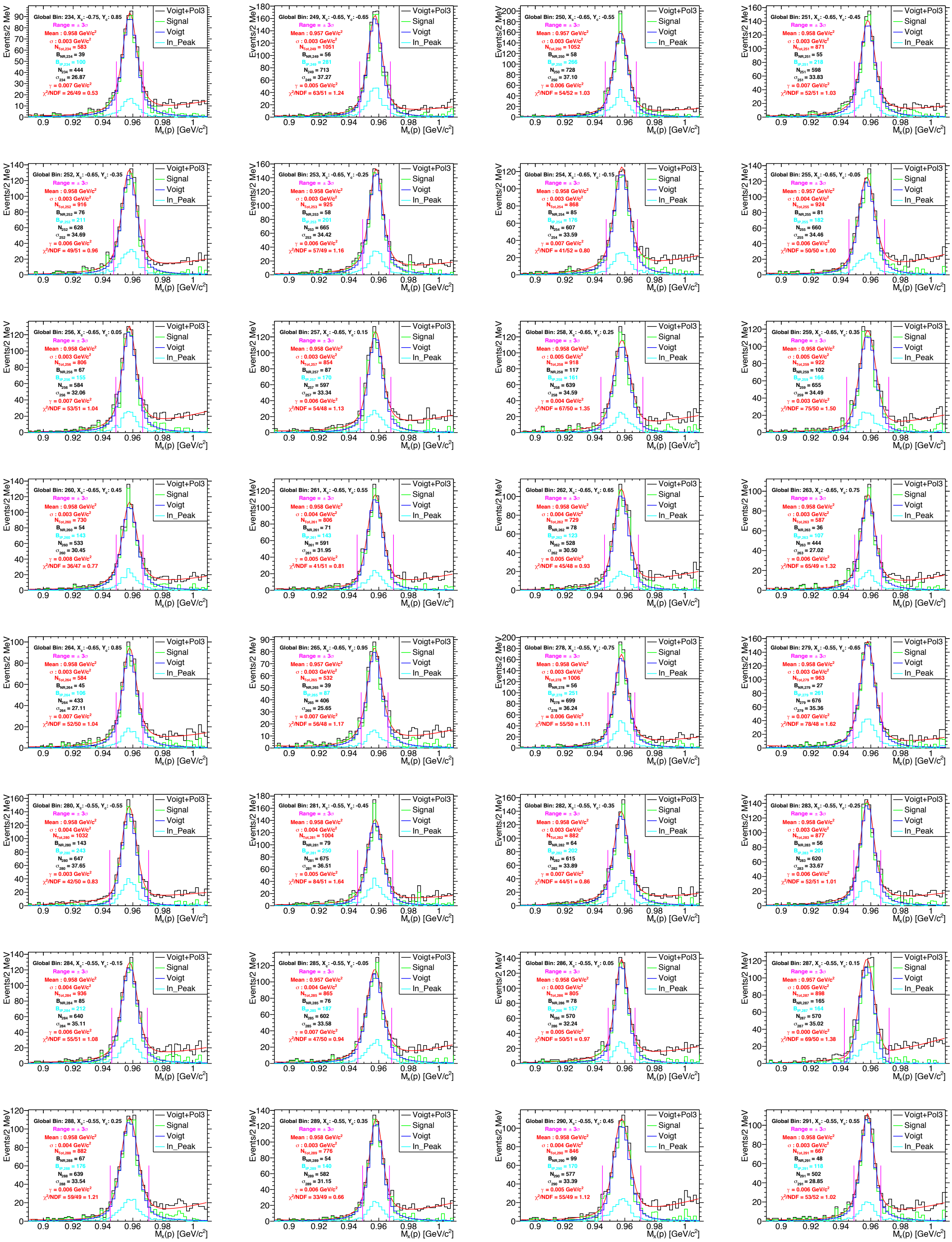
Voigt+Pol3
Signal
Voigt
In_Peak
Events/2 MeV
M_x(p) [GeV/c^2]

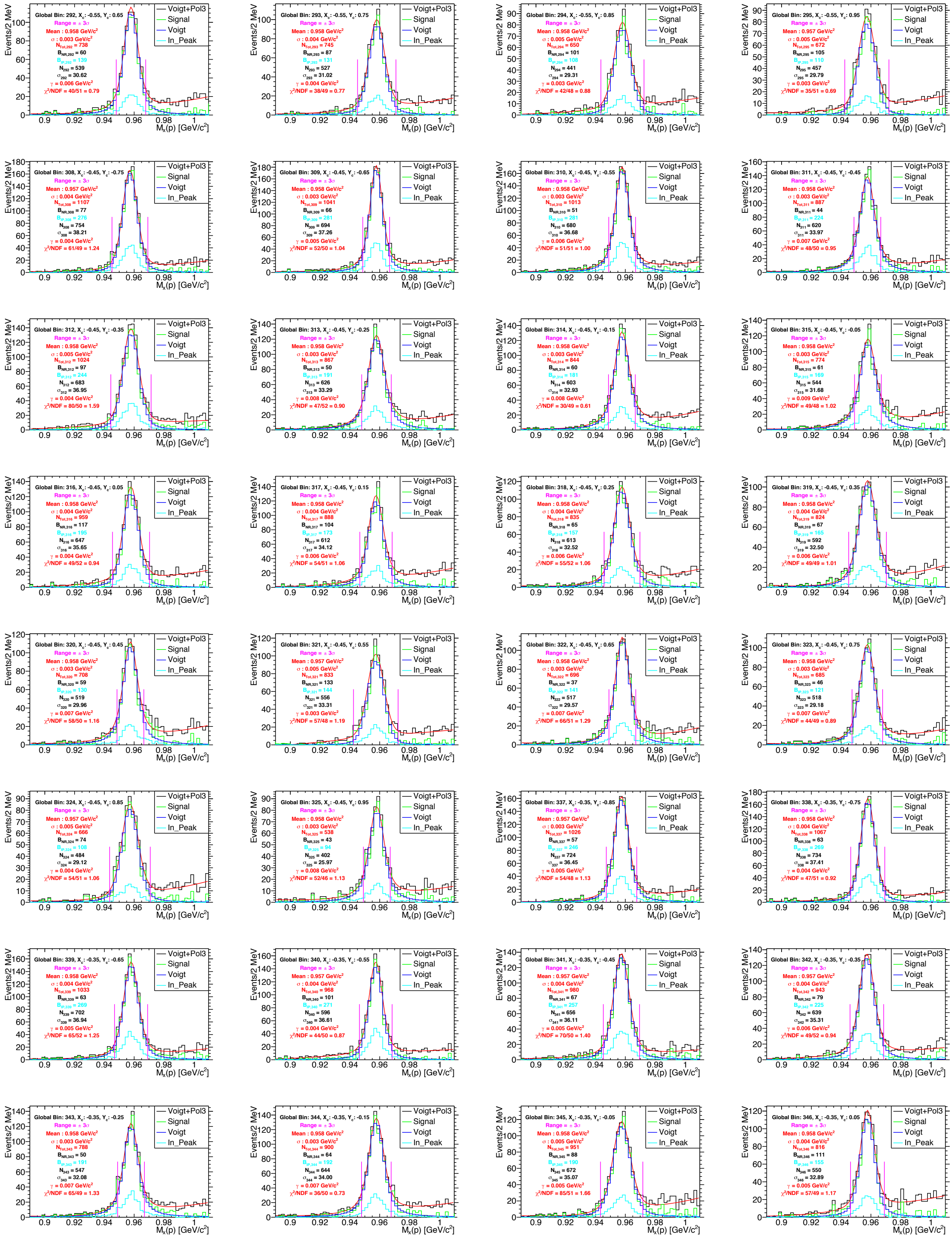

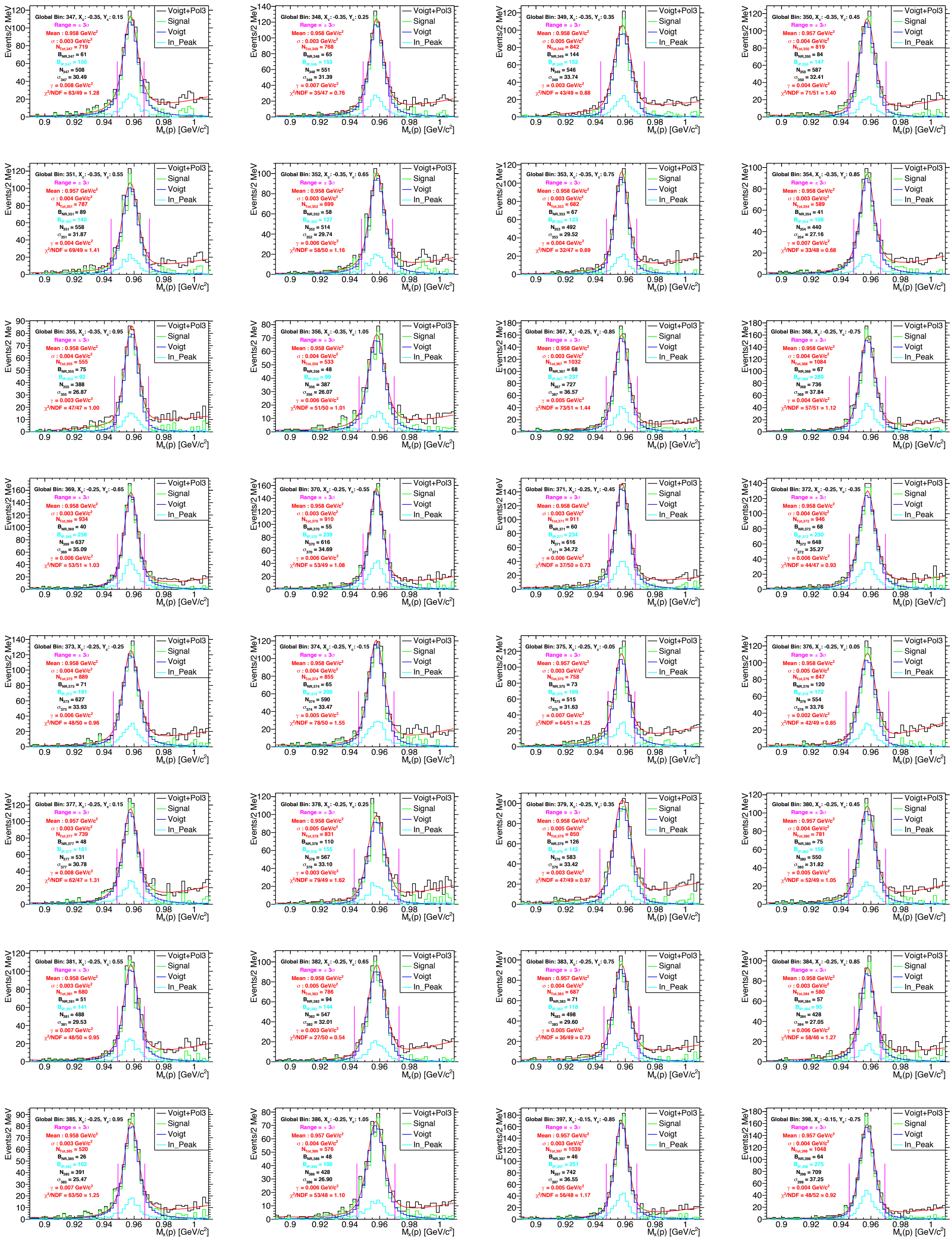
Voigt+Pol3
Signal
Voigt
In_Peak
Events/2 MeV
Mx(p) [GeV/c²]

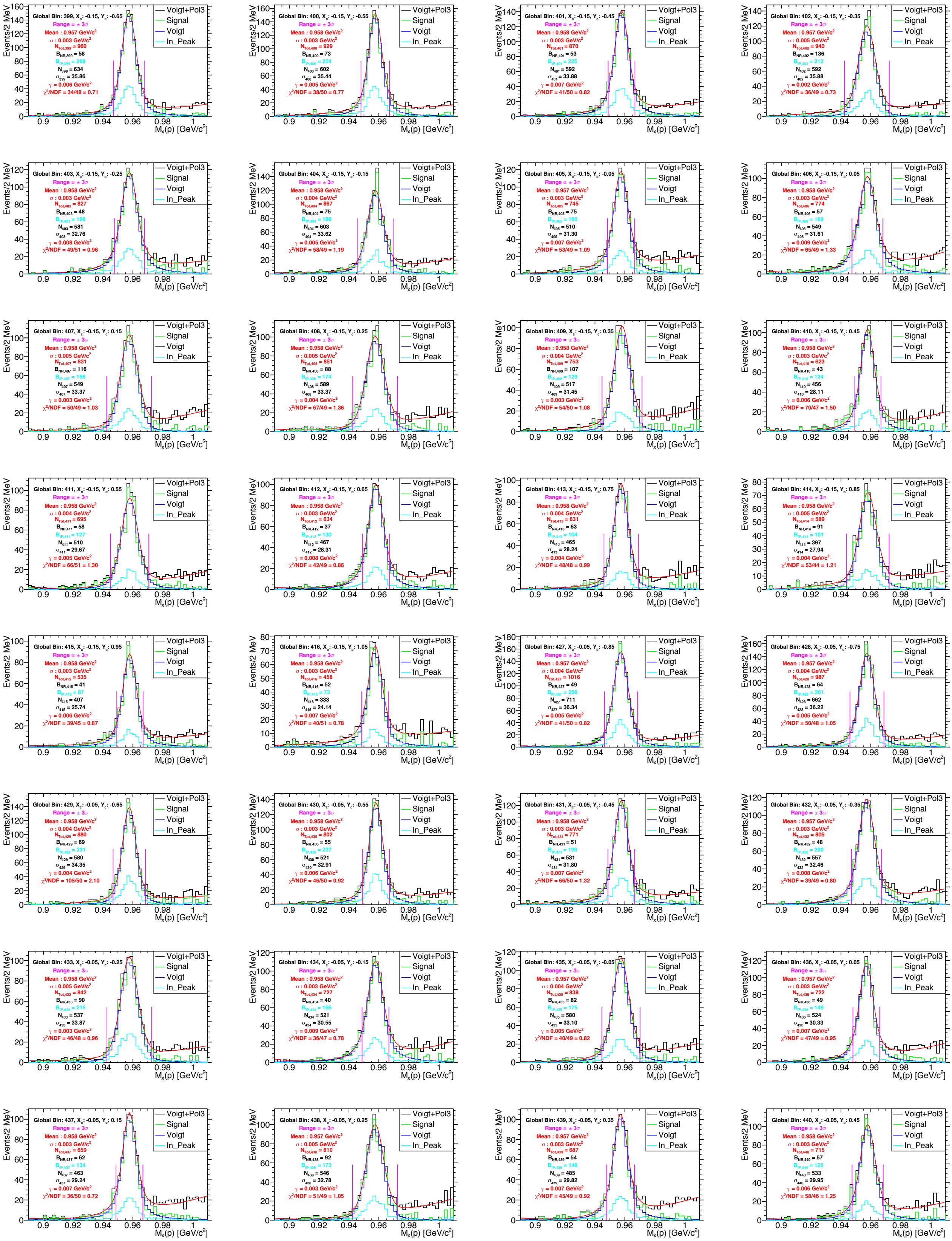

Voigt+Pol3
Signal
Voigt
In_Peak
Events/2 MeV
$M_x(p)$ [GeV/c^2]

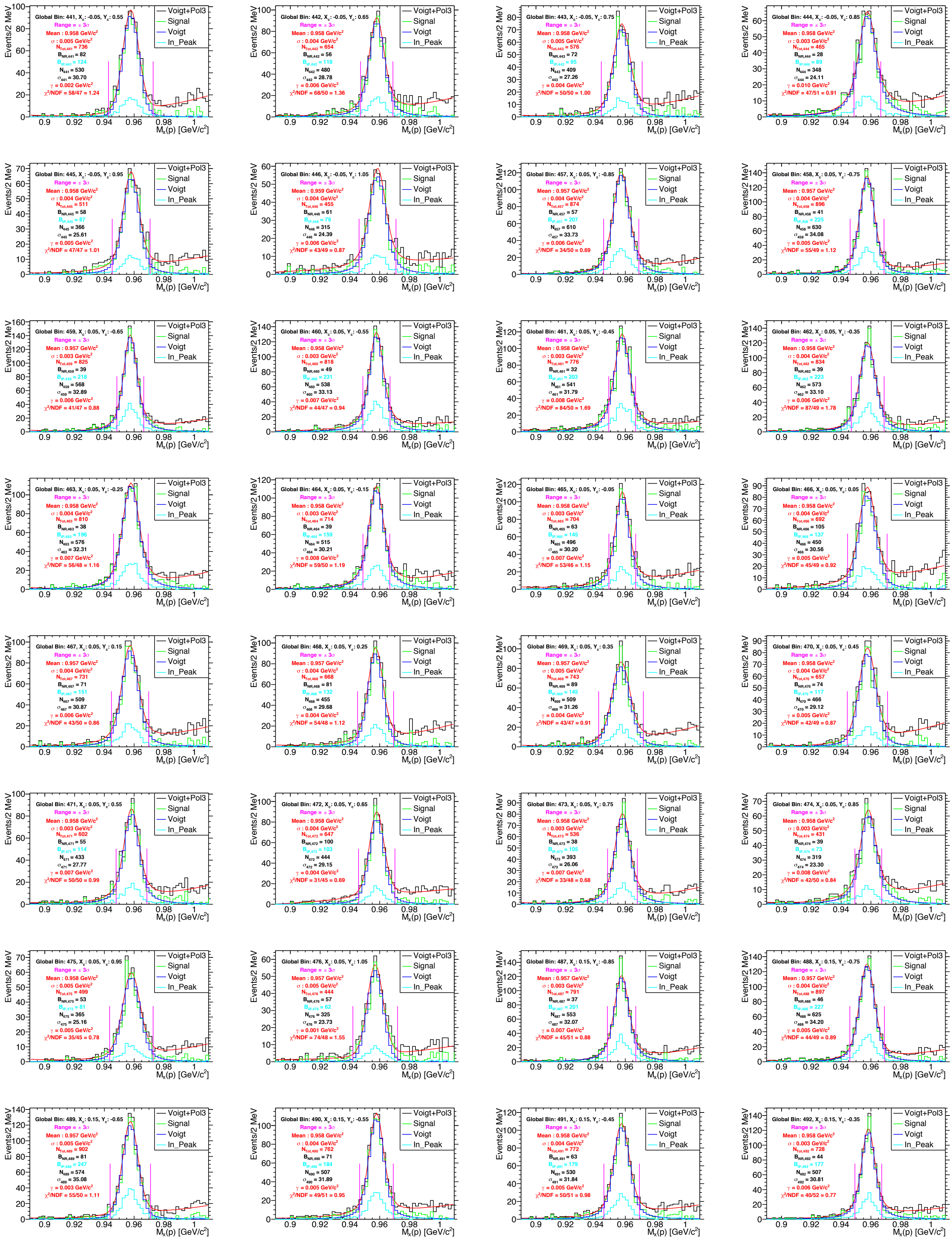

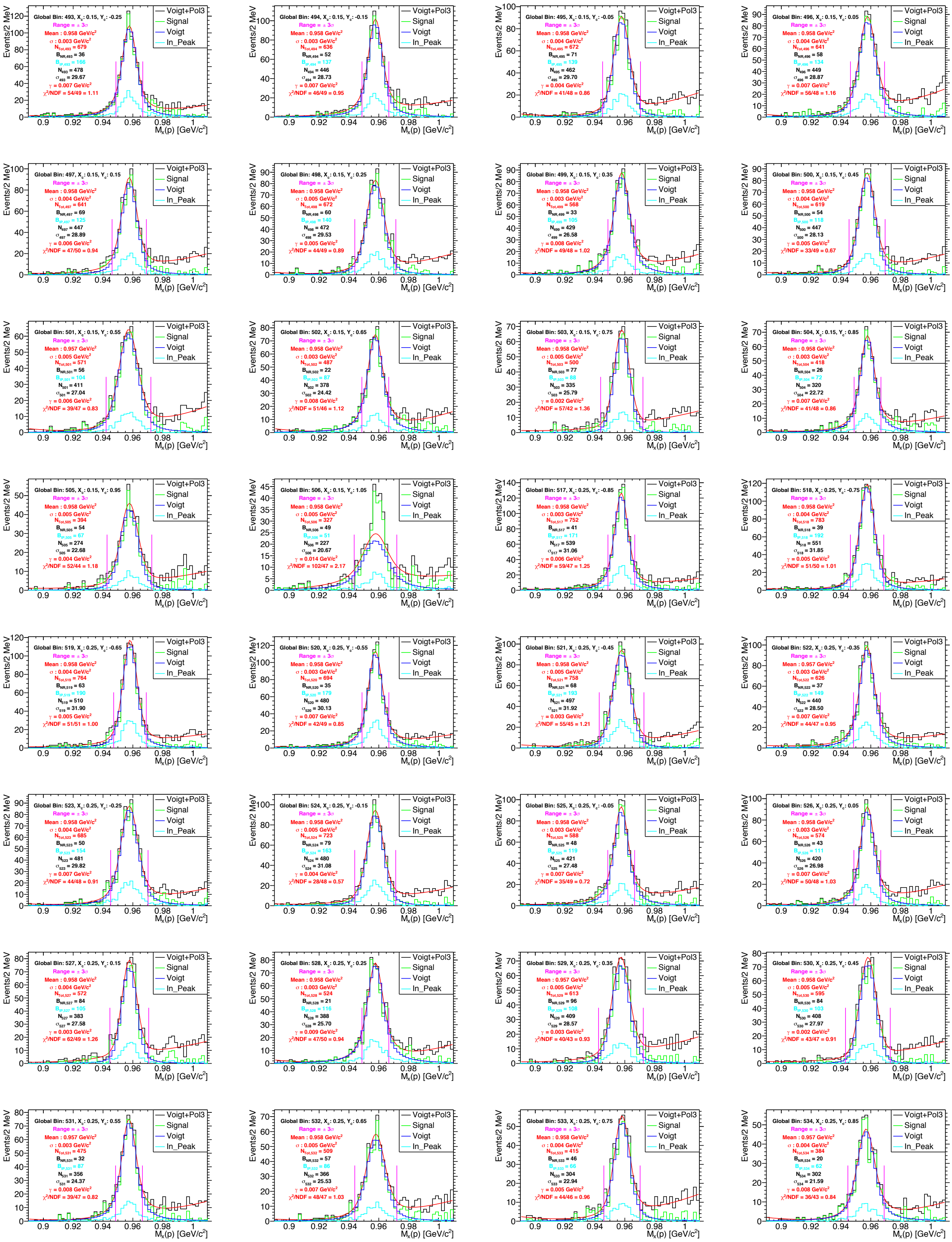
Voigt+Pol3
Signal
Voigt
In_Peak
Events/2 MeV
M_x(p) [GeV/c^2]

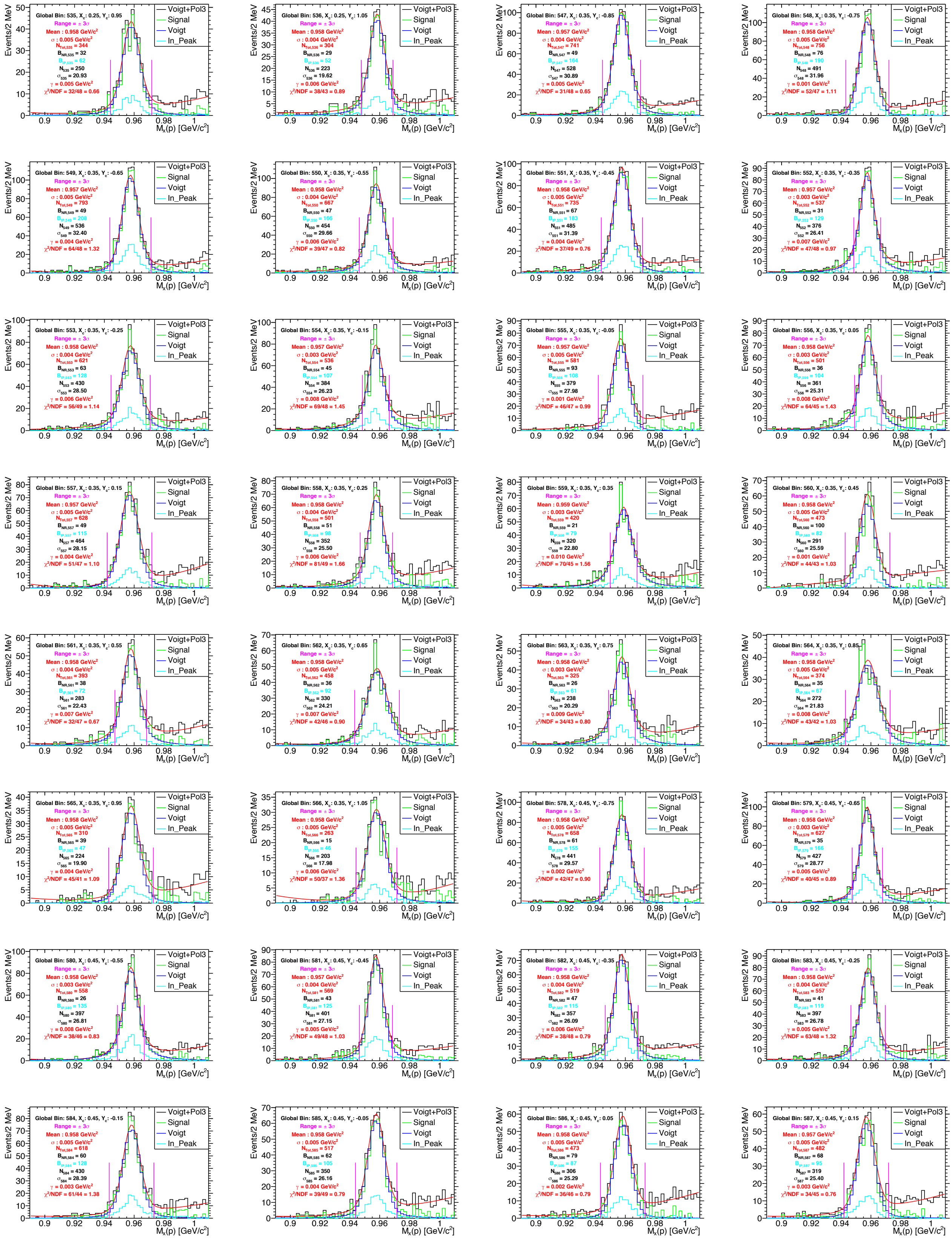

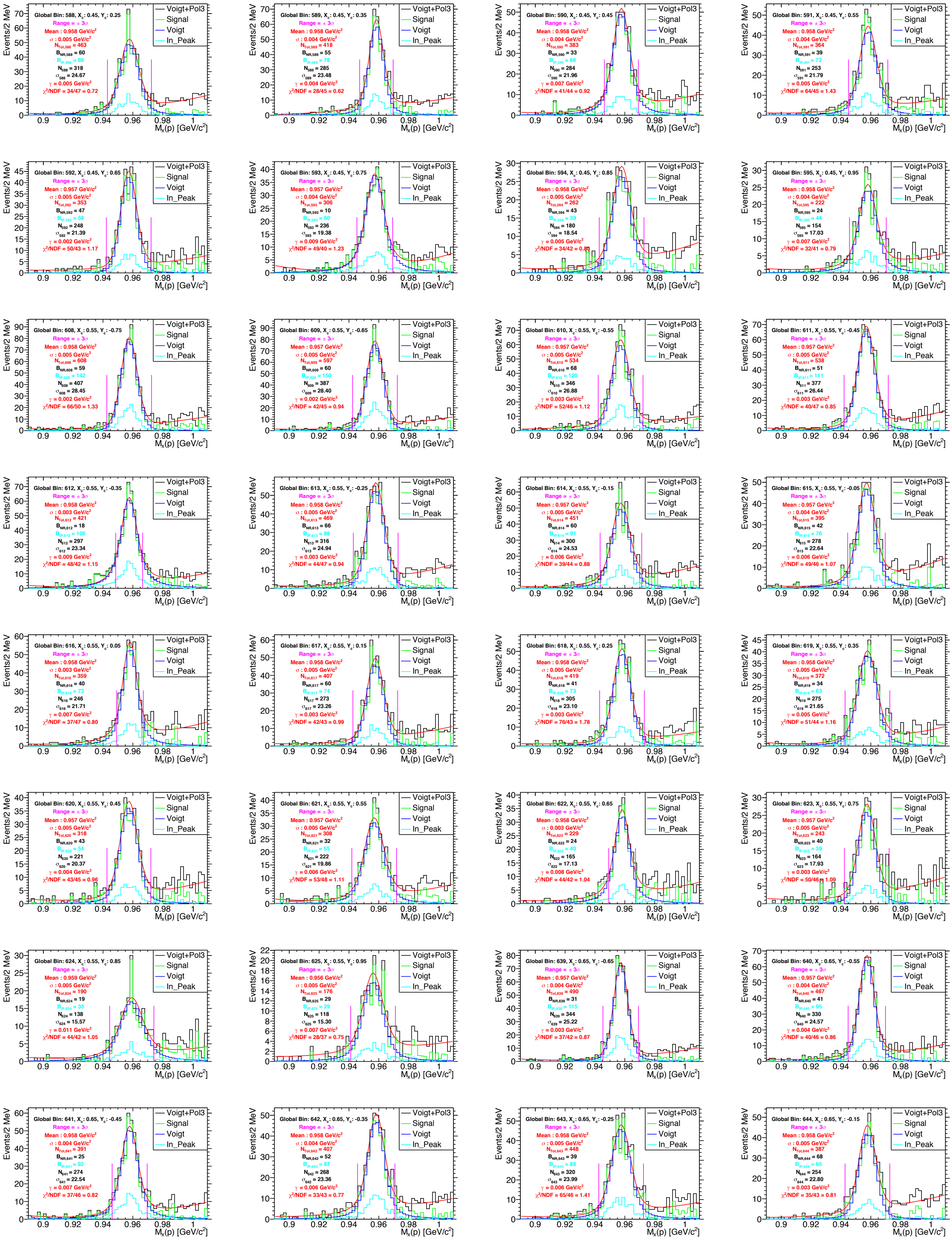
Events/2 MeV
M_x(p) [GeV/c^2]
Voigt+Pol3
Signal
Voigt
In_Peak

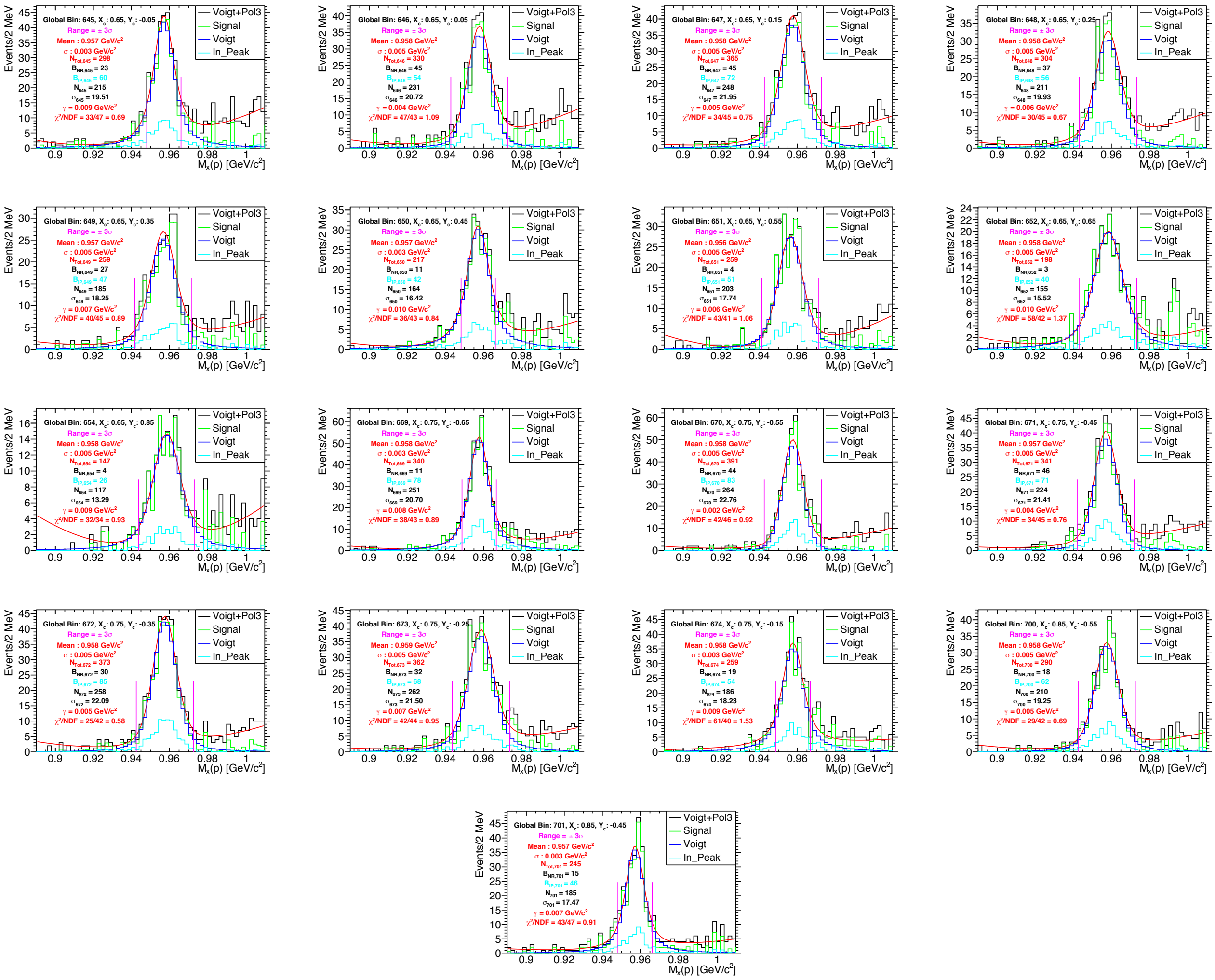

Voigt+Pol3
Signal
Voigt
In_Peak
Events/2 MeV
M_x(p) [GeV/c²]